Novel Visible Light Positioning Techniques

A THESIS PRESENTED IN PARTIAL FULFILMENT OF THE REQUIREMENTS OF THE DEGREE OF

DOCTOR OF PHILOSOPHY

IN

DEPARTMET OF MECHANICAL AND ELECTRICAL ENGINEERING

AT MASSEY UNIVERSITY, ALBANY, NEW ZEALAND

Moi Tin Chew

January 2024

Abstract

Localization is the process of finding an object's position within the space that it is situated in. Localization can be categorised into two types, indoors and outdoors. Outdoor localization is already a matured technology which mainly relies on well-known positioning satellite systems such as Global Positioning System (GPS) and GLObal NAvigation Satellite System (GLONASS). However, the indoor localization is still a growing area of research. Visible Light Positioning (VLP) has been getting the attention of researchers due to several advantageous factors. VLP is more accurate than many of the competing techniques. As Light Emitting Diode (LED) based luminaires have become an integral part of the indoor lighting systems in modern buildings and residences, such lighting infrastructure can be leveraged for localizing objects. The VLP systems are also suitable in places like hospitals and airports due to the fact that LED does not generate electromagnetic interference which can potentially affect the operation of many equipment used in those places. This doctoral research develops novel techniques and applications for VLP, and these are fully supported by experimental results and data analysis.

Fingerprinting is a common positioning method used in VLP systems that employs Received Signal Strength (RSS) as the signal characteristics. Weighted K-Nearest Neighbour (WKNN) is one of the most popular algorithms for such localization systems. This thesis investigates the impact of distance metrics used to compute the weights of the WKNN algorithm on the localization accuracy of the VLP. Experimental results show that Squared Chord distance is the most robust and accurate metric and significantly outperforms the commonly used Euclidean distance metric.

Robot navigation is one of the many potential applications of VLP. Recent literature shows a small number of works on robots being controlled by fusing location information acquired by VLP that uses rolling shutter effect camera as a receiver with other sensor data. In contrast, this thesis reports the experimental performance of a cartesian robot that was controlled solely by a VLP system using a cheap photodiode-based receiver. Two different methods (Direct Method and Spring Relaxation Method) were developed to leverage the VLP as an online navigation system to control the robot. The experiments consisted of the robot autonomously repeating various paths multiple times. The results show that both methods offer promising accuracy, with Direct Method and Spring Relaxation Method reaching the target positions of median / 90-percentile error of 27.16mm / 37.04mm, and 26.05mm / 47.48mm respectively.

The operation of VLP is very much dependent on the line of sight (LOS) link between the luminaires and the receiver. Unfortunately, in a practical environment, luminaires are positioned to serve illumination needs. Therefore, enough luminaires may not be visible for the purpose of positioning the target. One way to compensate this would be to utilise an ultrasound system to eliminate the “blind spots” of the VLP system. The final part of this work consists of a study of the ultrasound based indoor localization. A bespoke system employing an ultrasonic array to transmit chirp signals and time of flight measurement for ranging was developed. The position of the receiver is estimated iteratively using the spring relaxation technique. The spring relaxation technique, which has not been used for ultrasonic localization in the literature, outperforms the widely adopted linear least square-based lateration technique. The experimental results show that the ultrasonic system can be a viable option for fusing with a VLP system.

Acknowledgements

First, I would like to express special thanks to the main supervisor of my PhD journey, Professor Fakhrul Alam, for his astuteness in guiding me throughout the years of research and experimental studies as well as scholarly activities. Several times, I faced difficulties in breaking through some challenging concepts or presenting my findings clearly and concisely. With his supervision experience, research capability, and theoretical and practical expertise in a multitude of domains of signal and systems, communications, computing, and data processing, he skilfully guided me towards finding the right solutions leading to obtaining and presenting valuable results. I sincerely appreciate his excellent guidance, mentorship, friendship, and true care for my PhD studies.

Dr Mathew Legg, who was my co-supervisor, helped me learn using mathematical simulation efficiently in my study. I also benefitted immensely from his expertise in the acoustic field thus leading me to ultrasound indoor localization as a supplementary solution.

The third member of my supervision team was Professor Gourab Sen Gupta. He has been my long-time valuable colleague since the mid-90s at Singapore Polytechnic and then – Massey University. He was always available to provide his expert advice in robotics, navigation, and embedded system design. He also helped greatly whenever I needed help with my teaching responsibilities. His assistance allowed me to have more time to concentrate on progressing and finalising my PhD study while also working as an academic with considerable teaching duties.

Finally, I want to dedicate this achievement to my husband who has given me unceasing encouragement and immeasurable support throughout the entire time of my PhD study.

Due to various reasons in life, I started my PhD journey later than many other candidates - after three decades of extensive academic education work at several tertiary institutions in different countries. Yet, I did not feel disadvantaged in any way. In fact, I enjoyed working with my bright and energetic young colleagues - PhD candidates. Many of them were students of my classes during their undergraduate studies. And it helped us create a very important and productive postgraduate study bond and partnership. I received invaluable support from my ex-students Baden Parr, Tapiwa Wenge, Tyrel Glass, Nathaniel Faulkner, and Adli Hasan. They were very generous in sharing their time, expertise, and research findings with me. Another former student whom I appreciate deeply was Alex Xu, a young and bright research assistant who helped me with experiments and data collection.

The list would not be complete without the acknowledgement of the invaluable financial and administrative support provided to me by the School of Engineering and Advanced Technology and the School of Food and Advanced Technology of Massey University, New Zealand. My most sincere thanks go to the schools and great colleagues there.

List of Abbreviations

VLP	Visible Light Positioning
AOA	Angle of Arrival
CDF	Cumulative Distribution Function
CMOS	Complementary Metal-Oxide-Semiconductor
CNC	Computer Numerical Control
COTS	Commercial Off-the -Shelf
DT	Data Translator
ED	Euclidean Distance
FDM	Frequency Division Multiplex
FFT	Fast Fourier Transform
GLONASS	Global Navigation Satellite System
GPS	Global Positioning System
IoT	Internet of Things
LED	Light Emitting Diode
LiDAR	Light Detection and Ranging
LLS	Linear Least Square
LOS	Line of Sight
MOSFET	Metal-Oxide-Semiconductor Field-Effect Transistor
PD	Photo Diode
RF	Radio Frequency
RFID	Radio Frequency Identification
RSE	Rolling Shutter Effect
RSS	Received Signal Strength
RX	Receiver
SCD	Squared Cord Distance
SCSD	Squared Chi-Squared Distance
SNR	Signal to Noise Ratio
SR	Spring Relaxation
TDM	Time Division Multiplex
TDMA	Time Division Multiplex Access

TDOA	Time Difference of Arrival
TOA	Time of Arrival
TOF	Time of Flight
TX	Transmitter
UIL	Ultrasound Indoor Localization
US	Ultrasound
UWB	Ultra-Wide Band
VLC	Visible Light Communication
Wi-Fi	Wireless Fidelity
WKNN	Weighted K-Nearest Neighbor
WLLS	Weighted Linear Least Square

List of Figures

List of Tables

Table of Contents

Chapter 1 - Introduction

Knowing where you are and your position in relation to the surroundings is called context-aware localization. One of the best-known context-aware localization methods used in the outdoor setting is the Global Positioning System (GPS). This satellite-based positioning has been popularly used for numerous applications. However, GPS cannot be reliably applied in an indoor environment due to the signal attenuation caused by the structural material in the building. Consequently, other technologies have been researched for indoor localization systems. Indoor localization research is a growing field, as it has not reached the same level of scalability and adoption rate as that of GPS. The proliferation of modern smart phones, efficient and energy saving wireless sensor nodes, wearable devices, and Internet of Things (IoT) technologies have all contributed to the rising popularity of this research area. Wireless technologies like Wi-Fi [1], Radio Frequency Identification (RFID) [2], Ultra-Wide Band (UWB) [3] and ZigBee [4] have been proposed and investigated for indoor localization systems. However, with these systems, the localization error can be large (sometimes in the order of meters) due to the effects of multipath. Wireless localization is also vulnerable to interference. Ultrasonic localization [5] can be very accurate. However, they require the deployment of significant additional infrastructure. Researchers have used magnetic fingerprinting techniques [6] for indoor localization. Although these techniques do not require additional infrastructure, their accuracy (often in the order of meters) is not good enough for most applications, and they are susceptible to ferromagnetic perturbations. Magnetic fingerprinting is useful as a complement for other localization techniques especially when the primary system is experiencing poor conditions [7]. Light Detection and Ranging (LiDAR) [8] and computer vision-based [9] techniques solutions offer much lower error, in the order of millimeters. But they are costly and require significant computational power. In recent years, Visible Light Positioning (VLP) [10] have attracted a lot of attention within the research communities. This is because Visible Light Communication (VLC) [11] technologies have the potential to replace wireless communication technologies in the near future. The potential advantages include lower costs due to the ability to leverage existing infrastructure, durability, and environmental friendliness. However, most importantly from the localization perspective, visible light-based systems have the ability to estimate an object’s location to a high degree of accuracy [12], which is in the order of less than 3cm for mean error.

1.1 Visible Light Positioning

In VLP systems, LED luminaires are used as the transmitting beacons with either Photo Diode (PD) or camera as the common receiver sensor attached to the tracked object. Both the sensors come with inherent advantages and disadvantages. While cameras may allow more sophisticated communication schemes [13], PD based receivers are considerably cheaper and energy efficient [14] and incur less computational cost [15].

Signal characteristics that are most commonly discussed in literature for localization are Received Signal Strength (RSS) [16], Angle of Arrival (AOA) [17], Time of Arrival (TOA) and Time Difference of Arrival (TDOA) [18]. RSS is the most common approach because it can be done using a single photosensor and does not require synchronized hardware which keeps the cost and complexity of implementation low [19]. AOA implementations generally require more than a single photosensor or specialized optics [20]. TOA and TDOA based systems require highly synchronized hardware which increases the cost of implementation [18].

Visible light positioning algorithms can be broken down into three major categories: proximity, fingerprinting and model based techniques [21]. In some cases, the former two techniques can be considered to be simple and use less complex algorithms to estimate an object's position as compared to the latter. Model based positioning often utilizes the concept of signal ranging. The target that has the photosensor attached to it senses the signals from multiple light sources or luminaires and the distance from each luminaire (range) are estimated using a characteristic of the received signal and a model of the falloff of the light. The position of the object relative to the luminaires can then be determined using a lateration algorithm. Examples of model based localization systems using lateration can be found in [12, 22].

For a fingerprint-based system, a position within the target floor space is characterized as an ID which is made up of a vector of the detected RSS (or other signal characteristic) from each of the luminaires. An offline database is thus constructed by taking a set of RSS measurements that uniquely identify select locations within the space that the object is localized in. Once the construction of this database is complete, localization of the object is performed by capturing the current signal and then running a classifying algorithm or a regressor to determine an estimate of the position based on the offline database [23].

1.2 Research Objectives/Questions

The literature review on VLP identified some clear gaps that need to be addressed. Based on this, the PhD work had three clear objectives to improve state of the art of VLP.

- Majority of the VLP systems found in the literature[1] showing high accuracy is theoretical in nature and typically report simulation-based results. The practical implementations found in the literature are a) often limited to small-scale testbed; b) use specialised expensive luminaires and components; and/or c) operate within a controlled environment. Therefore, the focus was on room-scaled implementation of VLP using commercial off-the-shelf (COTS) luminaires and electronic components. Weighted KNN (WKNN) is among the most popular algorithms for fingerprint based VLP systems. Therefore, a major objective of this PhD work is to improve the accuracy of the WKNN algorithm.
- Robot navigation is one of the many potential applications of VLP. However, there is a noticeable lack of works that utilize VLP for controlling a robot. Recent literature shows only a small number of works on robots being controlled by fusing location information acquired by VLP that uses Rolling Shutter Effect (RSE) camera as a receiver with other sensor data. There is no reported work that has used only a photodiode based VLP to control a robot. Therefore, another objective of this PhD work is to develop and implement novel algorithms to control the movement of a robot, solely by a photodiode VLP system in real time.
- Visible Light Positioning is envisioned to leverage pre-existing lighting infrastructure. The number of the luminaires and their respective positions are therefore dictated by the requirements of illumination. It is possible that sufficient number of luminaires may not be visible at certain locations creating coverage “blind spots” for the VLP system. Other signal sources can potentially be utilised to supplement the light sources and thus provide enough information to localise a target. Given the high accuracy of the VLP system, the supplementary source should also provide very accurate ranging/localization. Due to such stringent demand, popular RF or wireless based positioning techniques are not viable. Literature review shows that ultrasound-based

---

[1] Circa 2018 (at the start of the PhD)

positioning can be very accurate. The final objective of this thesis is to evaluate the efficacy of ultrasound-based positioning. In particular, the goal is to

- develop and implement an ultrasonic positioning system that is very accurate allowing it to potentially address the lack of sufficient number of visible luminaires.
- adopt a localization algorithm for the ultrasonic system that has been used for VLP; thus, making a seamless integration viable.
- benchmark the ultrasonic system's accuracy against a VLP system with both systems being deployed in the same environment.

1.3 Contribution

By meeting the objectives outlined in the previous section, the PhD work makes the following original contribution to improve the state of the art of VLP:

- The impact of distance metric on the performance of the WKNN algorithm for a VLP is demonstrated. It is shown that the Squared Chord Distance (SCD) is the most robust distance metric and provides better localization accuracy than the commonly used Euclidean distance (ED). This is the first work, as far as we are aware of, that investigates the impact of distance metric on the performance of the WKNN classifier within the context of indoor localization.
- Two novel algorithms are proposed and implemented to control the movement of a cartesian robot, constructed in the form of a 2D Computer Numerical Control (CNC) machine, solely by a VLP system in real time. This also allowed to objectively evaluate the efficacy of a PD-based VLP system for controlling a robot. Based on the experimental results collected while the robot is traversing multiple path patterns, both algorithms show promising accuracy. As far as we are aware of, this the first work that utilizes only a PD- based VLP system to control the movement of a robot.
- This thesis presents the first study to benchmark the accuracy of an ultrasonic positioning system against a VLP system using the same platform setup. We apply the spring-relaxation algorithm for ultrasound indoor localization in a realistic sub-room scale environment. The weights, analogous to the Young's modulus, of the springs are adjusted to mitigate the ranging error resulting from multipath interference. To the best

of our knowledge, this novel concept of utilizing springs of varying stiffness to mitigate multipath interference has not been reported in the literature.

1.4 Thesis Outline

This thesis details the accounts of work, experiment results as well as findings in the following chapters:

Chapter 2: This chapter presents the fundamentals of visible light positioning. It describes the three categories of indoor localization techniques using visible light, these are proximity, fingerprint and model-based techniques. It also describes how ranging is obtained using model-based technique. From there it leads to object localization using the 2D lateration algorithm, based on Linear Least Square (LLS) and Weighted Linear Least Square (WLLS) Positioning methods.

Chapter 3: The chapter describes the experimental set up to attain accurate location estimates for VLP system using the Weighted K-Nearest Neighbour (WKNN) classifier. WKNN is a machine learning algorithm that relies on the collection of the offline location fingerprinting database to infer the online position of a target object or device. The impact of distance metrics used to compute the weights of the Weighted K Nearest Neighbor (WKNN) algorithm on the localization accuracy of the VLP is investigated.

Chapter 4: This chapter reports on the successful experimental performance of using Visible Light Positioning (VLP) as a global guiding system for indoor robot localization and navigation. Two separate algorithms are proposed to leverage the VLP as an online navigation system to control the robot.

Chapter 5 This chapter reports the development and experimental results on Ultrasound Indoor Localization (UIL) system based on Spring Relaxation (SR) technique. Latter part of the chapter looks at benchmarking the UIL with VLP using the same platform.

Chapter 6 This provides the summary of the PhD work that addresses several gaps in the literature of visible light positioning as well as some pointers for the future work.

1.5 Publication

The investigations conducted in this thesis has directly resulted in the publication of the following journal articles:

1. **M.T. Chew**, F. Alam, F. Noble, M. Legg, and G. S. Gupta, "Visible Light Positioning Based Robot Localization and Navigation", Electronics, January 2024 (**Q2, IF 2.9**)

   https://doi.org/10.3390/electronics13020368

2. **M.T. Chew**, F. Alam, M. Legg, and G. S. Gupta, "Accurate Ultrasound Indoor Localization Using Spring-Relaxation Technique", Electronics, May 2021 (**Q2, IF 2.9**)

   https://doi.org/10.3390/electronics10111290

3. F. Alam, **M.T. Chew**, T. Wenge, and G. Sen Gupta, "An Accurate Visible Light Positioning System Using Regenerated Fingerprint Database Based On Calibrated Propagation Model," IEEE Transactions on Instrumentation & Measurement, 2018. (**Q1, IF 5.6**)

   DOI: 10.1109/TIM.2018.2870263

Chapter 2 – Visible Light Positioning Fundamentals

It is predicted that the next generation of wireless communication technology will be based on Visible Light Communication (VLC). VLC technology might not be able to replace the radio frequency (RF), but in some areas it certainly can outperform the Wi-Fi, Bluetooth and UWB technology, especially with regards to indoor localization application. This has given rise to the concept of VLP or Visible Light Positioning.

The data transmission is done by encoding the information through modulating the frequency, amplitude, or both of the optical light signal. At the receiver end, there is a photo detector that can demodulate the information back to its original signal format. The benefit of VLC is that commercial of-the-shelf (COTS) light emitting diode (LED) and common photodiode sensor can be used as the transmitter and the receiver respectively. When transmission of data is carried out by more than one LED, the most common method of data protocol will be based on time division multiplex (TDM) or frequency division multiplex (FDM) [24]. Figure 2.1 shows the data transmission from two light sources sending individual data information to the receiver unit

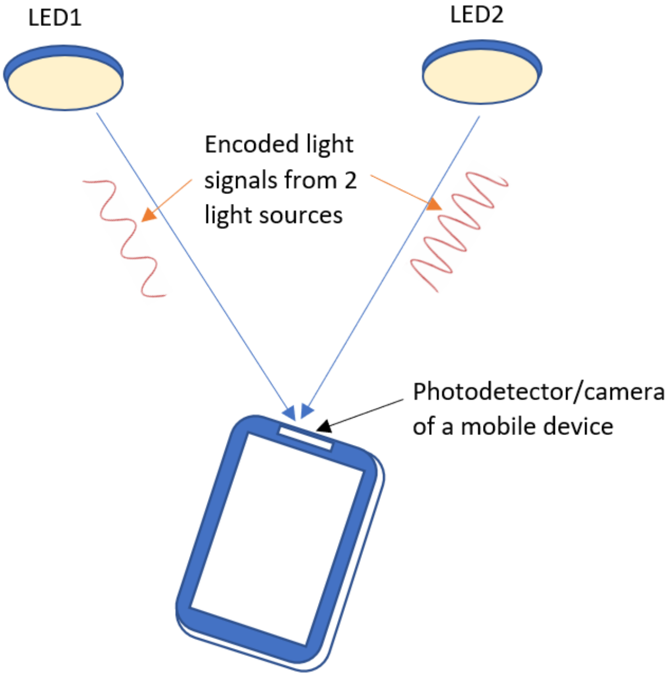

Fig.2.1 Visible light communication from 2 LEDs to a photodetector of a mobile device

Figure 2.2 shows a block diagram of a typical VLC system where signal transmission and reception take place, yet at the same time ensuring its primary aim to illuminate the room is not compromised [25].

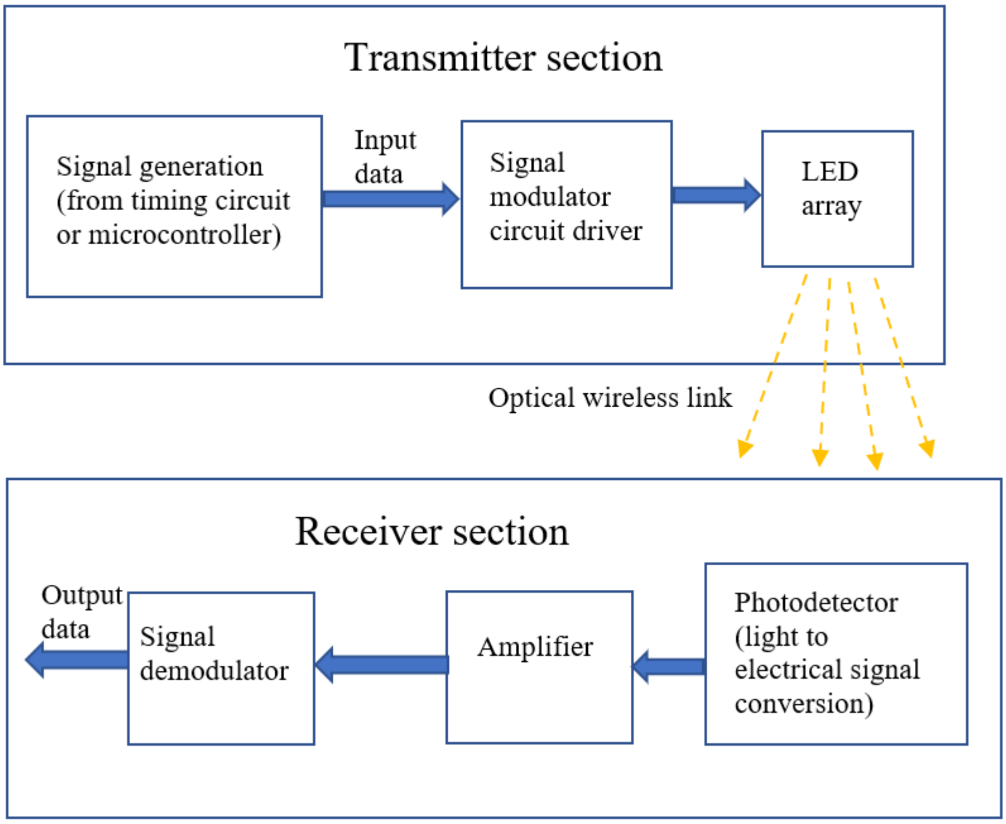

Fig. 2.2 Block diagram of a VLC system, showing data communication through optical wireless link (at the same time providing illumination to the room)

2.1 VLP techniques

In general, the indoor localization techniques using visible light can be categorised into three types. These are proximity, fingerprint and model based techniques [21] .

2.1.1 Proximity

The proximity method is the simplest positioning technique out of the three. In this technique, the position of a mobile device is determined by the signal transmitted by a single LED light station. Normally each LED light station has its own identity (ID), and this ID is identified with a particular location or region. Once the mobile device detects the light signal through its photo sensor receiver, it will send the data information to the processing node which is either the on-board processor or central computer via ZigBee or Wi-Fi. The processing node will check this ID and its corresponding position using a pre-stored database or a lookup table which contains the information of all the LEDs and their paired-up locations. Due to the inherent granularity, the distance error for this technique can be in the range of a few meters. Whether the mobile device is placed just below the LED or a few meters from the LED, the position is the same for both cases as long as the mobile device is within the exposure of the same light source. Since proximity-based localization only provides general location of the object, it is not so desirable for localization of robots and applications where a more precise positioning data are required (e.g., for robot navigation).

2.1.2 Fingerprint

Fingerprint based techniques, often referred as scene analysis technique, consists of offline and online phases. During the offline phase, information of light parameter is collected at various selected positions to construct a mapping data about the environment. Once the fingerprinting map, termed as the offline fingerprint database, is completed, the online phase which is the object localization phase will begin. This is done by capturing the current signals from the light sources, at the photoreceiver of the target unit, and matching it with the data sets in the database to get its current position estimate. A few known algorithms can be deployed to find the best match, examples of the classification algorithms are random forest [26] , k-nearest neighbours, artificial neural networks, support vector machine [27] and Naive Bayes classifier [28].

2.1.3 Model-based technique

This is based on the concept of signal angulation or lateration. Angulation method relies on measuring the Angle of Arrival (AOA) of received signals with respect to the reference light sources [29], in order to formulate the target’s location. Whereas the lateration method, performs ranging (range is the distance of the receiver from each of the transmitter LEDs of known coordinates). The unknown receiver’s location is then be determined by using mathematical spherical equations relating to these distances. For this to work, it requires range information from minimum of 3 transmitters [30]. Signal characteristics that can be used for ranging includes RSS, Time of Arrival (TOA) and Time Difference of Arrival (TDOA).

2.2 Received Signal Strength (RSS)

RSS is the most common signal characteristic used for visible light positioning. It is the received signal intensity which is a function of the distance between the luminaire and the photodetector. As the photoreceiver is moved further away from the light source, the received signal strength will be less intense. One advantage of RSS measurement is that it can be done using a single photodetector and does not require synchronized hardware which keeps the cost and complexity of implementation low [31]. Measuring AOA requires special optic with array of sensors in order to measure the incident angle with high accuracy [32], thus putting more cost on the hardware implementation. TOA and TDOA measurements require strict synchronization [27] between the hardware modules, essentially leading to high implementation cost.

2.2.1 Optical Channel Modelling

In using visible light for the purpose of localization, the LED transmitter with a large beam divergence is often regarded as a Lambertian source that emits light uniformly in all direction.

Thus the transmitter radiant intensity follows the Lambertian radiant intensity [33] which is :

$$R_0\,(\phi) = \frac{(m+1)}{2\pi}\, cos^m\phi \qquad (2.1)$$

where ϕ is the angle of irradiance, the direction angle relative to the transmitter normal axis (Figure 2.3), and m is called mode number of radiation lobe which is related to $\Phi_{1/2}$ the semi-angle or half power beam width [34] of the transmitter – refer to Figure 2.4

$$\mathrm{m} = \frac{-\ln 2}{\ln\,(\cos\ \Phi_{1/2})} \qquad (2.2)$$

Half power beam width, $\Phi_{1/2}$ value is normally supplied by the LED manufacturers. A mode number of m =1 ($\Phi_{1/2}$ = 60°) corresponds to an ideal Lambertian source.

At the receiving end, the amount of optical power that a photodiode receives depend on its effective physical area, $A_{R_{eff}}$. Manufacturers usually employ optical concentrator lens to increase the effective area [33]

$$A_{R_{eff}} = A\cos(\psi)T_S(\psi)g(\psi) \qquad (2.3)$$

where T_S is the filter gain and g is the concentrator gain, A is the area of the photodiode and ψ is the incidence angle (see Figure 2.3).

In a standard photodiode, there is no concentrator, hence these gains can be considered as $T_S(\psi) = g(\psi) = 1$ [13], the effective area can therefore be expressed as:

$$A_{R_{eff}} = A\cos(\psi) \tag{2.4}$$

In the optical link, the DC channel gain can be modelled as:

$$H_0\,(\phi) = \frac{P_t}{d^2}\,R_0\,(\phi) \tag{2.5}$$

where d is the distance (Figure 2.3) between the transmitter and the photoreceiver, and P_t is the transmitter power.

As mentioned earlier, received power depends on the effective area of photoreceiver therefore:

$$P_r = H_0\,(\phi)\; x\; A_{R_{eff}} \tag{2.6}$$

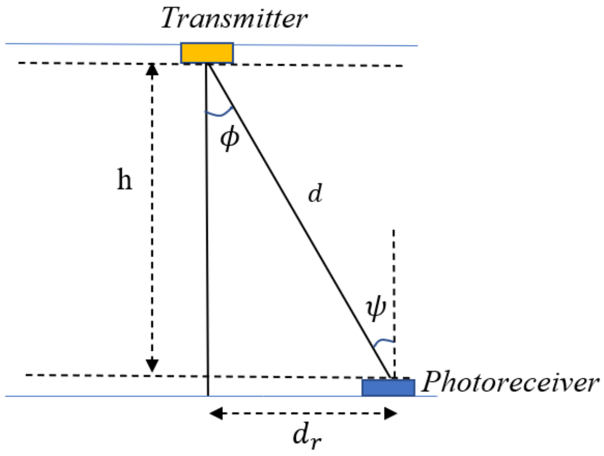

Fig.2.3 Lambertian propagation model

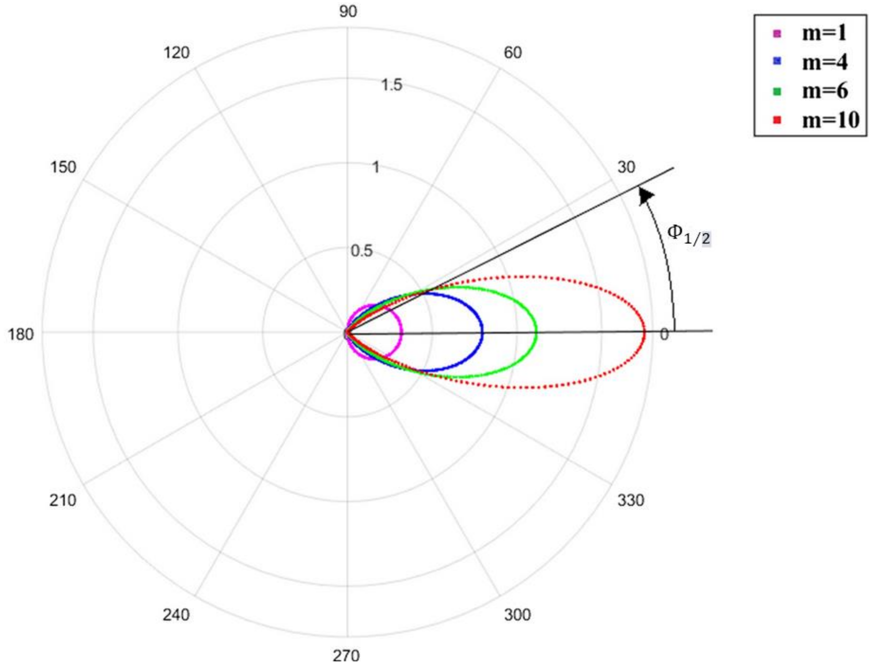

Fig. 2.4 Polar plot of radiation patterns from Lambertian LED sources, m = (1, 4, 6, 10) corresponding to $\Phi_{1/2}$ = 60°, 33°, 27°, and 22° respectively [34]

Using equations (2.1) (2.4) and (2.5), P_r becomes:

$$P_r = \frac{P_t}{d^2}\frac{(m+1)}{2\pi}\, cos^m(\phi)\; Acos(\psi) \tag{2.7}$$

Note that with $\Phi_{1/2} = 60°$ (an ideal Lambertian source), $m = 1$. Equation (2.7) can thus be further simplified to:

$$P_r = \frac{P_t}{d^2\pi}\, cos\,(\phi) A \cos\,(\psi) \tag{2.8}$$

In Chapter 4, a simplification technique based on equation (2.7) will be introduced. It is to account for the fact that real-world luminaires are not ideal and therefore the assumption that $m = 1$ is not accurate in a real-world environment.

2.2.2 Model-based Localization

In many localization applications, the device being tracked (e.g., a mobile robot) has a photoreceiver fixed at the top and within the field of view of the light source. It lends to the assumption that the ceiling where the transmitters are placed, is parallel to the floor [35]. This means that wherever the target moves within the tracking space, it will experience the same height, h from each transmitter. This helps to simplify the relationship between the receiver and transmitter power because the incidence angle ψ and the irradiance angle ϕ can be considered equal- see Figure 2.3, this gives:

$$\cos(\phi) = \cos(\psi) = \frac{h}{d} \tag{2.9}$$

Substitute this into equation (2.8) to get:

$$P_r = \frac{P_t A h^2}{d^4 \pi} \tag{2.10}$$

Finally, d the distance of the receiver from the transmitter (Figure 2.3) can be derived as:

$$d = \sqrt[4]{\frac{P_t C h^2}{P_r}} \tag{2.11}$$

where $C = \frac{A}{\pi}$ is a constant value

In a typical visible light positioning (VLP) system as depicted in Figure 2.5, it shows that the photodiode is receiving light signals from 4 LED transmitters, and associated distances from the LEDs are defined as d_{TX1} , $d_{TX2}, d_{TX3}, d_{TX4}$ respectively. From here a projected horizontal distance d_{ri} can be obtained using Pythagoras theorem:

$$d_{ri} = \sqrt{d_{TXi}^2 - h^2} \tag{2.12}$$

Once the horizontal range distance has been obtained from each LED transmitter, the location of the photodiode equipped object can be calculated using a linear least square algorithm for 2D lateration. This method requires horizontal distances from a minimum of 3 transmitters to locate the object's position. Essentially the method uses the projected distance as a radius to form circle from each LED. The point where the circles intersect will determine the object's coordinate- see Figure 2.6

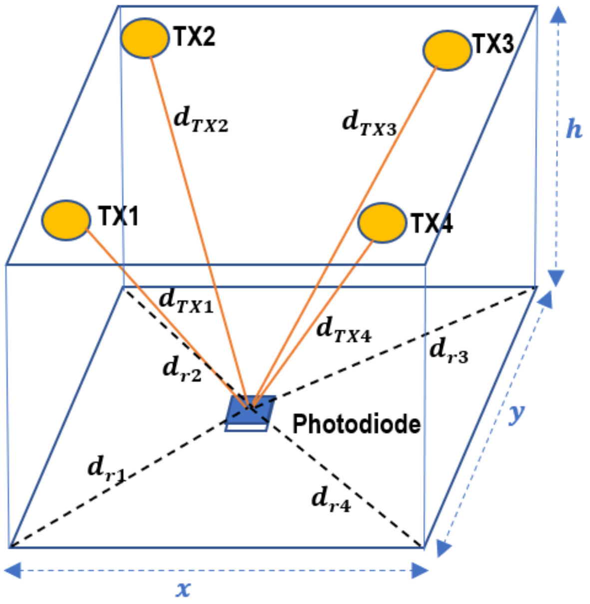

Fig.2.5 Typical VLP system with 4 LED transmitters

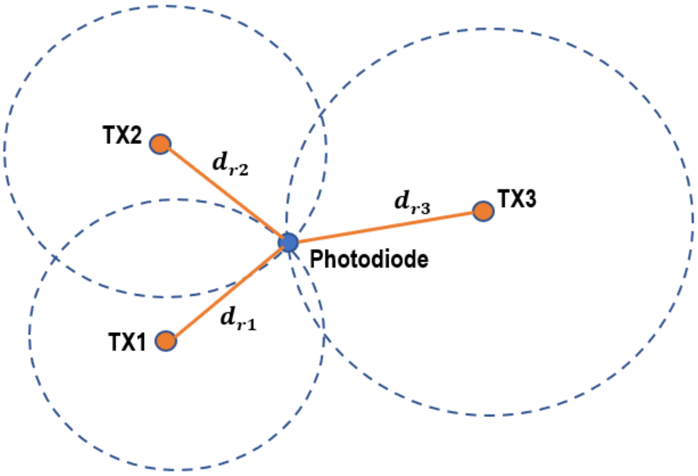

Fig.2.6 2D trilateration method using 3 LEDs and a photodiode equipped object

2.3 Localization Theory

Once the ranging distances from the luminaires are obtained, the next step is to incorporate this information into object localization theory to estimate the target's position. According to literatures, the most popular localization techniques are based on trilateration and multilateration techniques. The former uses signal information from 3 anchor sensors while the latter utilizes information from multiple anchor sensors. This report uses the term lateration which generally refers to either trilateration or multilateration.

2.3.1 Lateration

Localisation can be performed using lateration by finding the intersection point of circles or spheres, which have radii equal to the ranging distances r_i from the anchor node A_i - see Figure 2.7(a). The algorithm requires a minimum of three range distances from the reference anchor nodes to the unknown target unit, to form the three equations. The intersection point, which can be derived using the linear least square (LLS) method, is taken to be the position of the target unit. On the other hand, the position accuracy can be affected if the intersection is not in the exact cross point of the three circles, but rather in the overlapping area as depicted in Figure 2.7(b). This can be caused by range measurement errors.

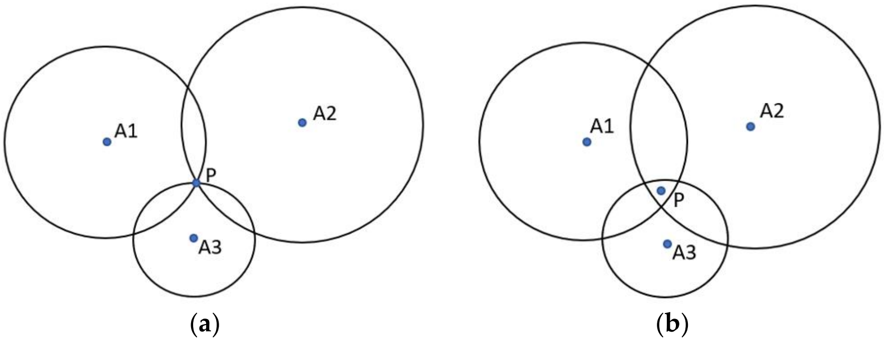

(**a**) (**b**)

Fig. 2.7 This diagram shows how trilateration can be used for localization. In diagram (a), the localization circles from three anchor nodes intersect at a single point P. In contrast, diagram (b) illustrates how distance errors result in the circles not intersecting at a single point meaning a least square fitting method is required for position estimation

2.3.2 Linear Least Square (LLS) and Weighted Linear Least Square (WLLS) Positioning

Figure 2.8 illustrates a 2D x-y plane looking from the top, where N is the total number of anchors used in the localization network. At any instance the target object requires the range distance information from each anchor nodes with indexes $j\{1,2 \dots W\}$, noted that $W \leq$ N.

The range measurement between the target and the *j*th (*j*=1, 2, 3, N where N=4 in this case) anchor is represented by r_j (see Figure 2.8) which has some element of random noise in it. The unknown target location is denoted with 2D coordinate $T = [x \;\; y]^T$ and the known 2D coordinate of the jth anchor is given as $T_j = [x_j \;\; y_j]^T$

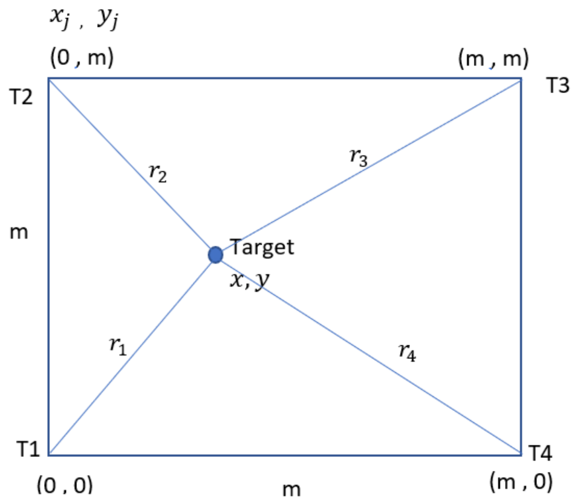

Fig. 2.8   2D x-y plane looking from the top

$r_j = r_1 , r_2 ,\; r_3 \;, r_N$ where j =1 , 2 , 3 , 4

$$r_j = T - T_j = \sqrt{(x - x_j)^2 + (y - y_j)^2} \tag{2.13}$$

$$r_j{}^2 = (x - x_j)^2 + (y - y_j)^2$$

$$r_j{}^2 = x^2 - 2xx_j + x_j{}^2 + y^2 - 2yy_j + y_j{}^2$$

$$-2xx_j - 2yy_j + x^2 + y^2 = r_j{}^2 - x_j{}^2 - y_j{}^2$$

$$-2xx_j - 2yy_j + S = r_j{}^2 - x_j{}^2 - y_j{}^2 \tag{2.14}$$

where $S = x^2 + y^2$

Therefore equation (2.14) can be re-written in matrix form as the following [36] :

$$H_I \, A = b_I \tag{2.15}$$

where $H_I = \begin{bmatrix} -2x_1 & -2y_1 & 1 \\ -2x_2 & -2y_2 & 1 \\ \vdots & \vdots & \vdots \\ -2x_N & -2y_N & 1 \end{bmatrix}$, $A = \begin{bmatrix} x \\ y \\ S \end{bmatrix}$ and $b_I = \begin{bmatrix} {r_1}^2 - {x_1}^2 - {y_1}^2 \\ {r_2}^2 - {x_2}^2 - {y_2}^2 \\ \vdots \\ {r_N}^2 - {x_N}^2 - {y_N}^2 \end{bmatrix}$

Multiply the linear equation (2.15) with ${H_I}^T$ (where T represents transpose operation), gives

$$({H_I}^T H_I)A = b_I {H_I}^T$$

$$A_{LLS} = b_I {H_I}^T ({H_I}^T H_I)^{-1} \tag{2.16}$$

As a result, the linear least square (LLS) position estimate which is the $(\hat{x}, \hat{y})$ coordinate of the target unit can be obtained from the first and second entries of matrix A, that is:

$$T_{LLS} = [\hat{x}, \hat{y}] = [\ [A_{LLS}]_1\ [A_{LLS}]_2\ ]^T \tag{2.17}$$

The location estimate, T_{LLS} obtained from equation (2.17) might not yield accurate result, this is due to the fact that distance range measurement is affected by random noise and signal fading whenever signal travels through the air medium. One way to improve the position accuracy is to use Weighted Linear Least Square (WLLS) positioning method. There are a few weighting methods one can use to apply in this technique, example Signal to Noise Ratio (SNR), Log (SNR), putting less weighting to the outlier range measurement, and so on. Using the weighing factor matrix *C*, the WLLS equation can be written as follows [36] :

$$A_{WLLS} = b_I {H_I}^T C ({H_I}^T H_I C)^{-1} \tag{2.18}$$

where C = diag ($[WT_1, WT_2, WT_3, \cdots, WT_N]$) , and N = total number of transmitters eg. WT_1 is a weighting factor relating to TX1 which is LED Transmitter1

The target unit’s location estimate can be written as

$$T_{WLLS} = [\hat{x}, \hat{y}] = [\ [A_{WLLS}]_1\ \ [A_{WLLS}]_2\ ]^T \tag{2.19}$$

Finally, the following shows the successful application of LLS lateration algorithm at 3 different locations: Figures 2.9 (a) (b) and (c) illustrate the 2D lateration results taken at 3 different test locations, each with reference to 4 known fixed anchor nodes (A1, A2, A3 and A4)

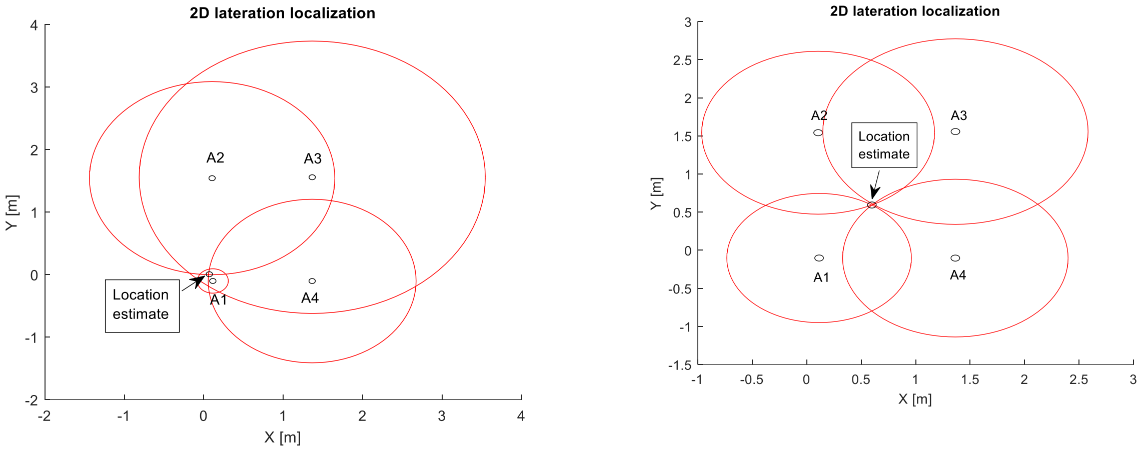

(a) Location 1 (b) Location 2

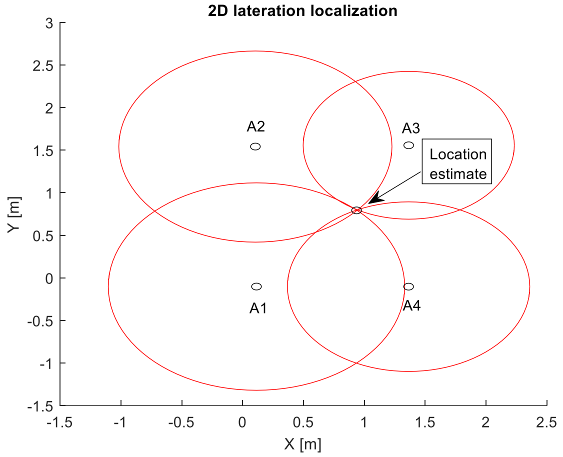

(c) Location 3

Fig. 2.9 2D lateration results at 3 different locations

2.3.3 2D Localization Accuracy

The accuracy of a localization system is most commonly evaluated through measuring the localization uncertainty which is termed as localization error in the literature [10] . Localization error is defined as the Euclidean distance between the actual position of the target (the ground truth) and the estimated position of the target. The Cumulative Distribution Function (CDF), mean, median and percentile values of the localization error are used to investigate the localization accuracy (please see the guidelines of [37, 38] for more details). In some cases, the standard deviation of the localization error is also reported. Consequently, these metrics will be used to evaluate the position accuracy of the various localization systems that are discussed in Chapter 3, 4 and 5.

Chapter 3 – Visible Light Positioning using WKNN: Impact of Distance Metric

This chapter reports the experimental results obtained with a room-scale VLP system using RSS based fingerprinting technique. The VLP system consists of cheap photodiode-based receiver and consumer grade LED luminaires. The impact of distance metrics used to compute the weights of the Weighted K Nearest Neighbor (WKNN) algorithm on the localization accuracy of the VLP is investigated. Experimental results show that Square Chord distance is the most robust and accurate metric and significantly outperforms the commonly used Euclidean distance metric. For this room scale implementation, a mean error of 2.2cm and a 90-percentile error of 4.9cm were achieved.

The performance of a fingerprinting-based localization system is heavily reliant on the algorithm used to classify the current signal based on the offline training. A broad range of pattern recognition and machine learning algorithms such as K-nearest neighbor (KNN), Neural Networks (NN) and Multiclass Support Vector Machines (SVMs) [39] are available to choose from. While classifiers like SVM [40] and NN [41] have been quite extensively used for wireless technology based indoor localization, comparatively simpler Weighed KNN (WKNN) [39] has been a popular choices for visible light based indoor localization. Comparative benchmarking shows WKNN to be more accurate and reliable compared to others for visible light based positioning [42]. Recent work also reports that WKNN performs favourably compared with model based methods in terms of accuracy [43]. Given these advantages of WKNN, it was selected as the classifier for the developed visible light positioning (VLP) system reported in this chapter.

It should be noted that majority of the VLP systems reported in the literature showing higher accuracy are theoretical in nature and typically show simulation based results [44]. Though there are reported cases of practical implementations, however these are mainly confined to a) small scale test bed [45] and/or b) use specialized expensive luminaires and components [45] and/or c) operate within a controlled environment [35]. In contrast, this chapter reports on a real-life room scaled VLP implementation that uses off-the-shelf consumer grade luminaires.

3.1 System Description

The developed VLP system aims to locate the position of a photosensor equipped robot/device within a floor space of 3.4m x 2.2m. Figure 3.1 shows the setup of the test bed. The floor map is divided into many sections with a minimum grid size of 10cm x10cm. Above this floor space, there are four off-the-shelf LED luminaires mounted on the ceiling, one at each corner. The ceiling height is 2.4m. Each of these 4 luminaires transmits its individual light identity to the photo sensing robot/device using square wave modulation signal and at the same time provides illumination to the room as illustrated in Figure 3.2. This modulation is implemented using the MOSFET driver circuit shown in Figure 3.3a and Figure 3.3b.

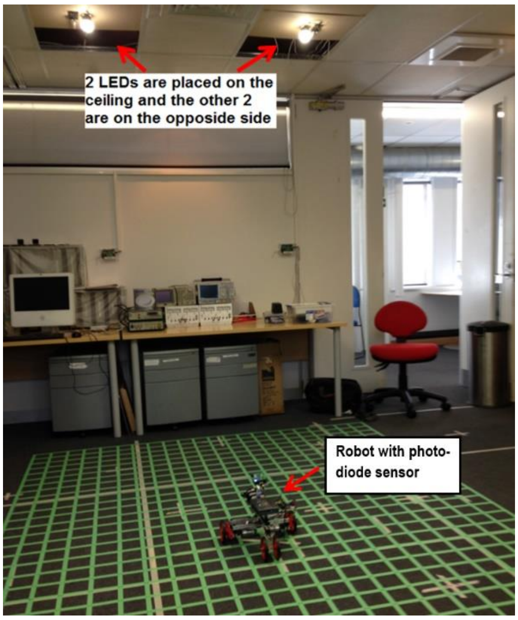

Fig. 3.1 Visible light localization testbed

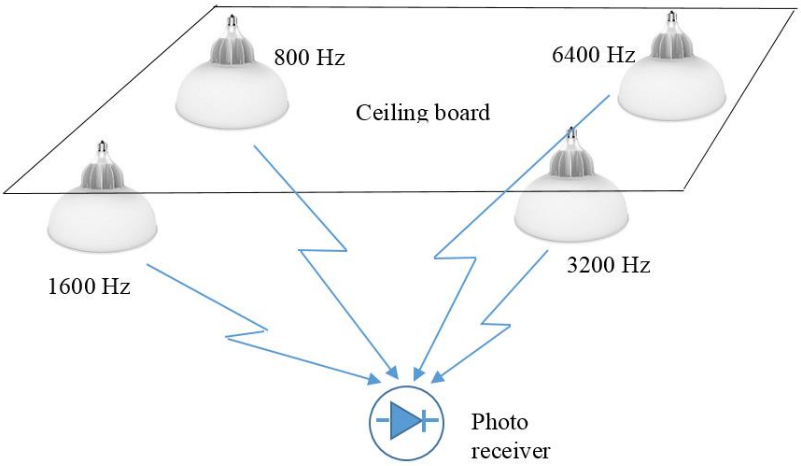

Fig. 3.2 System overview of visible light fingerprinting testbed

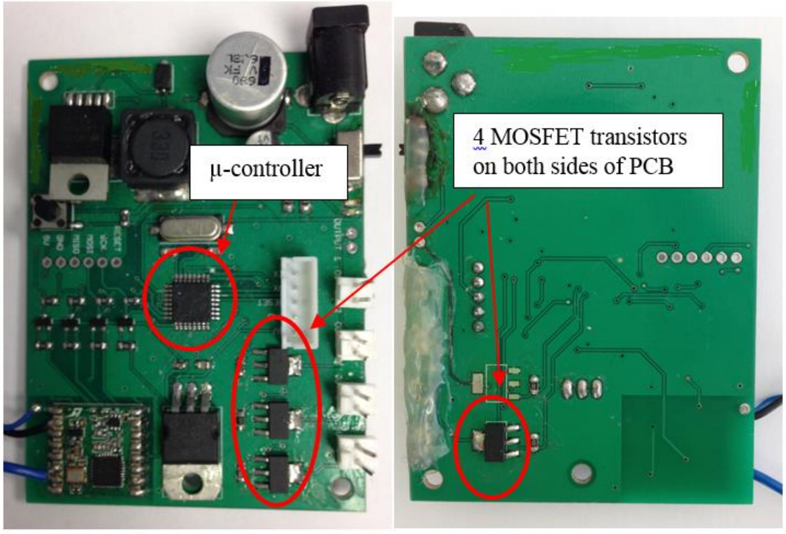

Fig. 3.3a VLC light modulation –MOSFET driver circuit and printed circuit board

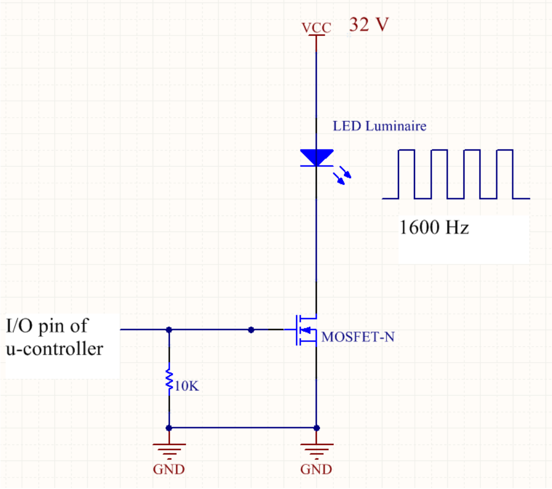

Fig. 3.3b Modulator driver circuit – shows one of the 4 LED luminaires sending out 1600Hz square wave generated from the microcontroller ATmega328P

The overall receiver system block can be described in Figure 3.4. First, the robot which is fitted with a photodiode receives the 4 transmitted light signals from the ceiling. The photodiode together with the amplifier then converts the optical signal to electrical signal, this in turns passes to onboard 16-bit ADC for conversion to digital signal. This digital signal obtained is sent to either onboard microcontroller or MATLAB for Fast Fourier transform (FFT) processing to get a frequency spectrum of these lights. Each robot’s position will display its unique frequency spectrum corresponding to the coordinate where it is placed on the floor map.

The next section explains how the blocks in Figure 3.4 interact with each other.

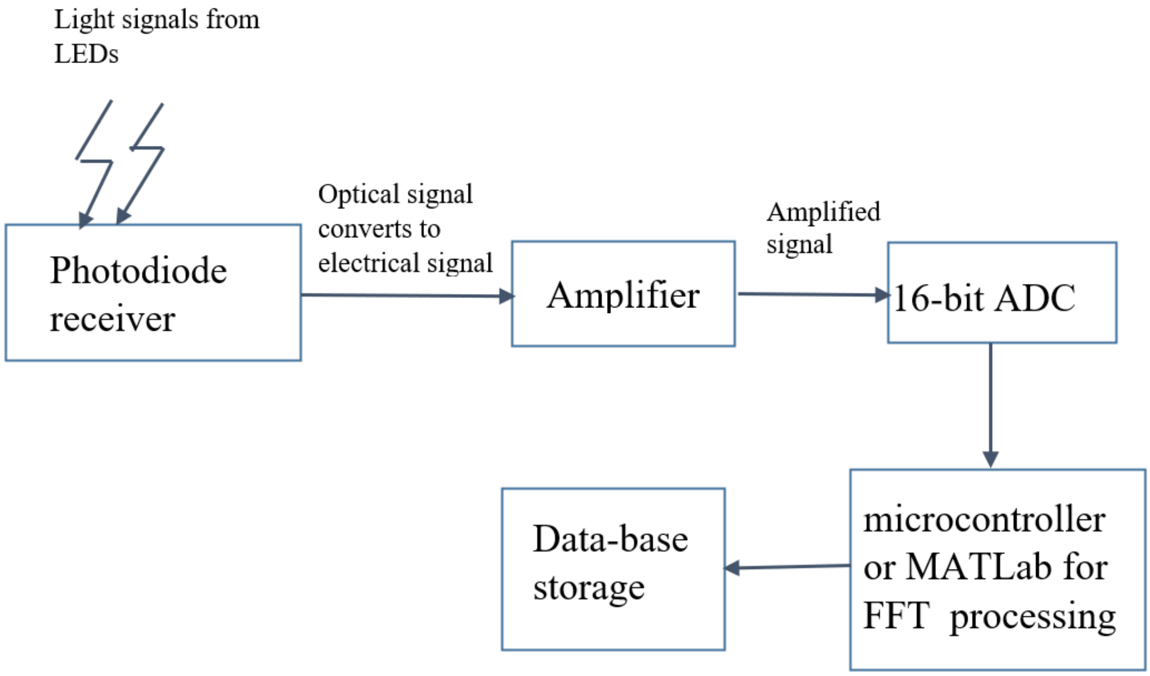

Fig.3.4 Receiver System Block

A. Photodiode receiver and amplifier

When operating a photodiode as a light sensor, it needs to be connected in a reverse biased mode in the circuit. When the light shines on the junction, the photoelectrons will result in an increase in the leakage current, I_{leak} and whole curve shifts downwards - see illustration in Figure 3.5a. The circuit in Figure 3.5b uses the photodiode which effectively acts as current source with an output current being proportional to the incoming light on the photodiode. The op-amp is connected as a current to voltage converter, which amplifies the signal before sending to the ADC converter.

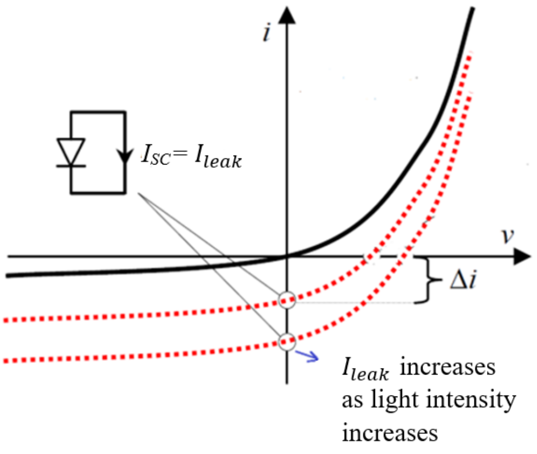

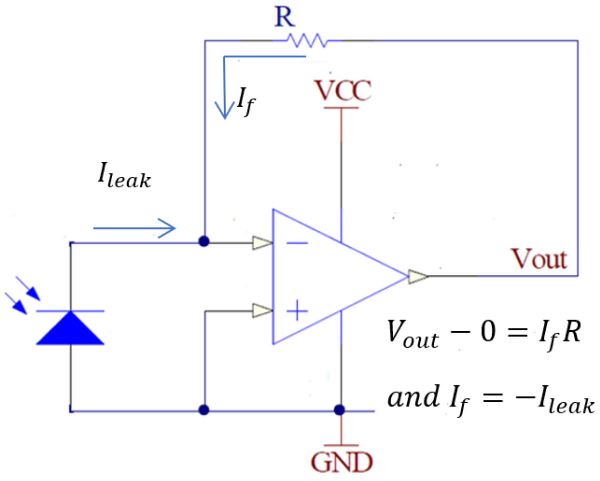

Fig. 3.5a iv-characteristic of photodiode

Fig 3.5b. current to voltage converter

B. ADC Converter and FFT processing.

The raw analogue signal will be processed into digital signal through 16-bit ADC converter, after which the signal is processed by standard FFT algorithm to obtain a frequency spectrum corresponding to the frequency ID of the 4 LEDs light sources. Figure 3.6a shows the FFT result obtained from the light received by the robot at one location and Figure 3.6b shows the fundamental frequency of each luminaire after filtering out the harmonics

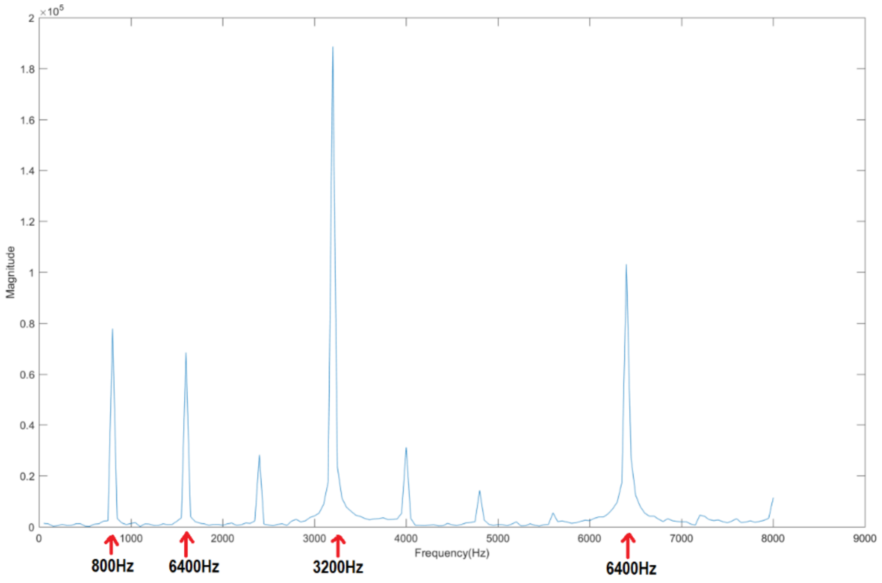

Fig. 3.6a FFT result showing the signal strength obtained from the 4 LEDs at one location – ie. frequency domain representation

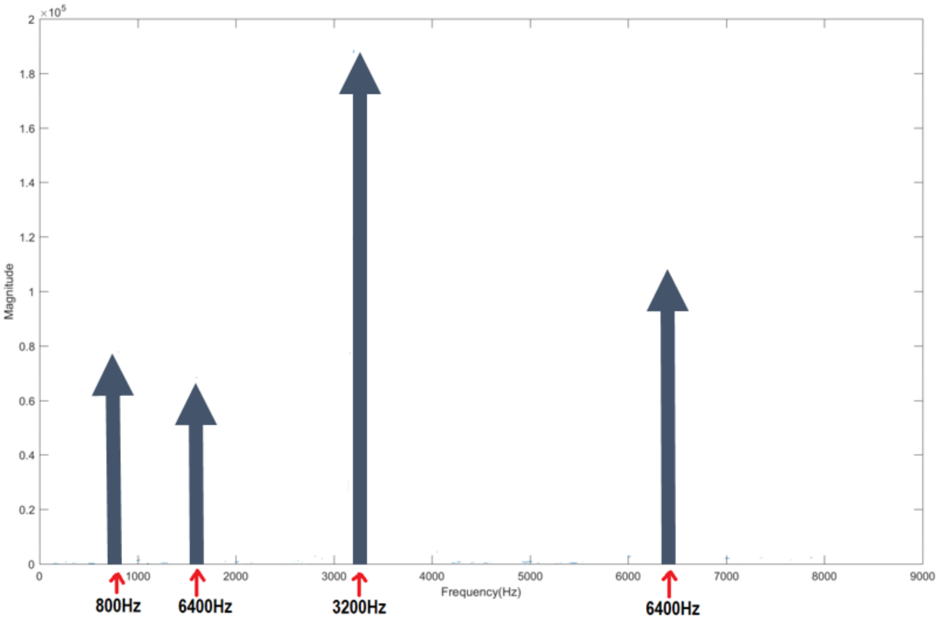

Figure 3.6b Fundamental frequency of each luminaire after filtering out the harmonics

3.2 Modulator Driver

The modulator driver carries two functions, one is to illuminate the room and the other is to communicate the ID code of each transmitter light source to the photosensor equipped object. The onboard microcontroller in the modulator circuit as in Figure 3.3, is responsible for generating the 4 ID signals in the form of square waves to drive the 4 LED luminaires. The signal generated at the I/O pin of microcontroller pulses between 3.4V to 0V and drives the gate input of the MOSFET N-channel transistor. The modulating frequencies chosen for the 4 luminaires in this system are 800 Hz, 1600 Hz, 3200 Hz and 6400 Hz

The transmitted square wave signal from the *n*th luminaire (*n* =1 to 4) can be expressed in Fourier series expansion [46]:

$$s_n(t) = A_n \sum_{q=1}^{\infty} \left(rect\left[\frac{t-\frac{qT_n}{4}}{\frac{T_n}{2}}\right] - rect\left[\frac{t-\frac{3qT_n}{4}}{\frac{T_n}{2}}\right] \right) \tag{3.1}$$

$$s_n(t) = \sum_{l,odd}^{\infty} C_n^l exp[j2\pi l f_n t] \tag{3.2}$$

$C_n^l = \frac{2A_n}{jl\pi}$ is the Fourier series coefficient and f_n is the fundamental frequency for the n^{th} luminaire.

This modulator uses frequency division multiplexing (FDM) scheme to transmit the light signals. Because $s_n(t)$ contains only odd harmonics of f_n , as such the modulation frequency f_n of the n^{th} luminaire is chosen to be the second harmonic of f_{n-1} , the modulating frequency of the $(n\text{-}1)^{th}$ luminaire. This is to make sure that the harmonics of a luminaire does not interfere with the fundamental frequency of any other luminaire. This basically explains the rational of using the 800 Hz, 1600 Hz, 3200 Hz and 6400 Hz to drive these 4 lights sources.

However, it is possible to choose fundamental modulation frequencies that are 50 Hz apart as long as they do not interfere with the odd harmonics of other modulating frequencies. For example, if using frequencies between 800 Hz and 2 kHz at 50 Hz interval, there will be 25 noninterfering modulating frequencies available to choose from. The aforementioned 4 frequencies were chosen after considering several factors. The highest frequency needs to be lower than the response time and the slew rate of the LED luminaires. The lowest frequency should have enough separation from the 100 Hz interference present in regular lighting infrastructure [46].

There are reports about harmful effect of flicker on human health from headache, blurred vision, eye strain to seizure [47, 48]. These light flickering frequencies can range from as low as 3Hz and up to 200Hz. At location (x_i, y_i), the received signal at the output of the photodiode from the n^{th} luminaire is given by-

$$r_{n,i}(t) = \sum_{l,odd}^{\infty} G_{n,i}^{l} C_n^l exp[j2\pi l f_n t] \tag{3.3}$$

$G_{n,i}^l$ is a factor that depends on the response of the photodiode at the frequency lf_n and the optical channel between the luminaire n and the location (x_i, y_i).

$r_{n,i}(t)$ is passed through a bank of 4 parallel bandpass filters each centered at the fundamental frequency f_n. The output of the bandpass filters can be written as-

$$R_{n,i} = H_n G_{n,i}^l C_n^l \tag{3.4}$$

H_n is the gain of the bandpass filter for the centre frequency f_n. For flexibility and the ease of implementation, the Fast Fourier Transform (FFT) operation was used which samples the spectrum to perform the bandpass filtering. Alternatively, these fundamental frequencies can be filtered through the use of hardware circuitries composed of cheap, passive analog bandpass filters. The experiment set up in Figure 3.7 shows the receive signal strength, $|R_{n,i}|$ where (n =1 to 4) at one test location. As can be seen, the values are strong at the vicinity of the n^{th} luminaire and get weaker moving further away. The $P_{n,i} = |R_{n,i}|^2$ at each point on the grid is an estimate of the RSS for the corresponding luminaire and a location vector ID can be assigned as:

$$\mathrm{P}_i = [P_{1,i}, P_{2,i} \quad \cdots, \quad P_{N,i}]^T \tag{3.5}$$

where N= 4 as there are 4 four LED light sources in this case

The sampling frequency of ADC at the receiver board which contains ARM Cortex M4 microcontroller is set at 31250 Hz. This sampling rate is chosen because it is significantly greater than the Nyquist theorem requirement for the incoming signal which is 12800 Hz (2x

6400Hz). The samples are buffered into frames of 625 samples that are used for the Fast Fourier Transform (FFT). The FFT operation can be performed on board of the target device or at the computer. For less powerful devices, all of the computation including the FFT can be performed at the computer as long as the received signal samples are transmitted back. However, this will increase the wireless transmission data rate and the energy consumption associated with the transmission [46].

The receiver hardware module to receive the optical signals is shown in Figure 3.8. To better visualise the result, MATLAB tool is used to provide various useful plots such as heat map of a luminaire, 3D plot of light intensity and others. Figure 3.9 shows the heat map of the frequency magnitude of the 3200 Hz luminaire when the measurements are taken at every intersection of the 10cm x 10cm grid. It can be observed that the received signal is the strongest at the lower left hand corner where the LED3 is located. The light magnitude falls off as the distance between the detector and the LED light source increases. Figure 3.10 demonstrates the 3D plot of light fall off model or Lambertian model [49] from LED3 which transmits light frequency at 3200 Hz. Similarly, the light intensity plots can be observed from the other 3 frequencies.

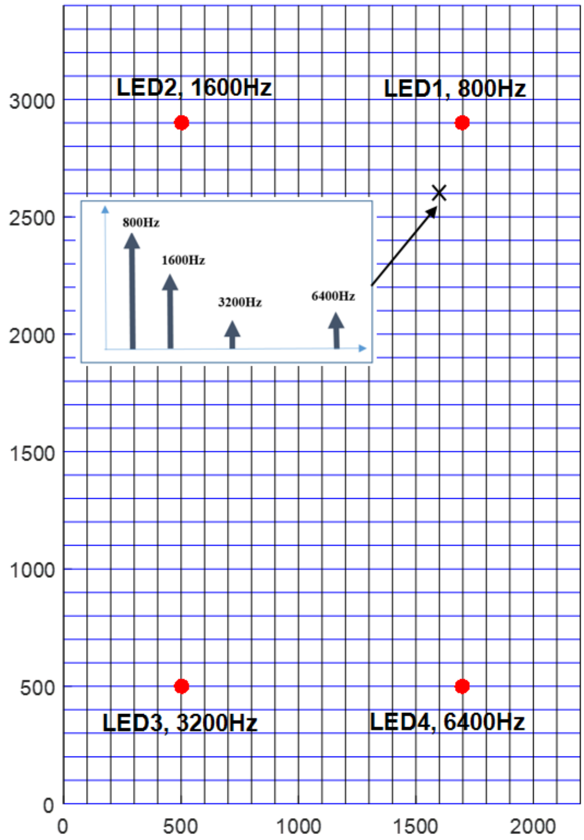

Fig. 3.7 Frequency components at one location of the test bed (3.4m x 2.2m)

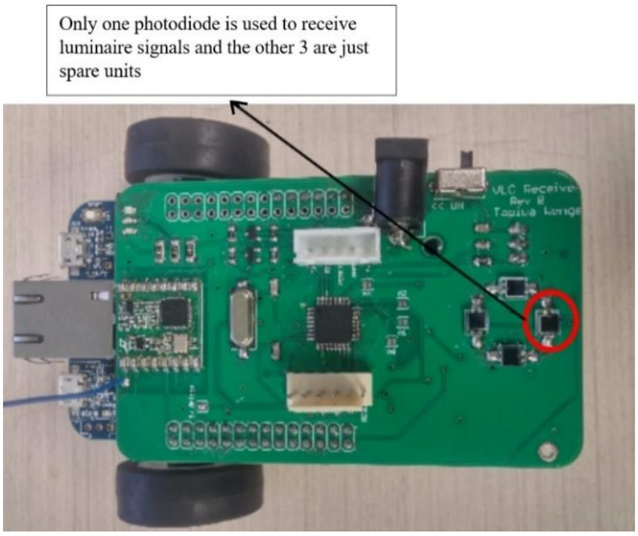

Only one photodiode is used to receive luminaire signals and the other 3 are just spare units

Fig. 3.8 VLC Receiver hardware circuit where the photodiode and amplifier are on the top level board and the 16-bit ADC is provided by the bottom level board - K64F development board (also refer to Receiver System Block from Fig.3.4)

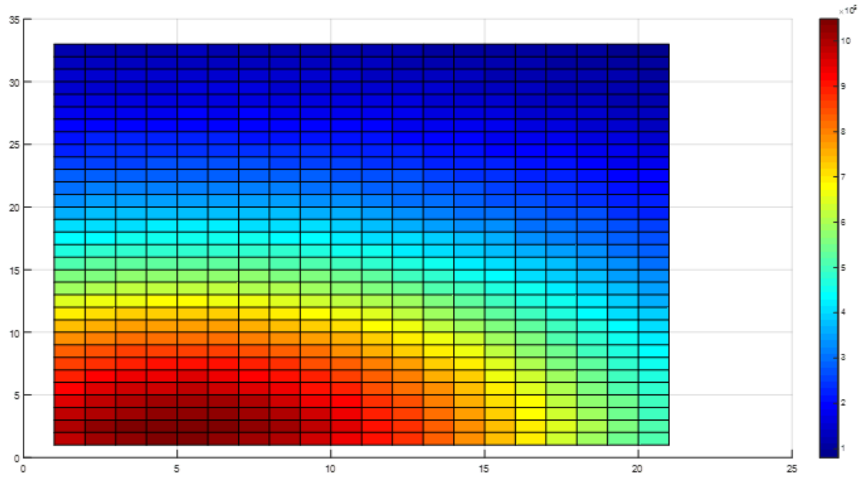

Fig. 3.9 The heat map for LED 3 -3200Hz (on 3.4m x 2.2 m floor space)

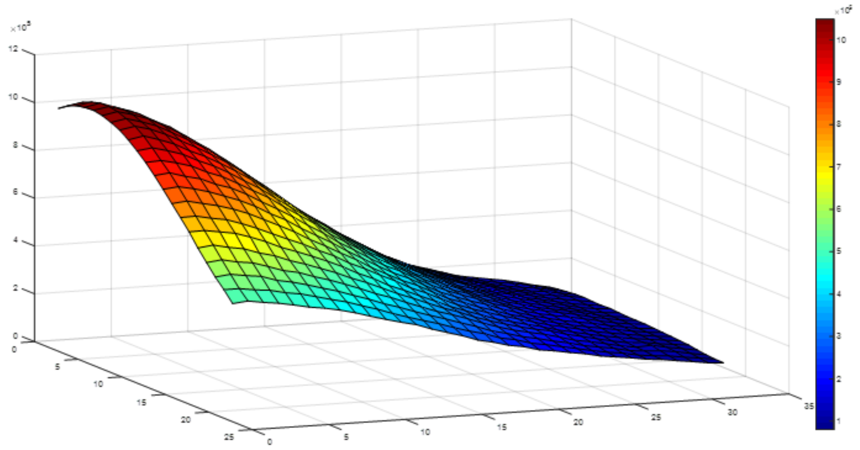

Fig. 3.10. Light magnitude falloff - LED 3, 3200Hz

3.3 Weighted K-Nearest-Neighbour

After the fingerprinting map has been constructed from the offline data collection at selected locations and identified by their individual unique ID information as in equation (3.5), the location of the mobile receiver can be estimated during the live phase using the weighted KNN algorithm. The ID vector received by the detector at a location (x_j ,y_j) during the live phase is given by-

$$\mathrm{P}_j^{live} = \left[P_{1,j}^{live}, P_{2,j}^{live} \quad \cdots, \quad P_{N,j}^{live}\right]^T \tag{3.6}$$

The Euclidean distance $d_{j,i}$ of the live ID vector P_j^{live} to the ID vector P_i of the offline database is given by-

$$d_{j,i} = \sqrt{\sum_{n=1}^{N}\left(P_{n,j}^{live} - P_{n,i}\right)^2} \tag{3.7}$$

where $i = 0,1,2,3, \ldots\ldots, z$ and z is the number of locations recorded in the offline database. $n = 1,2,3, N = 4$ indicating the 4 different frequency magnitude within an ID vector.

The proximity of the live location to every location on the database are determined by $d_{j,i}$. The weighted KNN algorithm estimates the location of the receiver ($\tilde{x}_j, \tilde{y}_j$) as the weighted average of the location of the K nearest neighbours. The nearest neighbours are the K offline locations that produce the smallest $d_{j,i}$ values. The value of K needs to be judiciously selected to produce the optimum results. The estimated location of the receiver ($\tilde{x}_j, \tilde{y}_j$) is given by-

$$\widetilde{x_J} = \frac{\sum_{k=1}^{K} w_{j,k} \times x_k}{\sum_{k=1}^{K} w_{j,k}} \quad , \quad \widetilde{y_J} = \frac{\sum_{k=1}^{K} w_{j,k} \times y_k}{\sum_{k=1}^{K} w_{j,k}} \tag{3.8}$$

Here (x_k, y_k) is the location of the k^{th} neighbor. The weight $w_{j,k}$ is the reciprocal of the distance calculated by equation (3.7). K= 4 was used in the experiments as that produced the highest accuracy as shown in Figure 3.11.

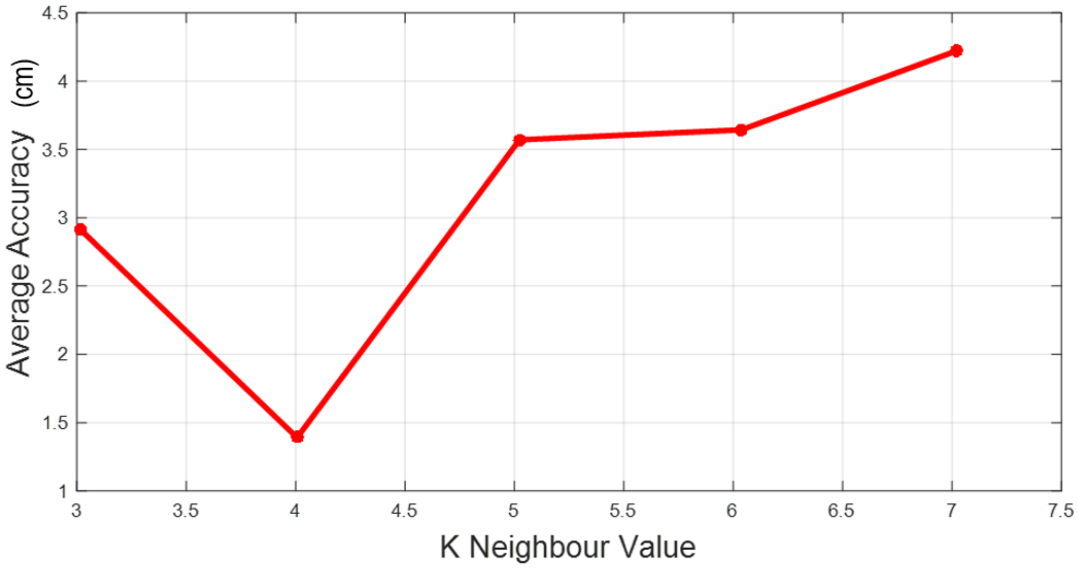

Fig. 3.11 Average accuracy vs K value for 20cm x10cm grid space database

3.4 Impact of offline database size

Altogether, there were 693 equal spaced measurements taken within the 3.4m x 2.2m floor map as shown in Figure 3.1 and Figure 3.7. There was no measurement done along the boundaries of the testbed. This resulted in 33x21= 693 measurements within a grid of 3.3m x 2.1m. The number of measurement points used to construct the offline fingerprinting database is 345 and the rest were designated for online or live data validation. The approximate time taken to collect each data point was 17 seconds. For the experiments, the photo sensing device was moved manually from one point to another and all the time ensuring the receiver was not tilted. In the real world, this can be achieved by simple gimbal.

To construct a database with 20cm x 10cm space grid size, it will result in data collection at 345 points at the designated floor space. The total time spent to build this database is 1hour and 38 minutes. The mean and median accuracy achieved were 1.39cm and 0.46cm respectively. For the experimental setup, there is no measurable improvement in accuracy for <20cm spacing. The lower bound of the localization accuracy is set by several factors. Reflection and multipath resulting from different type of objects present in the room contribute to the error. Given the cheap photodiode used in the receiver, the orientation of the receiver has an impact on the received signal strength. So, if the orientation of the receiver is not kept exactly the same during the offline calibration and the online phase, there will be some error in the localization. It is also assumed that the receiver plane remains at the same level for all measurements. However, this is difficult to maintain and the floor and ceiling planes may not be exactly parallel to each other over the entire test bed. This discrepancy also contributed to the error. Saturation due to ambient light, the noise floor of the hardware and the resolution of the A/D converter also contributed to the overall error. Figure 3.12 shows the distribution of the errors for 20cm x10cm database. As can be observed, the majority of the errors are quite small and they fall within the 2cm range.

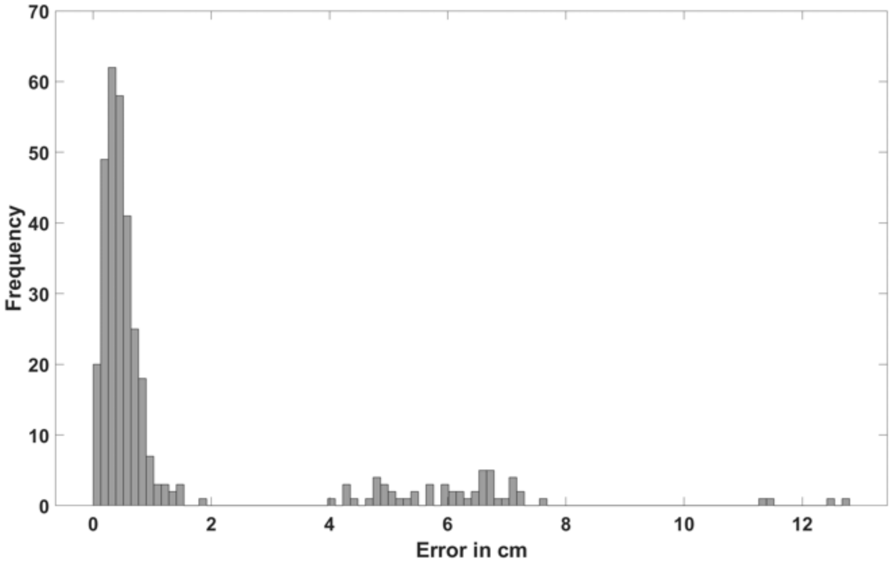

Fig.3.12 Error distribution for the 20x10 database

Table 3.1 summarizes the results for different offline databases. As the size of the database decreases, the accuracy of the localization system becomes poorer. However smaller databases require less offline measurements. So there is an obvious trade off between accuracy and time spent in offline measurement.

Table 3.1 Summary of errors

Spacing (cm)	Mean (cm)	Median (cm)	No. of off-line points	Construction time (min)
20	1.39	0.46	345	98
30	4.50	2.70	219	62
40	4.90	4.70	170	49
50	6.80	6.80	137	39

3.5 Impact of the number of luminiares

The experimental results in Table 3.1 show that VLC-based technology has the potential to replace other technology in precise indoor localization for robotics. This is because the LED light sources are very popular nowadays and will soon become ubiquitous feautures in buidlings of all types from offices, residential homes, hotels, hospitals to factories. Quite often with any lighting in the building, there bound to be one or two lights which are not operational due to wear and tear after some period of time. It is important to see if the VLC-based localization system is able to withstand under those faulty circumstances. The experiment has been conducted to test how tolerant is the developed system in identifying the mobile robot's position. Table 3.2 shows the various situations when one of these 4 LEDs is broken.

Table 3.2 Position error when one of the 4 LEDs is unavailable

LED Light sources	1,2,3	1,2,4	1,3,4	2,3,4
Mean (cm)	2.9118	2 .5907	3.7010	4.0685
Median (cm)	1.6949	2.5815	2.1823	2.3486
90 percentile(cm)	6.4992	6.0162	8.0911	9.5109
Min (cm)	0.0339	0.0095	0.0505	0.1426
Max (cm)	23.2943	23.2165	35.6900	29.5759
Std Dev (cm)	3.3956	2.7710	4.3487	4.8489

The data in Table 3.2 is based on 345 fingerprinting data point entries and resulting in average mean error of 3.318 cm and average 90 percentile error value of 7.529cm. If this localization technique is used to determine the mobile unit's position within a floor space which has grid or cell size of 20cm x 20cm, then this error is within the acceptable range because it is less than half the cell size. The result shows that even in the situation when one of the lights is off, the mobile unit or robot is still able to localise itself using the 3 remaining lights within its vicinity.

3.6 Impact of the Distance Metric

Distance measure or sometime referred as distance metric, is important when it comes to solving problem based on machine learning, pattern recognition and matching algorithm. The performance of these classifiers relies on the how accurate is the distance measured between the test location and the training set locations in the database. There are huge variety of distance measures [50, 51] to choose from beside the commonly used Euclidean Distance. The various distance metrics used in this work and their definitions are given in Table 3.3.

Table 3.3 Summary of localization error for various distance metrics. $K = 4$ [52]

Distance Metric	Definition	Localization Error in cm					
		20 cm x 20 cm Grid		50 cm x 50 cm Grid		100 cm x 100 cm Grid	
		Mean	90 Perc.	Mean	90 Perc.	Mean	90 Perc.
Euclidean (ED)	$d_{j,i} = \sqrt{\sum_{n=1}^{N} \left(P_{n,j}^{live} - P_{n,i}\right)^2}$	2.8	7.5	10.6	18.4	24.1	44.3
Squared Euclidean (SED)	$d_{j,i} = \sum_{n=1}^{N} \left(P_{n,j}^{live} - P_{n,i}\right)^2$	2.4	5.4	8.5	14.5	18.1	38
Manhattan (MD)	$d_{j,i} = \sum_{n=1}^{N} \lvert P_{n,j}^{live} - P_{n,i}\rvert$	3	7.1	10.5	18.3	23.8	47.9
Matusita (MtD)	$d_{j,i} = \sqrt{\sum_{n=1}^{N} \left(\sqrt{P_{n,j}^{live}} - \sqrt{P_{n,i}}\right)^2}$	2.9	7.2	8.4	13.9	19.9	32.7
Squared Chord (SCD)	$d_{j,i} = \sum_{n=1}^{N} \left(\sqrt{P_{n,j}^{live}} - \sqrt{P_{n,i}}\right)^2$	2.2	4.9	6.5	10.4	13.5	24.6
Chebychev (ChD)	$d_{j,i} = \max_{n} \lvert P_{n,j}^{live} - P_{n,i}\rvert$	3.4	8.5	12.7	22.9	25.3	47
Cosine (CoD)	$d_{j,i} = 1 - \frac{\sum_n^N P_{n,j}^{live} P_{n,i}}{\sqrt{\sum_n^N P_{n,j}^{live}}\sqrt{\sum_n^N P_{n,i}}}$	4.1	8.2	10.1	18.5	21.2	40.6
Squared Chi-Squared (SCSD)	$d_{j,i} = \sum_{n}^{N} \frac{\left(P_{n,j}^{live} - P_{n,i}\right)^2}{\lvert P_{n,j}^{live} + P_{n,i}\rvert}$	2.2	4.9	6.5	10.5	13.8	25
Canberra (CD)	$d_{j,i} = \sum_{n}^{N} \frac{\lvert P_{n,j}^{live} - P_{n,i}\rvert}{\lvert P_{n,j}^{live} + P_{n,i}\rvert}$	2.5	7.2	9.7	17.5	23.3	37.9
Lorentzian	$\sum_{n=1}^{N} log\left(1 + \lvert P_{n,j}^{live} - P_{n,i}\rvert\right)$	3.5	7.8	12.9	22.7	29.5	54

However, only the best performing ten distance metrics are presented out of the thirty-seven that were investigated. Using the same localization test rig (3.4m x 2.2m floor space) as in section 3.1, an experiment was carried out to compare the robustness of 9 other distance metrics with the Euclidean Distance used previously. Table 3.3 shows the localization accuracy results using 3 different grid sizes (20cm x 20cm, 50cm x 50cm and 100cm x 100cm).

Interestingly, the Table 3.3 shows that Euclidean Distance (ED) is not the most accurate or robust metric for computing the weights for Weighted K-nearest Neighbour (WKNN) classifier. Squared Chord Distance (SCD) and Squared Chi-Squared Distance (SCSD) produce the lowest localization error. Furthermore as the grid size becomes wider, ED's accuracy drops substantially when compared with SCD and SCSD. As for this work, only results obtained for SCD are presented, and where necessary results corresponding to ED are presented for some selected cases for comparison purposes.

Fig.3.13 shows the precision of the localization system in the form of the Cumulative Distribution Function (CDF) of the localization error for ED and SCD for various grid sizes. It can be observed that the SCD performs better than ED and denser grid leads to better performance. The number of nearest neighbour, *K*, is four in all experiments as that seems to be the optimum value for this data set and provide the lowest mean error (see Fig. 3.14).

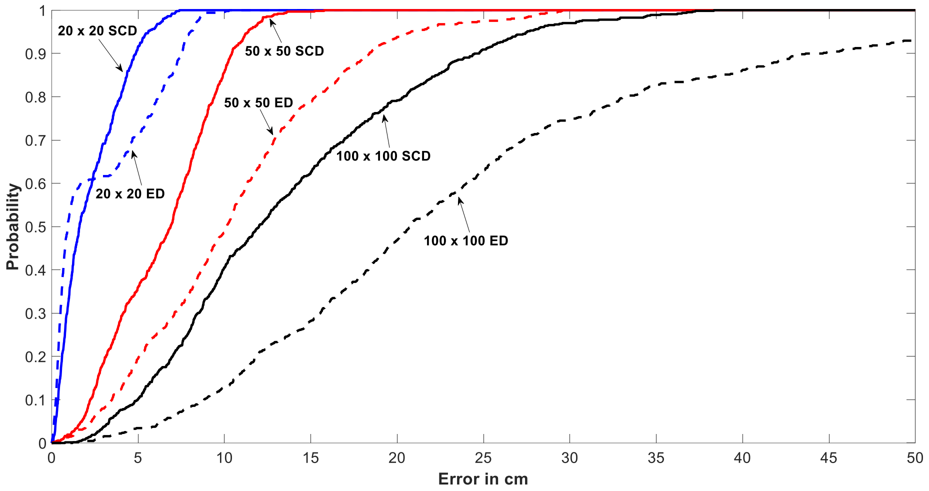

Fig. 3.13 Localization precision for Euclidean and Square Chord distance metrics for various grid sizes. K=4

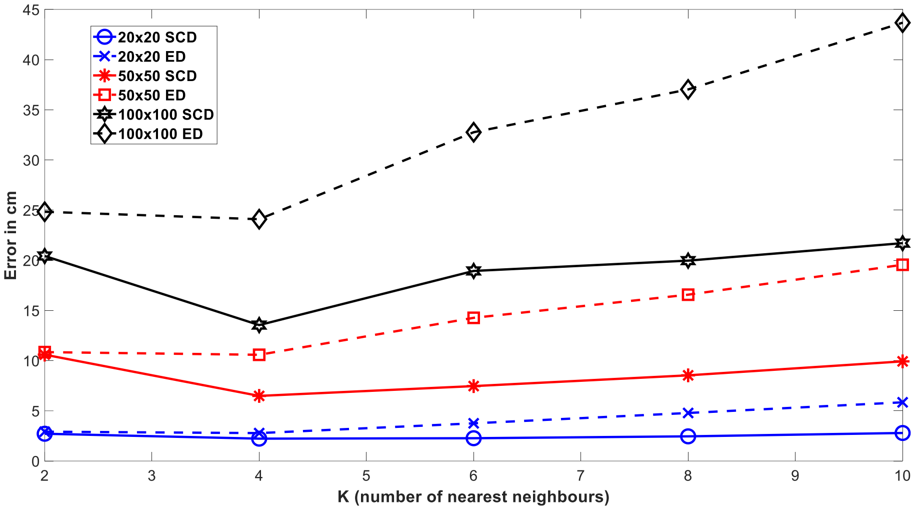

Fig.3.14 Impact of K on the mean error for Euclidean and Square Chord distance metrics for various grid sizes

3.7 Summary

It can be seen that the practical implementation of VLP system based on WKNN technique does give reasonable position accuracy. It also demonstrates the impact of distance metric on the performance of WKNN algorithm for a VLP. The investigation shows that Squared Chord distance is the most robust distance metric for the developed VLP and provides better localization accuracy than the commonly used Euclidean distance.

This experiment focused on the use of Frequency Division Multiplexer (FDM) to implement the VLP system due to it being one of the most common and simplest modulation schemes for data transmission. In this case, square wave on-off keying modulation frequencies were generated from modulator circuits to drive the LED sources. The signal frequencies chosen were in even multiples of the first fundamental frequency of 800Hz, this is so that the inherent odd harmonics that exist in one signal did not interfere with another fundamental signal.

However, using square wave test rig has its downside, besides the square wave modulation with 50% duty cycle results in a loss of half the total illumination, it also restricts the number of frequencies that can be used for transmitters identification. Hence it is not suitable if VLP system is expanded or upscaled. By moving to a sine wave modulation, it would remove this restriction and allow as many frequencies to be used as identification signals for the light sources. Hence, subsequent experiments on VLP described in Chapter 4 and Chapter 5, are based on different modulating sine wave frequencies implementing on FDM modulation scheme, and on different test rig platform sizes.

Chapter 4 - Visible Light Positioning Based Robot Localization and Navigation.

This chapter reports on the successful experimental performance of using Visible Light Positioning (VLP) as a global guiding system for indoor robot localization and navigation. Recent literature shows a small number of works on robots being controlled by fusing location information acquired by VLP that uses rolling shutter effect camera as a receiver with other sensor data. This thesis, in contrast, reports the experimental performance of a cartesian robot that was controlled solely by a VLP system using a cheap photodiode-based receiver rigidly attached to the robot's end effector. The receiver's position was computed using an inverse-Lambertian function for ranging followed by multi-lateration. Two novel methods to leverage the VLP as an online navigation system to control the robot were developed. The position acquired from the VLP was used by the two algorithms (which are based on Direct and Spring Relaxation Methods) to determine the direction the robot needed to move. The developed algorithms guide the end effector to move from a starting point to target/destination point(s) in a discrete manner, determined by a pre-determined step size. The results show median errors of 27.16 mm and 26.05 mm and 90 percentile errors of 37.04 mm and 47.48 mm respectively for the two methods.

4.1 Related Work

In VLP systems, LED luminaires are used as the transmitting beacons with either a photo diode (PD) or camera as the common receiver sensor attached to the tracked object. Both sensors come with inherent advantages and disadvantages. While cameras may allow for more sophisticated communication schemes [13], PD-based receivers are considerably cheaper and energy efficient [14], and incur less computational cost [15]. Received signal strength (RSS) is the most widely utilized signal characteristic for a PD-based VLP due to simplicity and convenience [28]. VLP that utilizes RSS can either be model- or fingerprinting-based [53]. Fingerprinting-based methods can be time- and labour-consuming compared to the model-based [52] ones. Considering all these points, the VLP system used for this work employed a PD-based receiver that utilizes RSS as the signal characteristic and localizes using a model-based technique. A literature review shows many localization works based on a PD-based receiver that utilises RSS (for example, see the recent survey paper by Rahman et al. [54] on

VLP) achieving centimeter-level accuracy. However, there is no reported work that uses such a VLP system as the singular tool for controlling robots in real time.

A survey of recent literature on VLP-based indoor robot navigation yields only a handful of papers. These works utilize a rolling shutter effect (RSE) camera as the light sensing device (please see [55-57] for examples of RSE-based VLP systems). Though the method uses more computer computation time and a complex algorithm because of the involvement of image processing and classification algorithm, the availability of ubiquitous CMOS image sensor cameras in most smartphones has made them the preferred choice among researchers.

Rátosi and Simon [58] employed an RSE camera installed on a mobile robot to determine its pose from the signal received from modulated LED luminaires. While the system is shown to be able to track the moving robot in real time in a 6 m × 6 m room within a low centimeter range, the VLP system is not used for the navigation. The process of decoding LED-ID information from the captured images using an RSE camera can be slow due to the computational latency. Therefore, Li et al. [59] proposed using convolutional neural network (CNN) to increase the speed of identifying the anchor node ID from the captured image, especially with motion blur caused by the fast movement of a robot.

Hua et al. [60] proposed the fusion of a PD- and camera-based system using a version of the Kalman filter. The system is shown to be robust and has the ability to perform real-time positioning. However, the system was not used to control or navigate a robot. Amsters et al. [15] demonstrated the capability of a PD-based VLP that utilizes only unmodulated light. While their system has the potential to estimate the pose of a mobile robot, the experimental results do not show real-time position estimation. They also do not control or navigate the robot using VLP. Zhuang et al. [61] reported on a PD-based VLP system that may be used for the localization of a mobile robot. However, the article only reports localization accuracy; the VLP system is not used to control the movement of the robot.

Guang et al. [62] proposed indoor robot localization based on a VLP system that utilized an RSE camera installed on Turtlebot 3 running a robot operating system (ROS). They presented an extension [63] of this work by introducing a loosely coupled multi-sensor fusion with LiDAR- based SLAM and odometry. Another improvement [64] of the work involves the fusion of VLP and IMU to improve the system's robustness with the ability to handle luminaire shortage/outage. A similar work on the fusion of VLP and IMU to address luminaire shortage/outage issues for an RSE-based receiver can be found in [65]. It should be noted that only one of the articles [64] develops a method for controlling the robot, whereas the other two articles [63-65] focus mainly on the localization aspect.

Therefore, a clear gap in the state of the art can be seen. There is a noticeable lack of works that utilize VLP for controlling a robot. Recent literature shows only a small number of works on robots being controlled by fusing location information acquired via VLP that uses an RSE camera as a receiver with other sensor data. There is no reported work that has used only PD-based VLP to control a robot. This is the motivation of the work being presented in this thesis.

4.2 Contribution

This is the first reported work that utilizes only a PD-based VLP system to control the movement of a robot. In this work, two novel algorithms are proposed and implemented to control the movement of a cartesian robot, constructed in the form of a 2D Computer Numerical Control (CNC) machine, solely by a VLP system in real time. This also allows for objectively evaluating the efficacy of a PD-based VLP system for controlling a robot. Based on the experimental results collected while the robot is traversing multiple path patterns, both algorithms show promising accuracy.

4.3 Experiment Setup

The key equipment of the experimental setup is a purpose-built 2D CNC machine (see Figure 4.1). The VLP photodiode receiver is mounted on the end effector. The CNC machine performs three important tasks:

- It acts as the online robotic platform where the end effector is driven by the VLP system;
- The encoders of the CNC measure the X Y linear movement at the rate of 1000 mm per minute;
- During the online phase, the CNC also records the exact locations of the receiver (end effector). The location information is not used by the VLP system to drive the CNC, but it is used as the ground truth so that the localization accuracy or error statistics can be computed;
- During the offline phase, the CNC is used to accurately position the VLP receiver at 29 pre-determined locations to collect RSS data for calibrating the Optical Propagation Model of the VLP system.

The end effector's minimum step size is 0.1 mm, achieved through lead screw actuation and Nema 23 stepper motors. An OpenBuilds BlackBox Motion Control System (MCS) with Grbl firmware controls the stepper motors. The host PC sends commands to the BlackBox MCS over a USB, with desired positions converted into GCODE commands via a Python program. These desired positions were computed by the VLP.

The VLP system consists of four transmitters constructed with LED luminaires which are commercially available and can be bought easily off the shelf. These luminaires are placed at a 1050 mm height above the CNC at known x–y locations: TX1 (0, 0), TX2 (0, 780), TX3 (760, 780), and TX4 (760, 0) (see Figure 4.1).

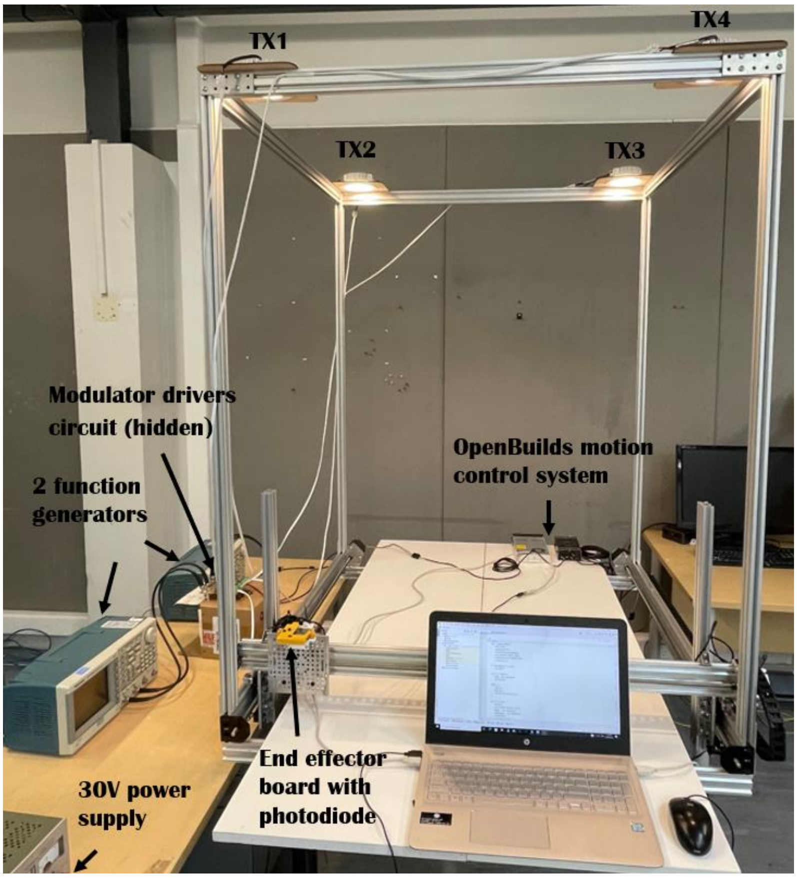

Fig.4.1 VLP system test rig

For the experiments conducted, an unmodulated sine wave of frequencies of 2 kHz, 2.6 kHz, 3.2 kHz, and 4.4 kHz were inserted by a modulator driver circuit powered by a 30 V power supply (shown in Figure 4.2). The input of the modulator circuit is connected to a function generator which supplies the required sine wave. Each function generator has two signal generation channels. Altogether, two function generators are sufficient for this experiment (as seen in Figure 4.1).

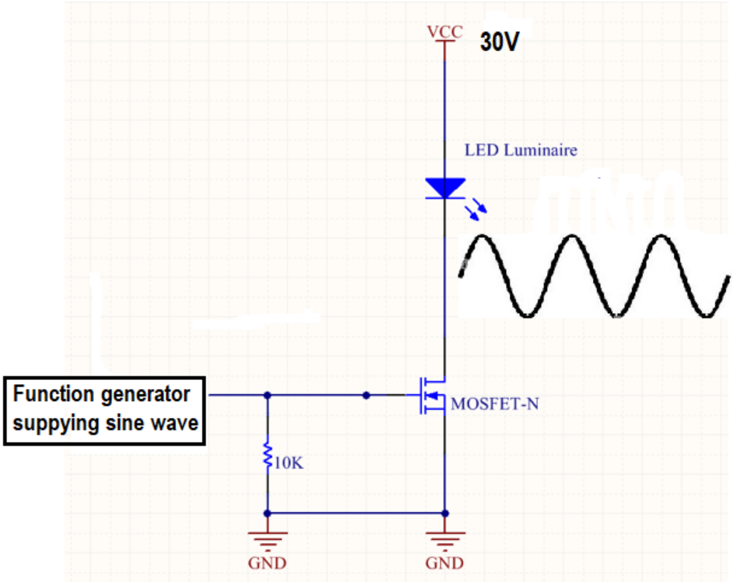

Fig. 4.2. Modulator driver circuit

Underneath, the PD-based VLP receiver was mounted on the end effector of the CNC. Together they form the robot that is controlled by utilizing the location estimated with respect to the fixed luminaires. On the receiver board, the photodiode sensor converted the optical signal to an electrical signal which was then amplified through a transimpedance amplifier before being processed by an onboard analog to digital convertor (ADC). More details of the receiver board can be found in [12]. The sensor board receives and decodes the identities of these four lights using a Python program in the PC. After that, the data are transmitted out serially via USB to PC for Fast Fourier Transform (FFT) processing. The function of the FFT is to demultiplex and measure the magnitude of the four sinewaves present in the received signal [12]. The magnitude squares constitute the RSS set at each location. Please refer to Figure 4.3 for more details of the operation of the VLP system.

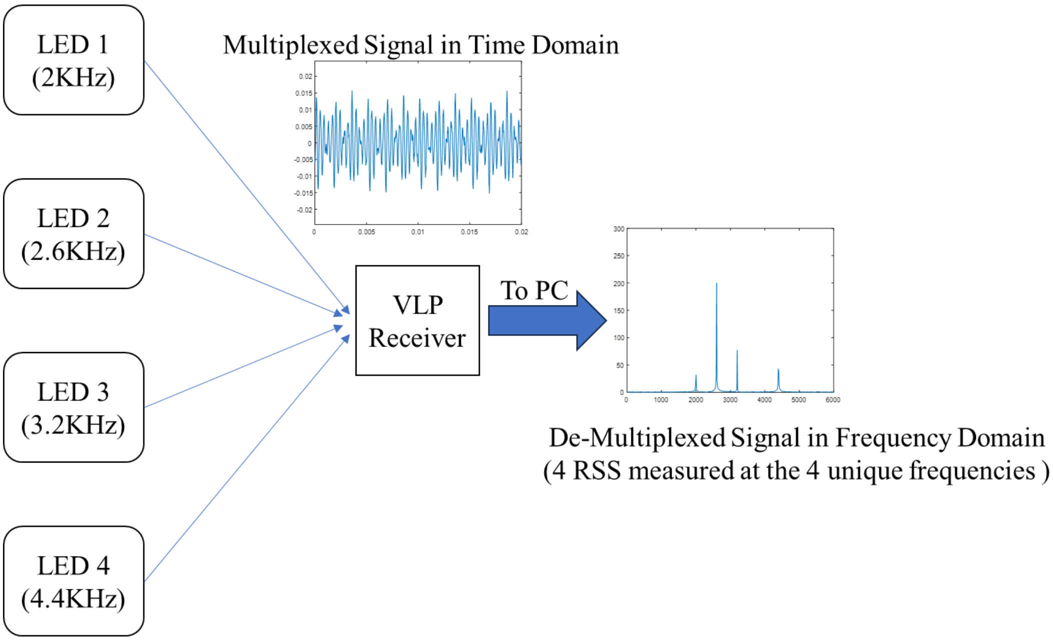

Fig. 4.3 Key concept of the VLP system. RSS is extracted from the received signal using FFT. A representative RSS from four visible luminaires is shown at the receiver at a particular location. The measured RSS is used for model calibration during the offline stage and for ranging and localization during the live stage

4.4 Localization Using VLP

During the offline stage, the RSS–distance relationship is found by calibrating the Lambertian propagation model. RSS data are collected at a set number of pre-determined locations for the parameter calibration. During the online phase, the live RSS readings are used to find the distance of the target device (the receiver on the end effector) from each transmitter by "inverting" this calibrated propagation model. Subsequently, the receiver's position is estimated via lateration.

4.4.1 Offline Calibration of VLP

For this research, the receiver/target plane and luminaire/transmitter plane are kept horizontal with respect to one another. This allows for the simplification of the Lambertian propagation model [53]. Please refer to the discussion in Section 4.7 on how this limitation can be addressed in the future.

Under this assumption of a parallel arrangement, the received power, P_{r_i} , or the RSS at a distance d_i from the i^{th} luminaire (Figure 4.4) within the field of view of the luminaire can be simplified from the Lambertian propagation model following the process outlined in [53].

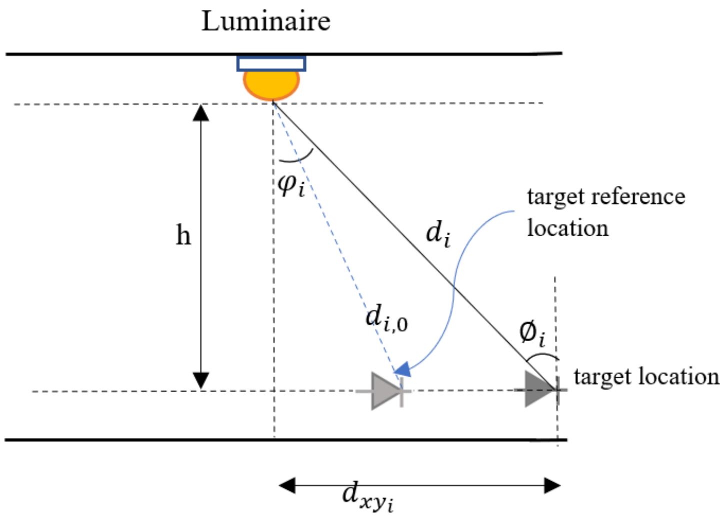

Fig. 4.4 Parameters of the Lambertian propagation model

$$P_{r_i} = P_{r_{i,0}} \left(\frac{d_{i,0}}{d_i}\right)^{m_i+3} \tag{4.1}$$

Here, m_i is the Lambertian order and $P_{r_{i,0}}$ is the RSS at a *reference* location at a distance $d_{i,0}$ from the target. Equation (4.1) can be rearranged so that

$$m_i = \left[\frac{log\left(\frac{P_{r_i}}{P_{r_{i,0}}}\right)}{log\left(\frac{d_{i,0}}{d_i}\right)}\right] - 3 \tag{4.2}$$

The received signal at the receiver at location (x, y) can be expressed as:

$$s(t) = \sum_{i=1}^{4} G_i \sin(2\pi f_i t + \theta_i), \tag{4.3}$$

where f_i and θ_i are respectively the frequency and phase of the sinewave of the i^{th} luminaire at location (x, y) and G_i is essentially a function of the distance d_i between the photodiode at location (x, y) and the i^{th} luminaire.

The spectrum $\mathrm{S}(\omega)$ of the signal at angular frequencies ω can be computed using the Fast Fourier Transform (FFT). The power spectrum can then be calculated using:

$$\widehat{\mathrm{P}}_{ss}(\omega) = \frac{1}{N}|\mathrm{S}(\omega)|^2. \tag{4.4}$$

The power spectrum, $\widehat{\mathrm{P}}_{ss}(\omega)$, at the known modulation frequencies (2, 2.6, 3.2 and 4.4 kHz) are used to estimate the received power $P_{r_i}(d_i)$ for each luminaire.

Figure 4.5 shows the position of the 29 offline locations where the RSS values were collected to estimate m_i for calibrating the RSS–distance relationship. As suggested by [52], the reference location is chosen directly underneath the corresponding luminaire. The Lambertian order is estimated at the rest of the 28 locations using Equation (4.2), and then averaged over these 28 values. These offline locations are carefully chosen so that all regions of the Lambertian propagation models for each luminaire are captured [22]. Table 4.1 shows the estimated Lambertian order and Figure 4.6 shows the measured RSS values and the calibrated RSS–distance Lambertian curves of the four luminaires.

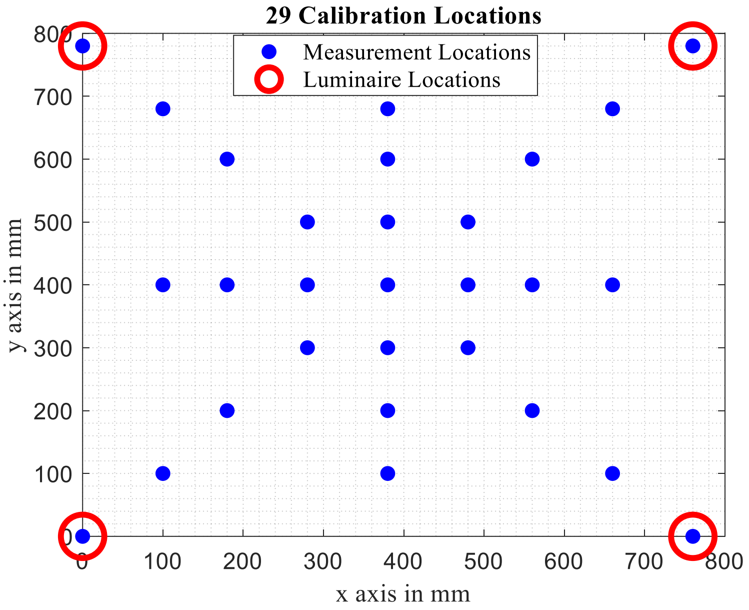

Fig.4.5 The location of the luminaires and the 29 measurement locations for offline parameter calibration of the Lambertian propagation model

Table 4.1: Estimated Lambertian order of the luminaires

Luminaire	Lambertian Order (m_n)
1	4.5998
2	3.9798
3	3.1961
4	3.5810

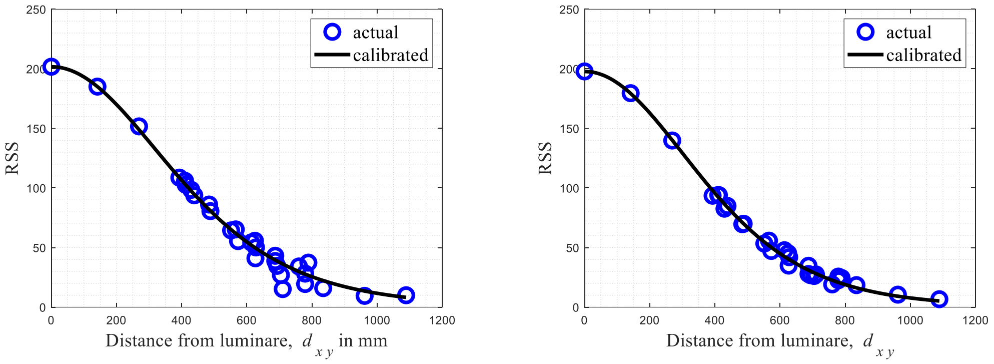

(**a**) Luminaire 1 (**b**) Luminaire 2

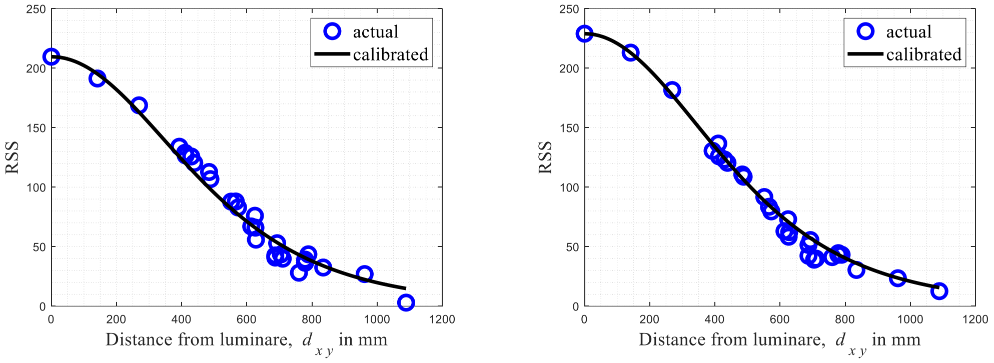

(**c**) Luminaire 3 (**d**) Luminaire 4

Fig. 4.6 Calibration of the Lambertian propagation models for the four luminaires

4.4.2 Online Localization Using VLP

Once the RSS–distance model is calibrated for each luminaire, Equation (4.1) can be rearranged for ranging (i.e., to compute the distance of the target from a luminaire) so that

$$d_i = d_{i,0}\left(\frac{P_{r_{i,0}}}{P_{r_i}}\right)^{1/(m_i+3)}, \tag{4.5}$$

The horizontal distance of the target from the i^{th} luminaire, d_{xyi} (please see Figure 4.4) is computed as

$$d_{xyi} = \sqrt{d_i^2 - h^2} \tag{4.6}$$

4.5 Online Navigation

Two algorithms were developed that can guide the end effector to move from a starting point to the target/destination point(s). Both algorithms drive and make the end effector move in a discrete manner, determined by the step size.

At each iteration of the algorithm, (1) visible light signal is captured by the VLP receiver (for 500 ms) and sent to the PC for extraction of RSS, (2) the distance of the end effector from each luminaire is determined (as per the procedure discussed in the previous section), and (3) the end effector is instructed to move by a step size toward a direction as determined by the algorithm or to remain stationary if the destination is reached. To maneuver the CNC machine, a GCODE set is needed to be sent to the OpenBuilds BlackBox motion control driver. The main program which is written in Python works out the x and y direction step movement from the algorithm and generates the equivalent steps in GCODE. The Black box motion control driver then processes the given GCODE and commands the movement of the stepper motors connected to the CNC machine.

4.5.1 Algorithm 1 (Direct Method)

The flowchart in Figure 4.7 shows the algorithm. The robot, if required, moves at a step size of *T*. However, before any movement takes place,

(i) The robot's current distance from each luminaire's position is determined using live VLP reading following the process outlined in Section 4.4.2. Once the horizontal distance of the target from all four luminaires is found, the location of the target on the xy plane is estimated using multi-lateration [59].

(ii) The direct distance between the current position and the final destination position (see Figure 4.8) Δxy , is calculated. Δxy is based on the difference in x distance, Δx and the difference in y distance, which is Δy, so that $\Delta xy = \sqrt{\Delta x^2 + \Delta y^2}$.

(iii) If $\Delta xy \leq T$, the robot is considered to have reached the target, otherwise (i.e., if $\Delta xy > T$) the robot receiver has not reached the destination yet and moves to a new position by moving x_s and y_s in the x and the y directions, respectively. Here $x_s = \frac{\Delta x}{\Delta xy} \times T$ and $y_s = \frac{\Delta y}{\Delta xy} \times T$. As discussed previously, *T* is the step size (which is 20 mm for the experiments). It should be noted that

1. if $x_s = +ve$, the robot moves to the right;
2. if $x_s = -ve$, the robot moves to the left;
3. if $y_s = +ve$, the robot moves up;
4. if $y_s = -ve$, the robot moves down.

Once arriving at the new position, steps (i)–(iii) are reiterated until the robot arrives at its destination.

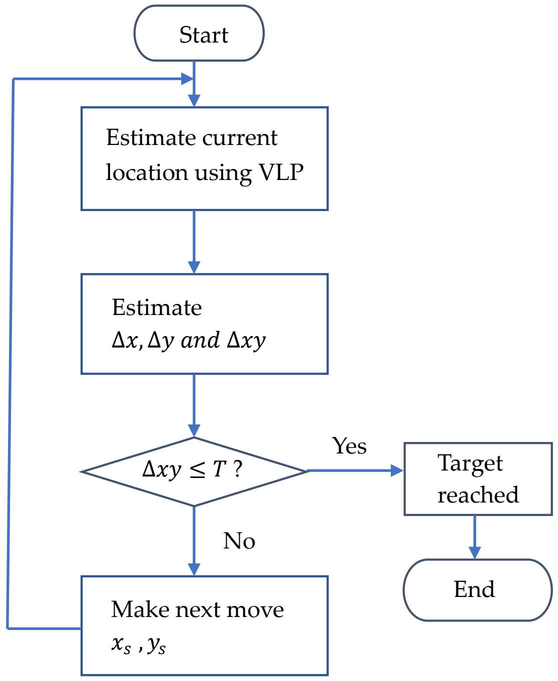

Fig. 4.7 Flowchart of Algorithm 1. Please see Figure 4.8 for details on Δx, Δy, and Δxy

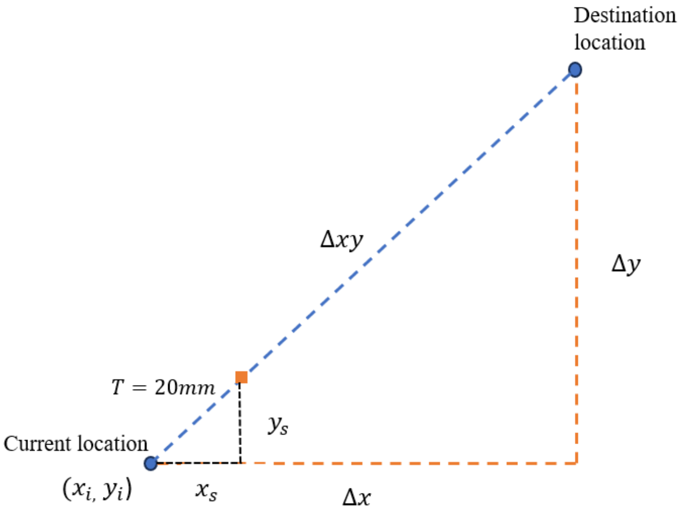

Fig. 4.8 Robot travels in a planned straight path from the current location to the destination location

4.5.2 Algorithm 2 (Spring Relaxation Method)

This algorithm is based on the spring relaxation [12] or artificial potential field [66] techniques. In this section, we explain the algorithm using the concept of spring relaxation which uses fictitious springs and Hooke's law to guide the robot to its destination/s. Figure 4.9 illustrates the concept of spring relaxation.

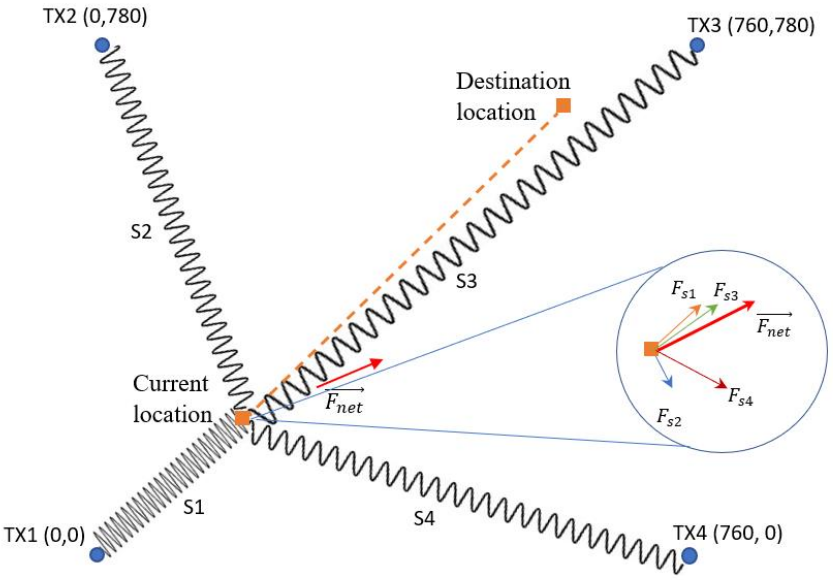

Fig. 4.9 Spring relaxation technique to guide CNC robot sensor to travel from current location to the destination location; it shows the various forces exerted by each spring, F_{s1} to F_{s4}, and the resultant net force, $\overrightarrow{F_{net}}$

The location of the luminaires is the anchor to which the one end of each fictitious spring is connected. The other ends are connected to the robot. The distance between the target destination and each anchor is the natural length of each corresponding spring. Therefore, when the robot is at its destination, all the springs are relaxed (neither compressed nor stretched) and no force is acting on any of them. The goal of the algorithm is to move the robot to a position where the net force acting on the springs is zero (or below a certain threshold). Figure 4.10 shows the flowchart of the algorithm.

(i) Compute the natural length, $l_{n,i}$ ($i = 1$ to 4 for our experimental setup), of the four fictitious springs of the sensor device at the target position.

(ii) Take an RSS reading at the current position, x_i, y_i . Next, calculate the distance of the robot from each luminaire using the ranging process described in Section 4.4.2 Equations (4.5) and (4.6). Each of these distances represents the current length of each spring, l_i ($i = 1$ to 4 for the experimental setup).

(iii) If the current location is not the destination, the springs are not in an equilibrium state (either compressed or stretched). A compressed spring experiences a push away from the anchor, whereas a stretched spring experiences a pull toward the anchor. The individual force, F_i , exerted by each spring, is estimated as $F_i = |l_{n,i} - l_i| e^{j\theta_{li}}$, where $|l_n - l_i|$ is the magnitude of the force and θ_{li} is the direction of the corresponding force.

(iv) Compute the net force acting on the robot as $\overline{\boldsymbol{F_{net}}} = \sum F_i$. Note that $\overline{\boldsymbol{F_{net}}} = |\overline{\boldsymbol{F_{net}}}|e^{j\theta_{net}}$, where $|\overline{\boldsymbol{F_{net}}}|$ is the magnitude of the net force and θ_{net} is the direction of the net force. If the net force is smaller than or equal to a threshold ($|\overline{\boldsymbol{F_{net}}}| \leq TH$), the robot is at the target. If not (i.e., $|\overline{\boldsymbol{F_{net}}}| > TH$), the robot moves toward the direction of the net force at the step size *T*. Steps (i)–(iv) are repeated and the robot moves until it reaches the destination.

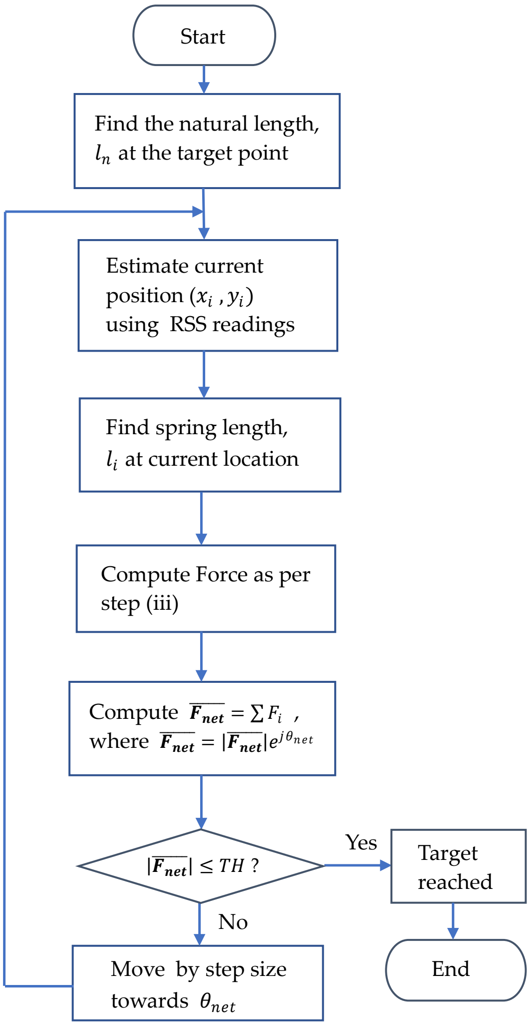

Fig. 4.10 Flow chart of Algorithm 2

Figure 4.11 shows the tasks completed by the PC to perform the navigation of the end-effector from the starting point to the next location.

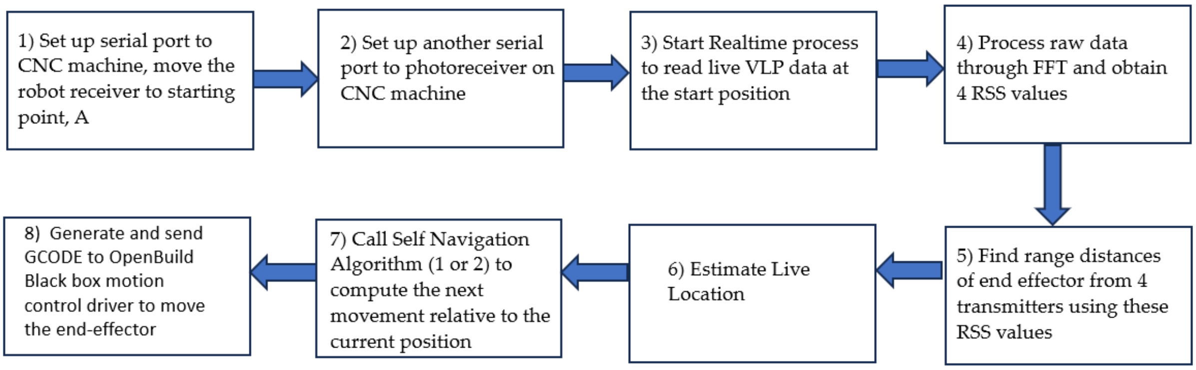

Fig. 4.11 The tasks completed by the PC to control the movement of the CNC end-effector while guided by one of the two algorithms running on live RSS data. Steps 3 to 8 are iterated until the end-effector reaches the destination (when the loop ends after step 6)

4.6 Experimental Results

Figures 4.12 - 4.14 show how the CNC end effector traverses through various paths. Each path is repeated five times. The actual location of the end effector can be determined to an accuracy of 0.1 mm since the CNC tracks and records its position. Please note that this information is only used as the ground truth and is not used to control the end effector which is solely driven by one of the algorithms based on the acquired RSS. As can be seen, VLP-driven algorithms can control the robot reasonably accurately. However, it is also clear that for all patterns, the robot does deviate from the ideal straight-line path. This is because the VLP-based position estimate using RSS data has some error. Due to this and the discrete nature of the robot's movement (step size of 20 mm), it does not reach the "target" points precisely. For every pattern, each path traversed is also slightly different regardless of the algorithm utilized. Therefore, the robot and the VLP-based control system, in its current state, does not have the precision or repeatability to be used for applications like assembly of electronic devices [67].

Figure 4.15 shows the cumulative distribution function (CDF) of the errors for each path. The error is computed as the amount of the deviation of the robot's locations from an ideal straight line. Figure 4.16 shows the CDF of the errors in reaching the target (measured as the difference between the destination point and where the robot stopped) for all the paths. The median and 90-percentile errors are shown in Table 4.2. It should be noted that the errors in reaching the target can be reduced by lowering the step size (e.g., 27.16 mm to 15.23 mm for algorithm 1 when the step size is changed from 20 mm to 5 mm). But that comes at the cost of higher computational cost and increased time.

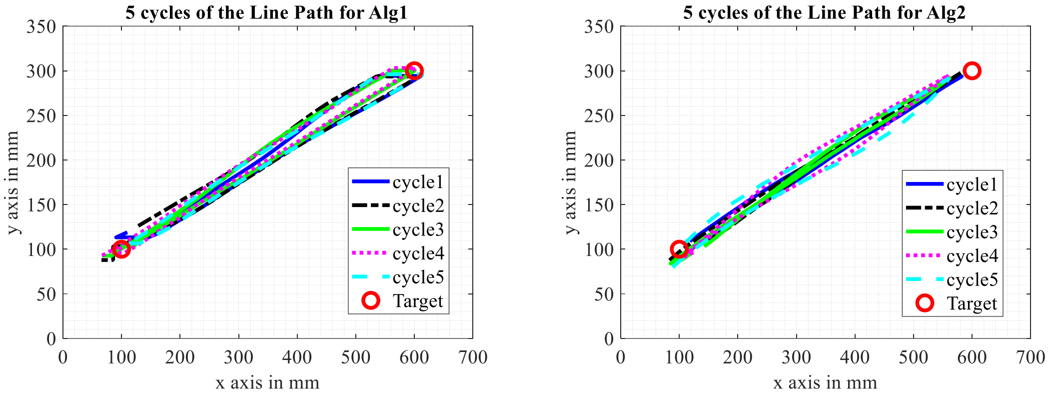

(**a**) (**b**)

Fig. 4.12 “Line Path” travelled by the robot. The robot is moving from point A (100, 100) to point B (600, 300) and then returning back to A. The diagrams ((a, b) for algorithms 1 and 2, respectively) show five iterations of the path

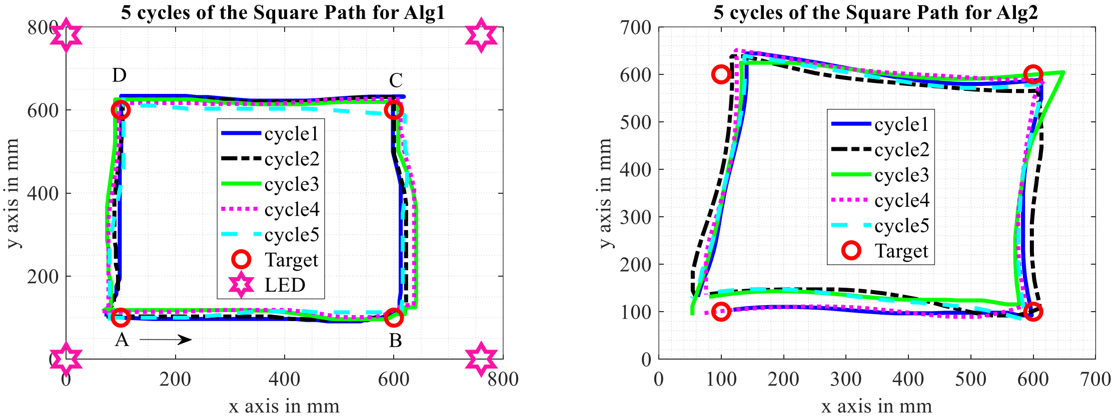

(**a**) (**b**)

Fig. 4.13 “Square Path” travelled by the robot. The robot is moving from point A (100, 100) to point B (600, 100) to point C (600, 600) to point D (100, 600) to point A. The diagrams ((a,b) for Algorithms 1 and 2, respectively) show five consecutive iterations of the path

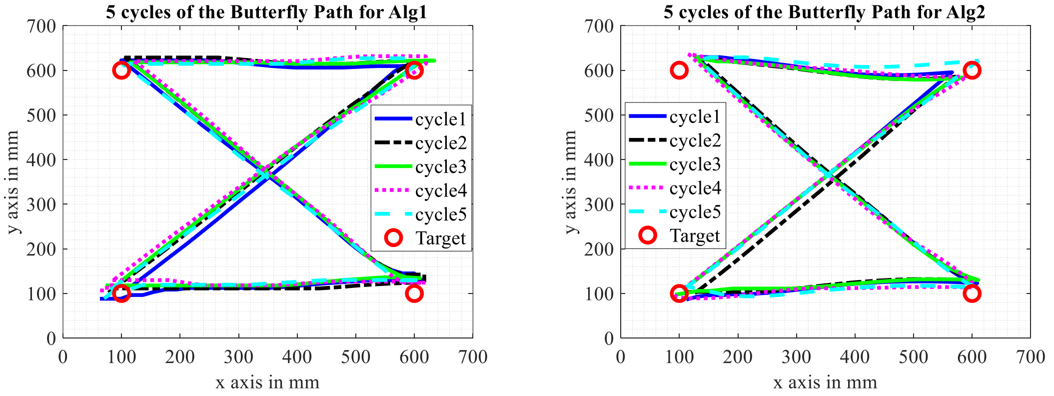

(**a**) (**b**)

Fig. 4.14 “Butterfly Path” travelled by the robot. The robot is moving from point A (100, 100) to point C (600, 600); then point C to point D (100, 600); then point D to B (600, 100) and then point B to A. The diagrams ((a,b) for Algorithms 1 and 2, respectively) show five iterations of the path

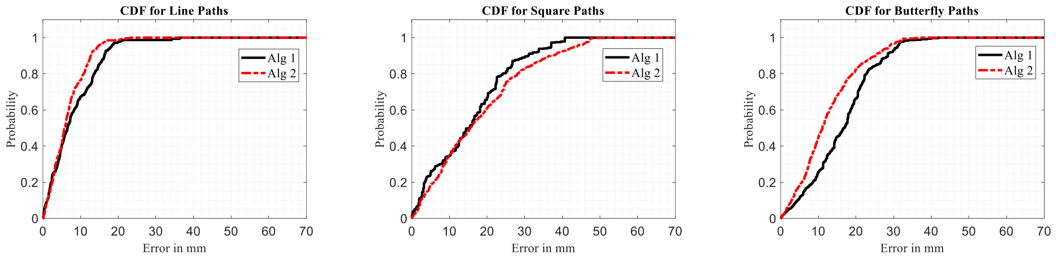

(a) (b) (c)

Fig. 4.15 CDF showing the accuracy of both algorithms for (a) Line Paths, (b) Square Paths, and (c) Butterfly Paths

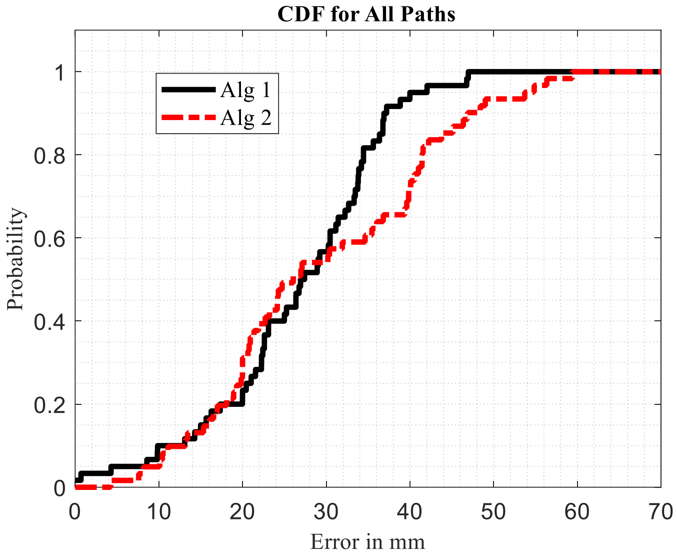

Fig. 4.16 Comparing "Target" positions accuracy

Table 4.2 Accuracy statistics for both algorithms for various scenarios

Scenario	Median Error (mm)		90-Percentile Error (mm)	
	Algorithm 1	Algorithm 2	Algorithm 1	Algorithm 2
Line Path	8.02	**5.86**	16.34	**12.71**
Square Path	**15.15**	15.51	**30.99**	37.59
Butterfly Path	16.81	**11.1**	28.48	**25.19**
Destination Points	27.16	**26.05**	**37.04**	47.48

4.7 Conclusions and Future Works

This work presented the control of a cartesian robot, a 2D CNC machine, capable of precise positioning along the X and Y axes using only a PD-based VLP system. Two algorithms were developed to control the position of the robot in real time. Both algorithms show promising accuracy. Algorithm 1 performed better for the "square path", achieving a 15.15 mm median localization error. Algorithm 2 performed better for the "line path" and the "butterfly path", achieving median localization errors of 5.86 mm and 11.1 mm, respectively. Given the accurate performance of the system, further investigation is warranted. Also, further investigation needs to be carried out before an algorithm can be conclusively recommended. There are several other limitations that can be addressed in the future.

The locations of the luminaires of the VLP have not been optimized. Future works can explore the optimization of the layout of the VLP system. However, it should be noted that as part of real-world implementation, the location of the luminaire may be dictated by the need for illumination.

The Lambertian model was simplified under the assumption that the PD and the luminaires are parallel. If the receiver tilts, the localization estimate is affected. However, there are models [68] that address this issue and can thus be adopted. A simple gimbal can also ensure that the receiver maintains its orientation.

Pose comprises of location and orientation. For this work, the location was determined via VLP. The orientation was determined via a CNC. Therefore, developing a new receiver capable of VLP-based orientation estimation will enable more sophisticated control strategies. Bernades et al. [69] proposed a multi-PD based system for estimating the orientation of the receiver for an infrared (IR)-based positioning system. A similar approach can be applied for estimating the complete pose (both location and orientation) of the receiver. Incorporating orientation information into the algorithm and conducting new benchmarking experiments will open new avenues for investigation. Obstacle avoidance and path planning can also be investigated in the future. But this will require utilizing other sensors alongside PD.

Chapter 5 - Ultrasound Indoor Localization Using Spring Relaxation Technique

In the earlier chapters, the research has been concentrating on the primary mode of localization which is based on Visible Light Communication. The problem exists when the positioning method relies only on one type of technology. In the event when there is sudden loss of sight due to malfunctioning of some LEDs or obstructions in the room, what alternative can be offered to compensate for the loss of position or direction of a mobile unit? There is a need to study other sensing which could help to compute the position of the mobile device/robot. This gives the motivation to the study on ultrasound for indoor localization, reportedly giving position accuracy which is on par with the Visible Light Positioning (VLP), in the order of centimetres [32, 70]. Ultrasound operates in the frequency range which is above the human hearing limit of 20KHz. For distance measurement, the frequency used is normally around 40KHz, and for medical usage the range is from 2.5MHz to 40MHz[71]. This chapter reports the development and experimental results on Ultrasound Indoor Localization (UIL) system based on Spring Relaxation (SR) technique. The UIL system uses 4 Ultrasound (US) transmitter modules which are mounted on the ceiling, and a receiver microphone acts as the target or mobile unit whose movement is controlled by the CNC machine that allows the unit to move within a 2-dimension XY frame test rig. The metallic XY frame has the size of 1.2m x 1.2m, and this is placed at 1.6m below the ceiling. The experimental results obtained from Spring Relaxation method are benchmarked against the linear least square based lateration technique. This system is also compared with VLP using the same platform set up. The obtained results show the UIL to be more accurate than the VLP in the same environment.

5.1 Time of Flight, TOF estimator

The principle of distance measurement using ultrasound is based on Time of Flight (TOF), the time taken by the ultrasound signal to reach the receiver sensor at the distance, d away

$$d = c \times TOF \qquad (5.1)$$

where c is the speed of sound. The relationship between ultrasonic velocity in the air medium and the environment temperature can be expressed as [72]

$$c \approx 20.06\sqrt{T+273.15}\,\left(\frac{m}{s}\right) \qquad (5.2)$$

Here T is the temperature in degrees Celsius. At 20 °C the speed of sound, $c \approx 343.5\,m/s$. There are a number of ways to measure TOF [73], but the two most common ones are threshold method and cross correlation method. Figure 5.1, adopted from [74], gives an example of how TOF estimation is obtained by the threshold technique.

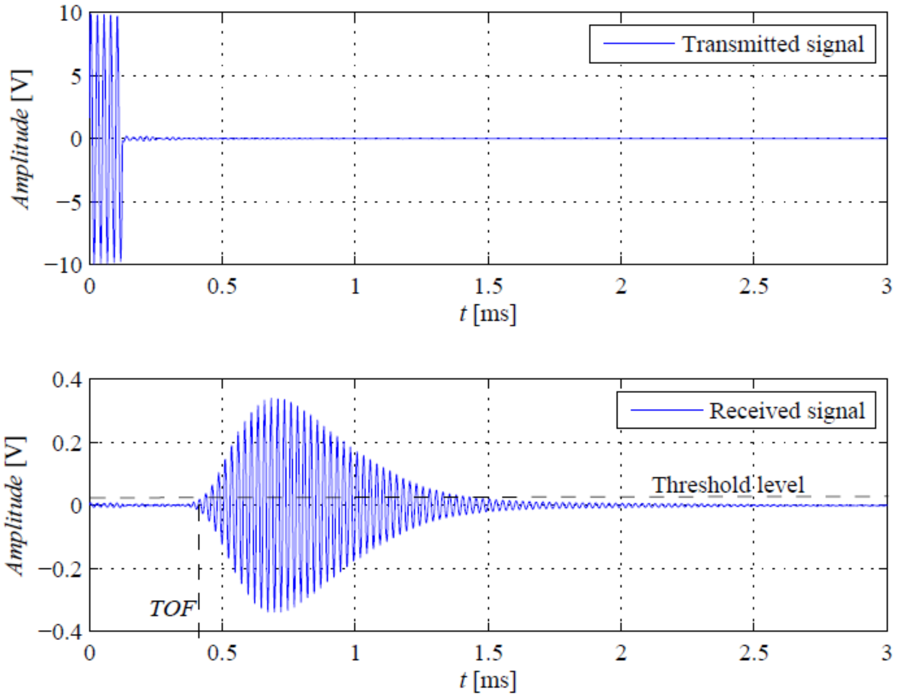

Fig. 5.1 TOF estimation by threshold method [74]

It shows that the TOF value is obtained as soon as the received signal crosses the threshold level, not long after the signal pulse is sent out. However, the main problem with this method is, that the measured TOF is normally larger than the actual TOF, thus making the target appear to be further than its actual distance. This is the result of the long rise time of the signal produced by the narrow bandwidth transducer at the reception side. The error could be corrected if the received signal is constant. However, in practice it is hard to achieve because of factors like signal-to-noise ratio (SNR), threshold level, and target location [73] which cause the amplitude fluctuation at the receiving end.

Another option is the use of cross-correlation technique between the transmitted signal and received signal. The TOF is measured at the time when the cross-correlation result reaches its peak. The technique works well with low SNR signals and it is less affected by low sampling rate problems [74]. Figure 5.2 shows an example of TOF obtained by cross-correlation.

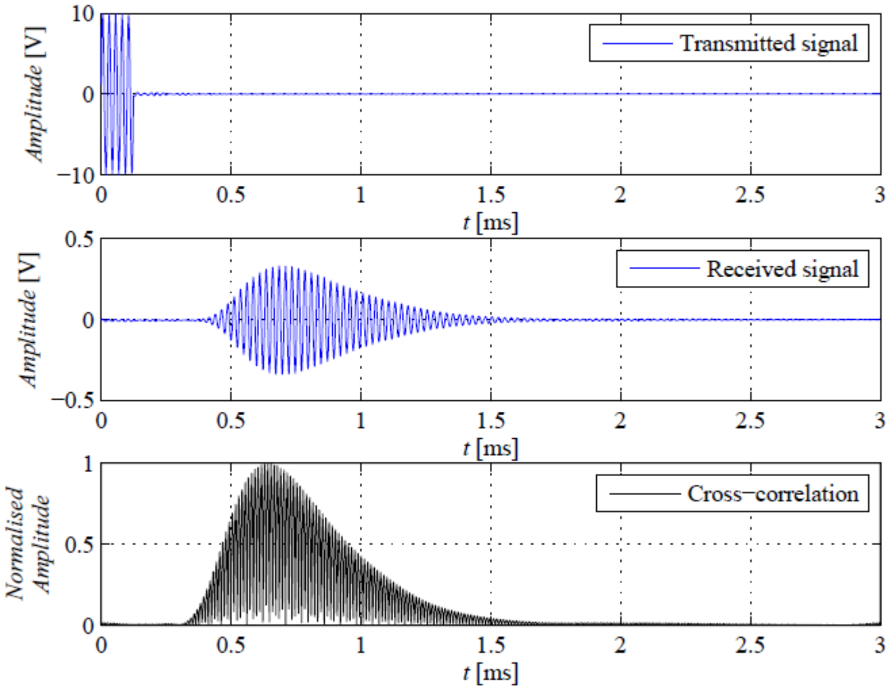

Fig. 5.2 TOF estimation by cross-correlation technique [74]

The cross correlation function of transmit signal *x(t)* and the received signal *y(t)* is [75]

$$R_{xy}\,(\tau) = \lim_{T\to\infty} \frac{1}{T}\int_0^T x(t)\,y(t+\tau)dt \qquad (5.3)$$

The peak value of cross correlation result is corresponding to τ which is the lag time between these two signals. Using equation (5.1), the target distance can thus be derived.

5.2 Review of past ultrasound indoor localization system

Most of the ultrasound positioning systems use Time of Flight (TOF) signal characteristic to measure the range distance between the transmitter and receiver. TOF is also referred as Time of Arrival (TOA). Other commonly used characteristics are Time Difference of Arrival

(TDOA) and Angle of Arrival (AOA). Once the range distance has been obtained, majority of researchers prefer to use lateration to compute the position of the target or mobile unit.

This section looks into various UIL systems reported in the literature. Various aspect of their US transmission/reception units have been studied, for example what type of US transmission signals have been applied - resonant frequency of 40KHz or some other signal characteristic such as chirp signal used for range measurement, localization algorithm, test bed size and position accuracy. The review only focuses on the practical and experimental type of UIL system rather than the simulation type of UIL. Table 5.1 gives the evaluation of those systems based on the above categorization.

Table 5.1 Evaluation on the past ultrasound indoor localization (UIL) systems

Ref	Spectrum	Range measurement	Localization algorithm	Methods	Position Accuracy Error
[76]	40KHz	TOF/TOA	Multilateration	-Object has array of 5 transmitters arranged in hemispherical pattern -16 receivers on the ceiling. - distance between 2 receivers is 1.2m -sub room scale	95-percentile 140mm
[77] Bat system	40KHz ultrasonic pulses of a 50-μs duration	TOF/TOA	Multilateration	-US transmission emitted from user's badge (Bat) -Central controller sends signal through wireless link to activate the badge to send US pulse to the receivers - 750 receivers on ceilings, wired in daisy chain network. Each receiver unit has a DSP microprocessor and matched-filter signal detection circuitry -50 badges given to employees. Each badge has unique 48-bit ID code - Office scale with 3 floors of 1,000 sq. m (consists of many sub sections)	95-percentile 30mm
[78] Cricket system	40KHz	TOF/TOA	Multilateration	-4 transmitters placed around 1.2m apart on the ceiling - target unit with 5 receivers arranged in "V" shape in few cm across -sub room scale	95-percentile 56mm - 250mm (at various target locations)
[79]	Chirp signal – range not mentioned	TDOA	Multilateration	-12 US transmitter beacons on various places on ceiling – Receiver on the target unit - Room area (5.2m x 3.6m)	200mm

[80] Dolphin system	50KHz (Dolphin)	TOF/TOA	Multilateration	-8 receivers on the ceiling about 0.5m -1m apart - one mobile target unit with transmitter placed at various test points -4 fixed transmitters at 0.75m above the floor to test multiple access potential of broadband system -sub room scale (3.5mx2.6m)	95-percentile 50mm
[81]	40KHz	TOF	Trilateration	-7 US receivers on ceiling -mobile transmitter tag is placed 2.6m above ground -Room area (5mx3m)	90-percentile <150mm
[82]	45KHz	AOA and TOF	Trilateration	– 3 transmitter beacons on the ceiling corners -a mobile unit with 3 receivers arranged in triangle (placed 2cm apart) -Sub room scale (3.5mx2.85m)	99-percentile 95mm
[83]	19KHz to 23KHz	TDOA	Multilateration	-The transmitters are sending each of their ID code sound clip through the public PA system -Receivers are mobile phones and tablets -Atrium	95-percentile <100mm
[84]	21.5KHz from mobile phone	TDOA	Asynchronous Trilateration	- 4 microphones placed just below ceiling -mobile phone (target unit) transmit the US, placed 1.6m below ceiling - Room area (7mx7m)	Mean of 100mm
[85]	18KHz-22KHz chirp signal	TOF	Geometrical method	-Localization of a person in static position and moving position. Based on first reflection from the human body in the line of sight and the second reflections from the 2 reference walls (together with unscented Kalman filtering) -Sub room scale	static position , median error =150mm and moving position, median error = 80mm
[86]	Not mentioned, presume 40KHz	TDOA	Trilateration	-5 receivers on ceilings -1 transmitter on mobile unit - Sub room scale(2mx2mx2m)	Approx. mean = 50mm
[87]	40KHz (6 transmitters on ceiling)	TOF/TOA	Multilateration	-6 transmitter on ceilings -1 mobile receiver unit -Sub room scale(2.4mx0.9 m)	Approx. mean = 160mm

[88]	Chirp signals – range not mentioned	TOF	Trilateration with inertial sensor data,	-Anchor receivers are connected using RS485 bus. - KUKA mobile robot equipped with transmitter moving in reference path - Sub room scale.	mean deviation = 24.4mm, and maximum deviation = 68.7mm
[89]	PWM of 40KHz	TDOA	Multilateration, Linear Least Square (LLS)and Nonlinear Least Square (NLS) techniques	-5 receivers on ceilings connected using CAN network -1 transmitter on mobile unit - Sub room scale (2.5mx2.5mx2.5m	Result applicable to test points that are under 45 degree angle of arrival. 90-percentile: 23mm for LLS and 21mm for NLS
[90]	Not stated	TOF	Multilateration	-4 receivers with fixed positions, each one is placed at 1.5m height on the standing pole -1 transmitter on mobile robot moving in slow speed within circle track of radii of 0.5m	Maximum location error is 10.2mm
[91]	BPSK modulation (63-bit Kasami sequences) with two periods of a sinusoidal carrier at 41.67 kHz	TDOA	Multilateration	-5 US transducer beacons on the ceiling, emitting 5 different sequence codes which are binary phase shift keying modulated and 1 TOF camera on the floor to measure height of drone -1 drone with receiver -Sub room scale	Mean error 176mm

From Table 5.1, it shows the position accuracy of the various UIL systems vary from 50mm to over 100mm for 95 percentile, with the exception of Bat system [77] which gives 30mm. The latter system has a sophisticated and extensive infrastructure. There are altogether 750 receiver units and each has a DSP microprocessor and matched-filter signal detection circuitry. Accordingly, the papers also quoted sources of errors from these positioning systems, for example in [78] the inaccuracy is due to US reflection from the nearby wall or multipath propagation effect. The noisy receiver is one factor to be looked into from [80]. Hardware limitation is another contributor of uncertainty error as suggested by [88], for example using infrared synchronization method can cause approximately 0.6mm uncertainty in the ultrasound based distance measurement, in addition, the measurement update rate can be affected by the communication speed over the RS485 bus.

5.3 Ultrasound Hardware: Transmitter and Receiver

The US transmitter and receiver used in the localization experiment are MA40H1S-R surface mount transducer/transmitter and microphone receiver WM61A respectively- Figure 5.3

Fig.5.3 (a) MA40H1S-R transmitter

Fig.5.3 (b) WM61 condenser microphone receiver - both sides

The actual transmitter/transducer circuit board is made out of a cluster of 8 MA40H1S-R, connected in parallel and soldered closely to each other as in Figure 5.4. The US receiver system has a WM61A microphone, with an inbuilt high pass filter and pre-amplifier circuit encapsulated in one casing. Figure 5.5 shows the US receiver system.

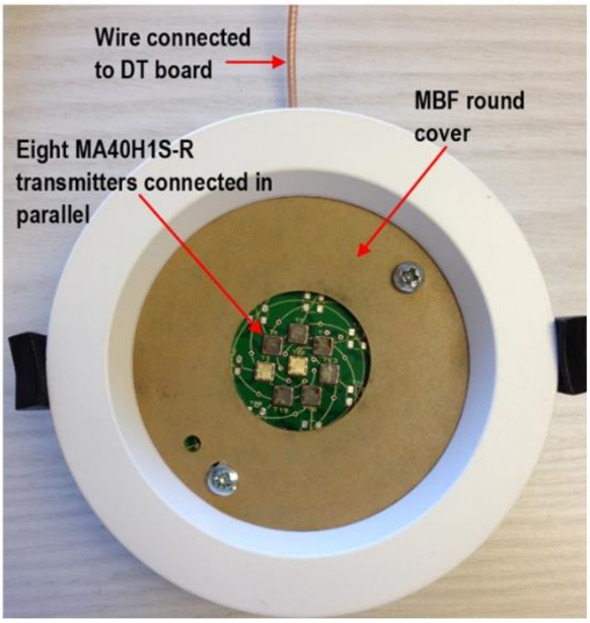

Fig. 5.4 Actual transducer board

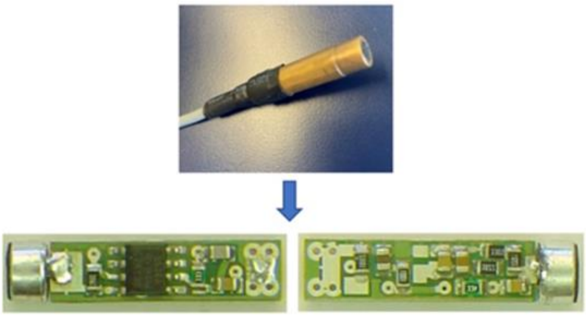

Fig. 5.5 US receiver system - consists of WM61A, high pass filter and pre-amplifier

The ultrasound signal is captured through the WM61A microphone and a high pass filter cuts off signals below 10 KHz. The signal is then amplified through pre-amp circuit, so that it can be processed by analogue to digital converter (ADC). The digital data is saved in the database for the use of localization analysis later on. An overview of the receiver set is depicted in Figure 5.6(a) block diagram and Figure 5.6(b) shows its schematic circuit.

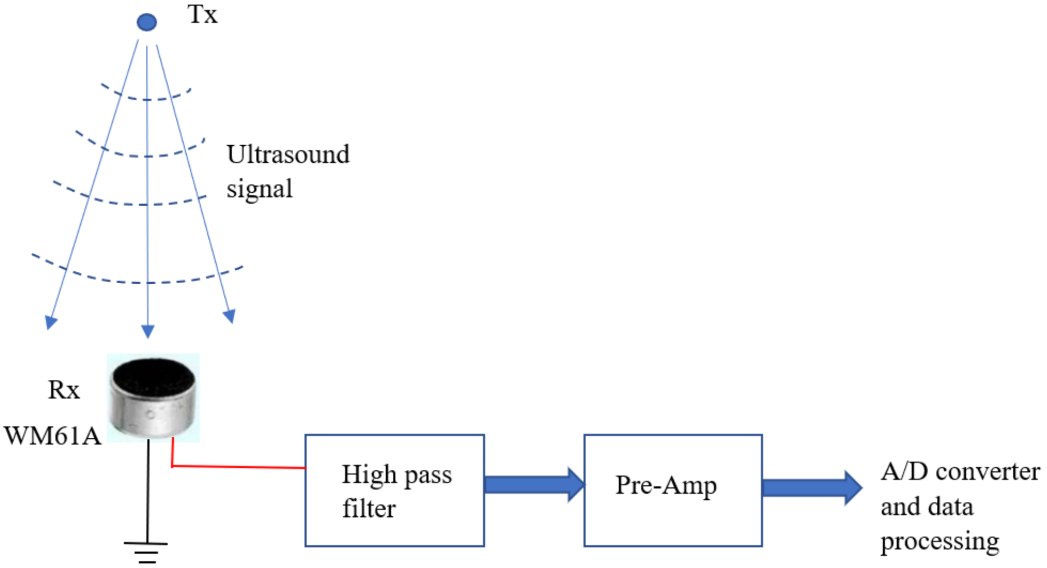

Fig. 5.6(a) Block diagram of receiver system

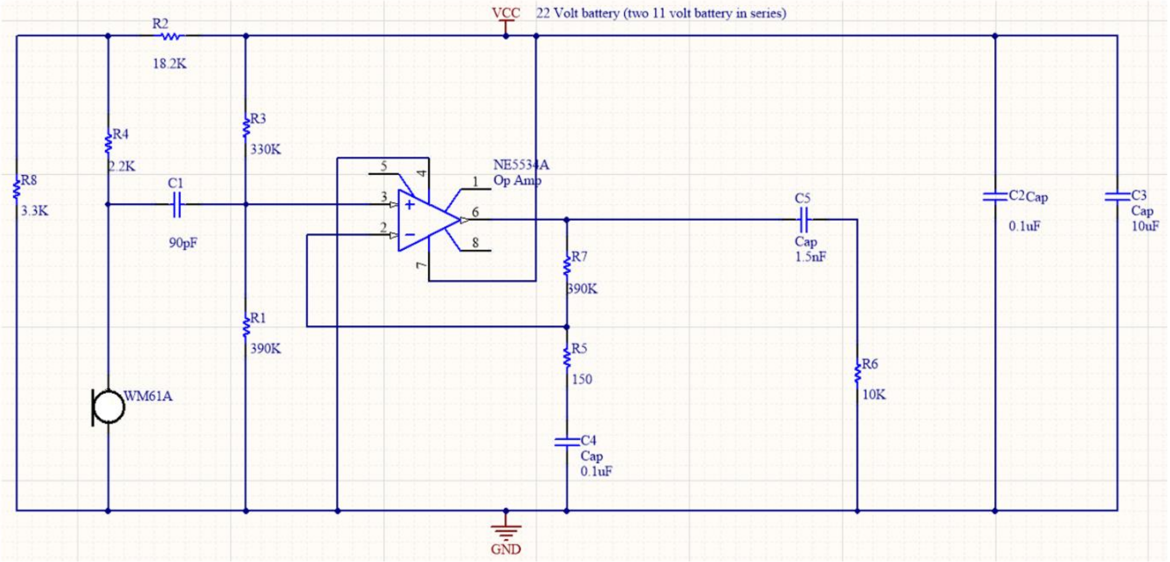

Fig.5.6(b) Schematic circuit of receiver system

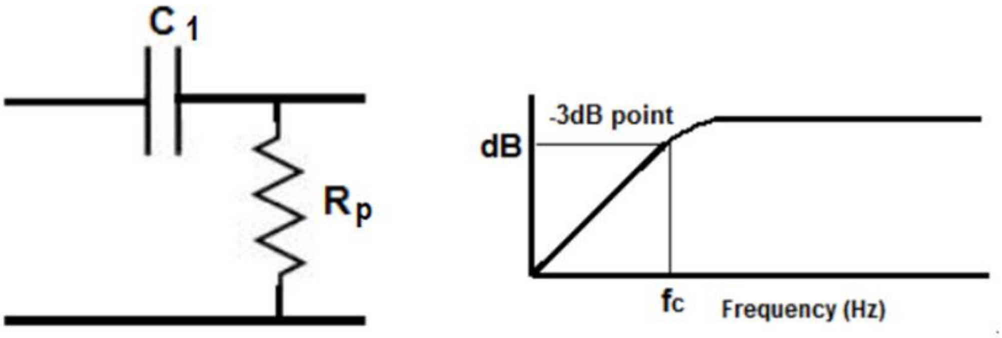

Fig.5.7 High pass filter and its frequency response

The AC circuit analysis of Figure 5.6(b) shows that C1 and Rp (the equivalent resistance of R3 in parallel with R1) effectively form the high pass filter with the approximate cut-off frequency, f_c of 10 KHz as shown in Figure 5.7

$$R_P = \frac{R_3R_1}{R_3+R_1} = \frac{330\times10^3\times390\times10^3}{330\times10^3+390\times10^3} = \frac{128700\times10^6}{720\times10^3} = 178.75\,K\ ohm$$

$$f_{c=}\ \frac{1}{2\pi C_1R_P} = \frac{1}{2\pi\times90\times10^{-12}\times178.75\times10^3} = 9.893\times10^{-6}\times10^9 = 9.893\,KHz$$

Therefore, $f_c\ \cong 10\,KHz$

Because the signal received is rather small, a high gain amplifier is needed to boost the signal in this case, this gives:

Gain of the Pre-Amp = $\frac{R_7}{R_5} = \frac{390\times10^3}{150} = 2600$

This circuit is intentionally designed with no high frequency cut off so that ultrasound signal in the range between 20 KHz to 40 KHz can be captured.

5.3.1 DT9836 Data Translator (DT) board

Another important piece of hardware equipment in the US localization experiment is the DT9836 Data Translator board. The DT9836 Series provides USB 2.0 multifunction data acquisition (DAQ) modules. All functions of the DAQ (A/D, D/A, DIO, counter/timers, and quadrature encoders) can be simultaneously triggered internally or externally [92]. The DT9836 Board and its various DAQ module outputs can be seen in Figure 5.8(a) and its key features are given in Figure 5.8(b). The data translator board, DT9836 is essential in synchronizing the transmitter and receiver operation, which is necessary for estimating the TOF.

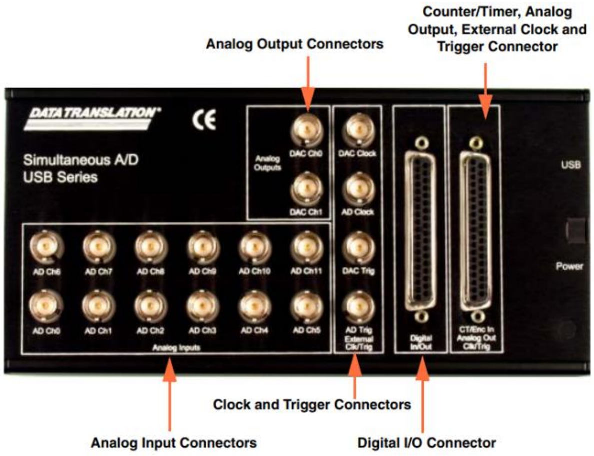

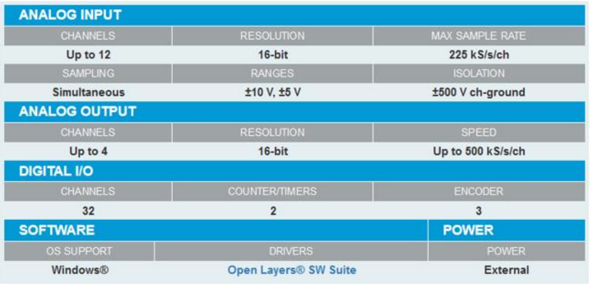

ANALOG INPUT		
CHANNELS	RESOLUTION	MAX SAMPLE RATE
Up to 12	16-bit	225 kS/s/ch
SAMPLING	RANGES	ISOLATION
Simultaneous	±10 V, ±5 V	±500 V ch-ground
ANALOG OUTPUT		
CHANNELS	RESOLUTION	SPEED
Up to 4	16-bit	Up to 500 kS/s/ch
DIGITAL I/O		
CHANNELS	COUNTER/TIMERS	ENCODER
32	2	3
SOFTWARE		**POWER**
OS SUPPORT	DRIVERS	POWER
Windows®	Open Layers® SW Suite	External

Fig.5.8 (a)
DT9836 board with BNC connectors[92]

Fig. 5.8 (b)
Key features of DT9836 board [92]

Besides, the DT9836 series module also supports MATLAB software suite which gives an added advantage as the result interpretation can be visualized in graphics. The DT board becomes the main driver for both US transmitter/transducer and US receiver. A broad view of connection between DT board, transducer and received is illustrated in Figure 5.9(a).

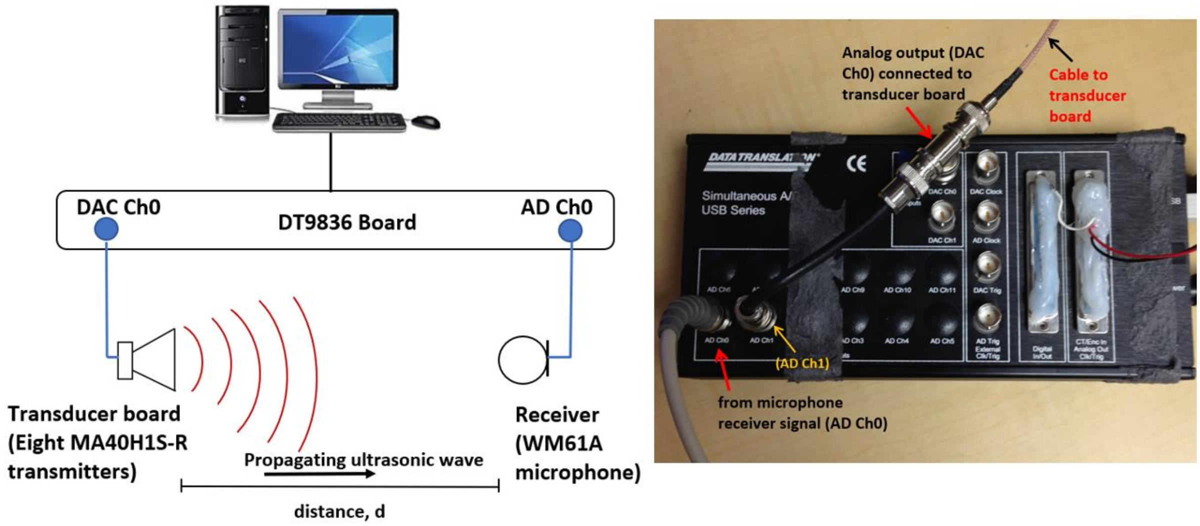

(a) (b)

Fig.5.9(a) A broad view of interconnection between DT9836 board, the transducer and the receiver
Fig.5.9(b) Hardware connection of transducer and receiver to DT board

The transmitter/transducer signal was digitally generated using MATLAB script and its conversion to analog output is produced by the DAC module of the DT board. The analog signal taken out from the DAC Ch0 shown in Figure 5.9(b), is responsible for driving the cluster of MA40H1S-R chips which form the transducer board in Figure 5.4. In addition, the connections made on the DT board allows for simultaneous capture of both the transmitting and receiving signal, so that these can be displayed on MATLAB screen. This is achieved by analog to digital conversion of transmitting signal via input AD Ch1. In the meantime, the receiving signal from the microphone and pre-amp circuit is captured by ADC channel, AD Ch0 of the DT board.

5.3.2 Chirp signal

Generally, there are a few types of signals which are commonly used for ultrasound transmission, these are chirp signal, tone signal and hamming window signal as shown in Figure 5.10. The chirp signal is widely used in radar applications due to its Pulse Compression characteristic [83, 93, 94]. It has range enhancement capability and a good level of noise immunity, thus leading to good SNR performance. Effectively, it increases ranging resolution as well as receiver sensitivity [83]. This experiment adopts the chirp signal over the other two for the indoor ultrasound localization system due to such advantageous characteristics.

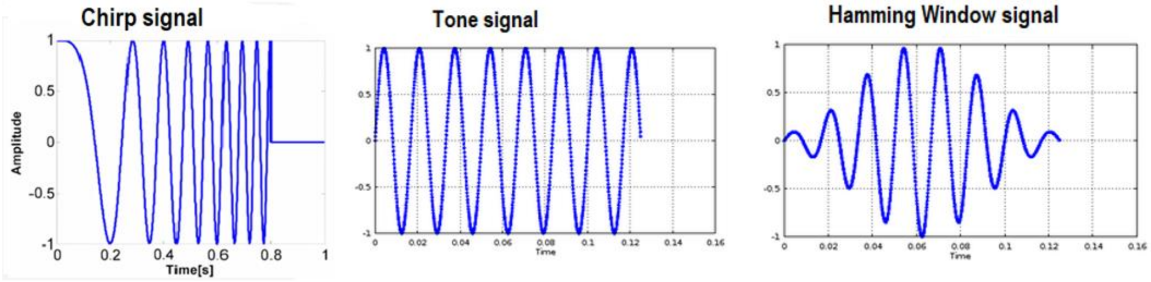

Fig. 5.10 Different types of signals for ultrasound transmission

The specified frequencies for the linear up chirp signal in the experiment is from frequency $f_0 = 20KHz$ to $f_1 = 35KHz$. The signal can be defined as:

$$R(t_m) = \cos\left(2\pi f_0\, t_m + \frac{\mu {t_m}^2}{2}\right), \qquad 0 \le t_m \le T_w \qquad (5.4)$$

where chirp sweep rate, $\mu = \frac{2\,\pi\,(f_1 - f_0)}{T_w}$ and T_w= transmission time taken to sweep from f_0 to f_1, and t_m is m^th^ transmit sample time

The transmission time, T_w for the signal is 1ms. At the receiver side, the sampling frequency is set to 500KHz at the ADC input. For the recording period of 40ms, there will be 20,000 samples taken. Figure 5.11 shows the transmitted and received signals averaging out of the 5 readings taken at one position.

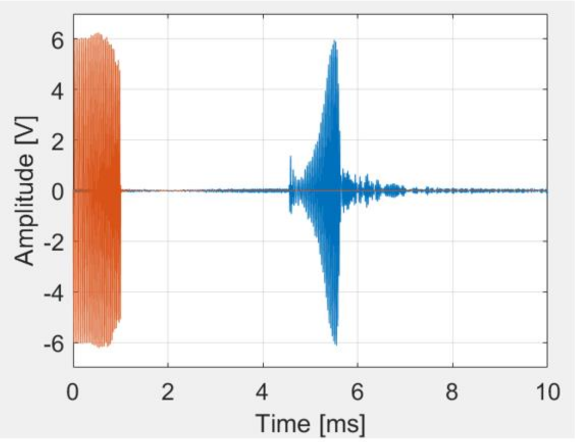

Fig.5.11(a) Transmitter(red) and receiver(blue) signals

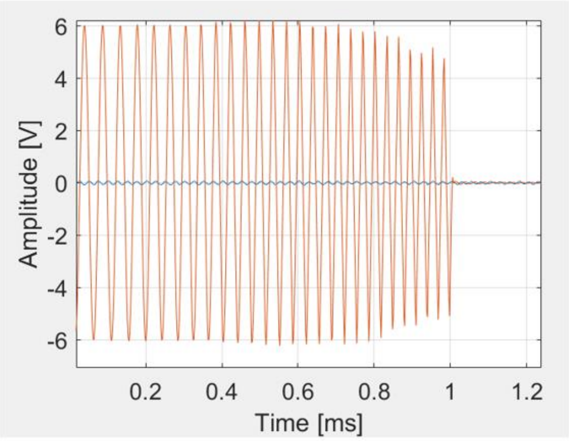

Fig.5.11(b) Expanding the transmitter chirp signal-frequencies ranging from 20KHz to 35KHz

5.4 Implementation of Ultrasound Indoor Localization System

The Ultrasound Indoor Localization (UIL) prototype system consists of four ultrasound (US) transducer/transmitter boards as described, and these are placed on the ceiling. The target object consisting of WM61A microphone receiver unit was mounted 1.6 m below a computer numerical controlled (CNC) machine with a dimension of 1.2 x 1.2 m. The CNC machine has an accuracy of 0.025 mm, of which the magnitude is better than the expected localization accuracy of the UIL system. The receiver unit, mounted onto the CNC machine, can be moved to various test locations with a very high accuracy. This ensures that the ground truth is accurately recorded. Figure 5.12 illustrates the UIL system test rig set up that was used.

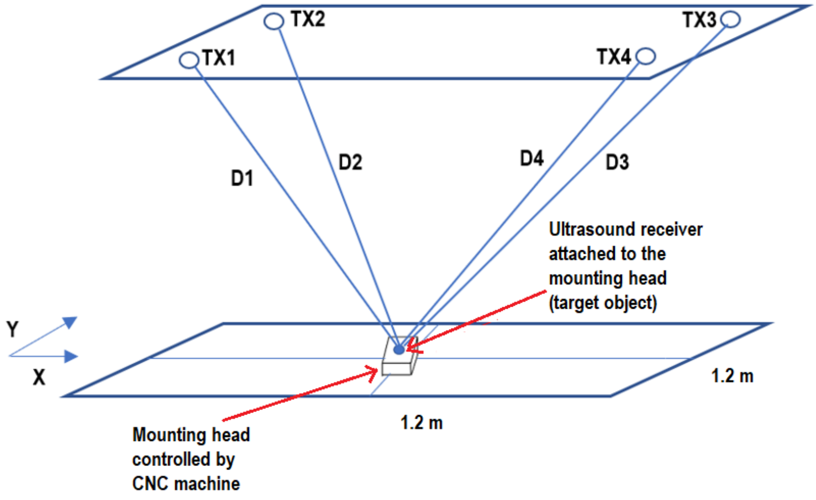

Fig. 5.12 (a) The UIL system set up

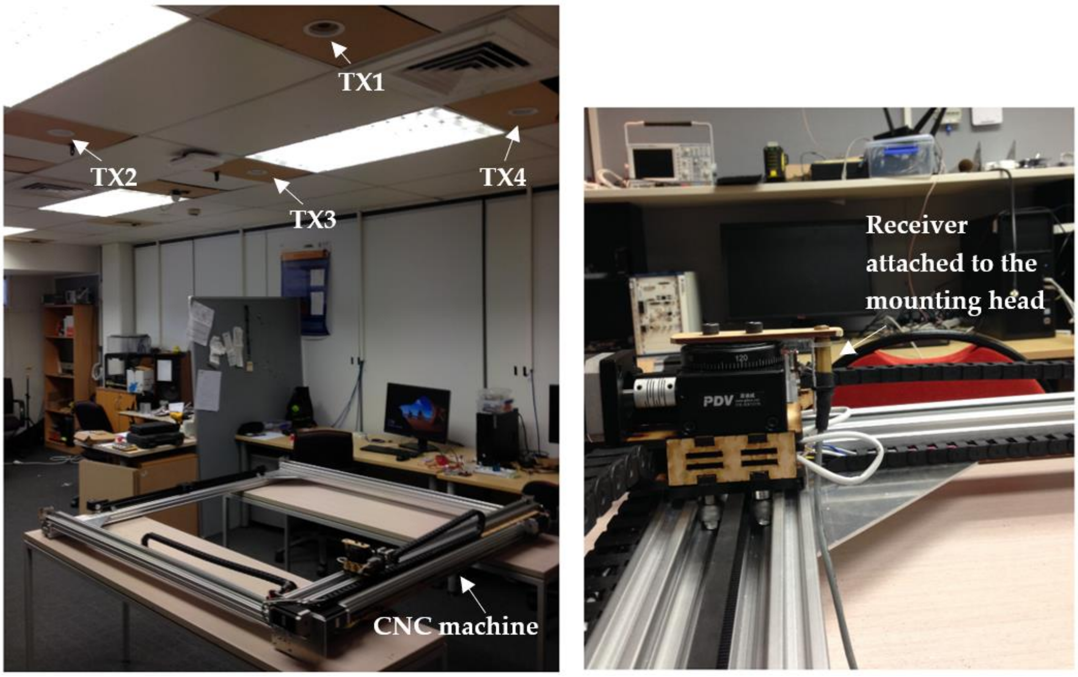

Fig.5.12 (b)

Fig.5.12 (c)

Fig. 5.12 (b)The actual UIL test rig with CNC machine Fig.5.12 (c) A closeup view of the receiver microphone on the CNC

5.4.1 Data Collection

The four anchor transmitter stations TX1 to TX4, shown in Figure 5.12(b), send out their ultrasound waves to the target object. The transmit and receive hardware is synchronized through the DT board - as described in Section 5.3.1. In a real-world implementation, an RF or infrared signal can be used to trigger the synchronization between the US emitter and receiver

[95]. A time division multiple access (TDMA) [96, 97] scheme can be deployed to multiplex the ultrasound emission between these anchor/emitter nodes. At any test point, there will be four different range values (computed using TOF), e.g. D1, D2, D3 and D4 obtained at one location, see Figure 5.12(a). Figure 5.13 shows how the CNC machine was used to obtain measurements with the target object (microphone in this case) at a range of positions in a grid pattern starting from coordinate (0mm,0mm) to coordinate (1200mm, 1200mm) with 50mm step increments between measurement locations. Altogether 625 positions are to be recorded, and 5 readings are taken at each point (later each position will be average out of these 5 readings). The total number of recorded received signals in this case, for example, from TX1 is 625 x 5 = 3125, and the same numbers are recorded for TX2, TX3 and TX4.

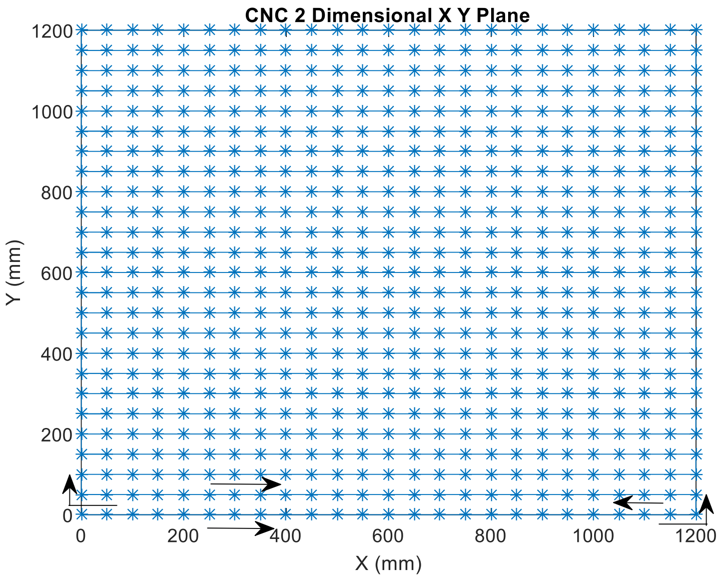

Fig.5.13 Traverse path of the target object equipped with microphone receiver in the CNC's 2 dimensional XY plane. The asterisks show the test points where the data was recorded

The next step is to get the TOF values from the previously stored raw data of four transmitters and then converted to ranges (D1-D4) to be kept in the database for the usage in the localization algorithms. The ambient temperature impacts the speed of sound in the air, ultimately affecting the range estimation. Therefore, the room temperature was recorded during the experiments. For a real-world system, a temperature sensor of high accuracy and low power consumption (e.g. TMP117[2]) can be collocated with the receiver tag.

---

[2] https://www.ti.com/product/TMP117

5.4.2 Estimating Time of Flight Using Cross-Correlation

This experiment uses the cross-correlation technique to measure the TOF. The discrete time cross-correlation function of transmit signal $x[m]$ with the received signal $y[m]$ can be defined mathematically as [75]:

$$R_{xy}\,[k] = \sum_{m=0}^{M-1} x[m]\, y[m-k]. \tag{5.5}$$

where m is the sample index, M is the total number of samples, and k is the number of samples that the data is shifted. This shift can be related to a time shift τ using $k = \tau\, F_s$, where F_s is the sampling rate. The time shift when the cross correlation reaches its maximum value is taken as the estimate of the TOF. This technique works best where excitation waveforms are used for transmission that have good autocorrelation properties such as chirps.

Figure 5.14 shows a sample of a raw signal measured at a target's position, n=72 and the cross-correlation of this signal with the transmit signal. Here there are multiple peaks in the signal. The first peak is the direct path signal which is the one that is used for TOF measurements. The other peaks are due to multipath signals resulting from echoes from walls, the floor and any surrounding artifacts. A threshold method can be used to select the direct arrival signal for TOF measurements and avoiding the secondary peaks that resulted from multipath echoes.

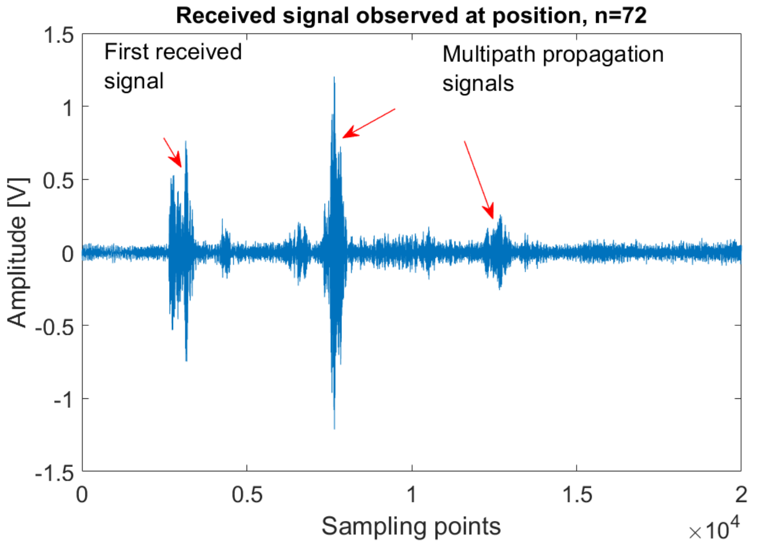

(a)

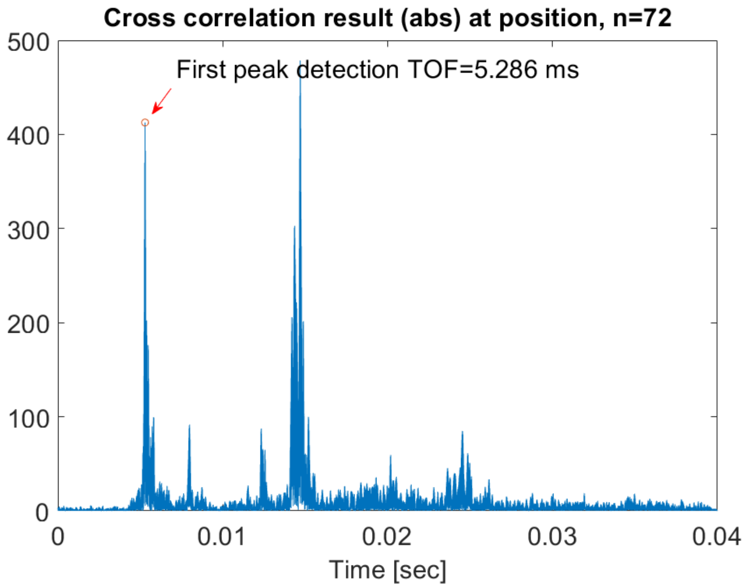

(b)

Fig. 5.14 An example of the receiver's signal taken at one of the target's positions is plotted in (**a**). The corresponding cross-correlation signal is shown in (**b**). Multipath signals can be seen

5.5 Spring Relaxation Localization Algorithm

The concept of Spring Relaxation (SR) technique in the application of location estimate can simply be explained with finding the net force [98] of a set of fictitious springs [12] connecting to the target unit whose position is to be determined. Figure 5.15 shows that 4 separate springs where each end is attached to its corresponding anchor node or transmitter node. These anchor nodes are at the fixed and known positions, whereas the other end of each spring is attached to a moving target (with receiver sensor). Each spring has a natural length when the net force experienced by the target is zero. Normally the target receives a zero net force whenever the springs are at their relax positions. The spring's natural length is found through the range measurement using TOF.

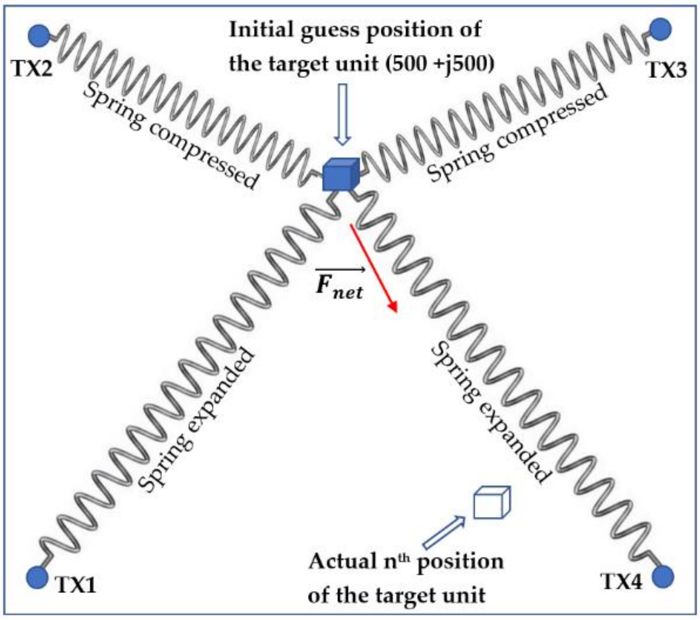

Fig.5.15 Application of Spring Relaxation technique for location estimation

Now assume the target unit is at the initial guess position as illustrated in Figure 5.15, and the target's final position at the nth position (the actual location of the target) is to be estimated. Each spring's length, l will be computed by taking the difference between the current estimate position and its corresponding anchor's position. According to Hooke's law, the force exerted on each spring is described as $F = K(l - l_0)$, where l is the current length of the spring , l_0 of the natural length of the spring and K is the spring constant (assume K =1 in this case). Each spring will either be compressed or expanded according the difference $(l - l_0)$ that gives a positive or negative vector force, $\vec{F}$ that exerted on the target object. At each iteration of SR algorithm, the net force which is the vector sum of the individual force, $\overrightarrow{F_{net}} = \sum_{i=1}^{N} \vec{F_i}$ (where N = total number of fixed transmitters) will move the target for a small distance in the direction of the net force. The net force is non zero to start with at the initial guess position. The total net force reduces each time the target moves toward the final destination. The SR iteration algorithm stops when the net force received by the target unit reaches zero or a pre-defined threshold value, eg. 10^{-4} Nm.

According to [12], the location of i^{th} transmitter or anchor node is given as a cartesian complex number:

$$X_i = x_i + j\, y_i \,, \tag{5.6}$$

where i=1 to 4 (TX1 to TX4 in this case) and the imaginary number, $j = \sqrt{-1}$, is used here to represent the y-axis direction.

The current estimate coordinate of the target is given as:

$$X_{est} = x_{est} + j\, y_{est} \qquad (5.7)$$

The current length of each spring is :

$$l_i = X_{est} - X_i \qquad (5.8)$$

The individual force exerted on the target by the *i*th spring can be represented by the exponential and polar formats as follows

$$F(i) = \left| r_{i,n} - l_i \right| e^{j\theta_{li}} = \left| r_{i,n} - l_i \right| angle\ (\theta_{li}), \qquad (5.9)$$

where $r_{i,n}$ is the horizontal distance range measurement (natural length) at the target's *n*th position and *i* = 1 to 4 (i.e. the spring number)
The net force exerted on the target will be:

$$\overrightarrow{\boldsymbol{F}_{net}} = \sum_{i=1}^{4} F(i) \qquad (5.10)$$

At each iteration of SR algorithm, the target will move a small step size from its current position towards the direction of the net force, $\overrightarrow{F_{net}}$. Hence the target's new current estimate position is:

$$X_{est}^{m+1} = X_{est}^{m} + \Delta F_{net}^{m}, \qquad (5.11)$$

where *m* is the iteration number and Δ is the applied step size.

From here, the SR algorithm will update l_i (equation 5.8) based on the new estimate of the current coordinate, and re-calculate the individual force and the total net force on the target.

The algorithm repeats the whole process and updates the location estimate, and it will stop processing when the net force reaches a pre-defined threshold value, σ :

$$F_{net}^{m} < \sigma, \qquad (5.12)$$

where σ can be set at 10^{-4} or lower for example

5.6 Ultrasound Localization Results

As per the discussion in Chapter 2, the accuracy of a localization system is evaluated through measuring the localization error which the Euclidean distance between the ground truth and the estimated position of the target. Statistical measures like the CDF, mean, median and percentile values of the localization error are used to investigate the localization accuracy.

5.6.1 Spring-Relaxation Results

A value of 625 positions (see Figure 5.13) were tested. For this testbed, the larger ranging errors appear in the regions that are closer to the transmitters, as shown in Figure 5.16. This was believed to be due to echoes being picked up by the microphone when the receiver was located under one of the transmitters. These multipath components were not resolved, leading to error in TOF measurements.

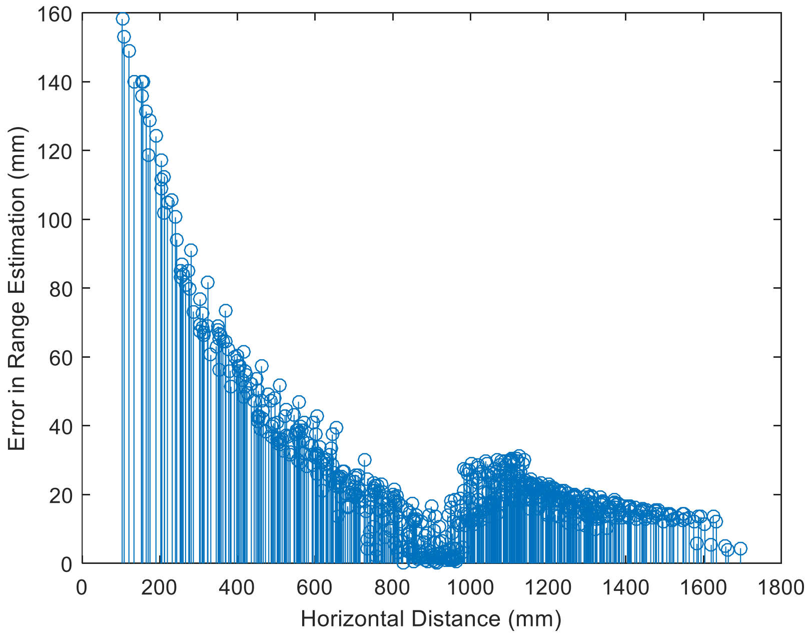

Fig. 5.16 Measured ranging errors as a function of horizontal distance from the transmitter. Larger ranging errors occur when the receiver is near the transmitter

This range-dependent error leads to modification of Equation (5.9) by applying weightings while calculating the forces acting on the springs giving:

$$F(i) = w(i)\,|\,r_i - l_i|\; angle\,(\theta_{li}) \tag{5.13}$$

The weights are estimated as:

$$w(i) = \frac{r_i}{\sum_{i=1}^{4} r_i} \tag{5.14}$$

The weighting *w(i)* is analogous to the spring constant, with larger springs, representing larger Tx-Rx (Transmitter to Receiver) separation, considered stiffer. Thus, the larger the spring, the more the contribution it has to the net force, since the ranging is more accurate for larger Tx-Rx separations. While the concept of variable stiffness has been utilized to account for the measurement uncertainty in wireless sensor networks [99], it has not been applied for the mitigation of US ranging error.

As a result of applying variable spring stiffness (Equation 5.13), the localization performance was seen to improve as demonstrated by the CDF (cumulative distribution function) plot shown in Figure 5.17. It shows the probability that an error of a particular size will occur. For example, it can be seen that with identical spring stiffness, 90 percent of the errors are less than 33.8 mm. The mean error reduced from 17.6 to 13.0 mm when using the weighting method. Table 5.2 summarizes the results of the SR algorithm for the two cases.

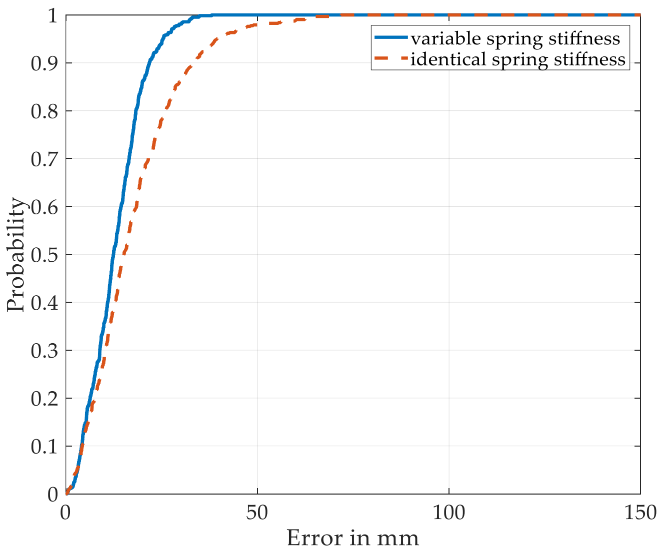

Fig. 5.17 Cumulative distribution function, CDF, of spring- relaxation localization error. The red line corresponds to no weighting (uniform springs) being used. The blue line corresponds to weighting (variable stiffness springs) being used

Table 5.2. Localization accuracy of the proposed spring-relaxation algorithm

With Identical Spring Stiffness (no Weighting)	**With Variable Spring Stiffness (with Weighting)**
Median = 15.2 mm Mean error = 17.6 mm 90-percentile = 33.8 mm Std-deviation = 12 mm	Median = 12.4 mm Mean error = 13.0 mm 90-percentile = 21.8 mm Std-deviation = 6.9 mm

5.6.2 Benchmarking Spring- Relaxation (SR) with Linear Least Square (LLS)-Based Lateration

The ultrasound indoor localization (UIL) accuracy error obtained from both the methods of LLS lateration and SR are shown in Figure 5.18 and Table 5.3. As can be observed, the SR algorithm outperforms the lateration in terms of accuracy.

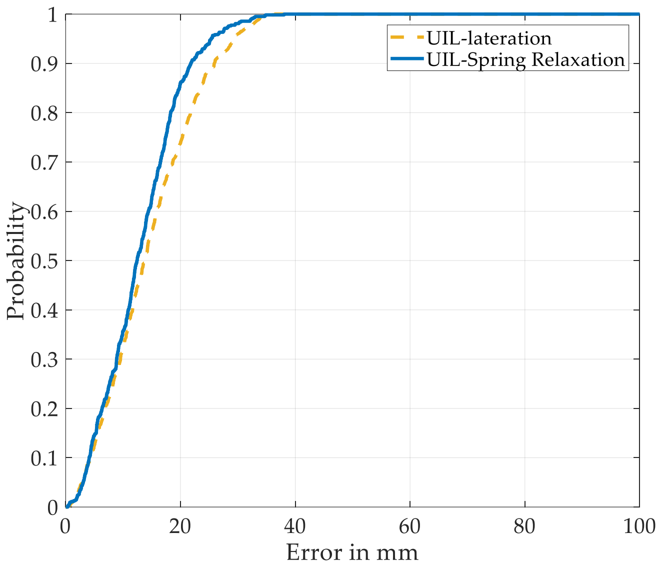

Fig. 5.18 UIL localization accuracy error for spring- relaxation and LLS lateration. LLS: linear least square

Table 5.3 Localization accuracy error of the spring-relaxation algorithm compared to LLS lateration

Lateration	**Spring-Relaxation**
Median = 13.8 mm Mean error = 14.5 mm 90-percentile = 25.2 mm Std-deviation = 8.0 mm	Median = 12.4 mm Mean error = 13.1 mm 90-percentile = 21.8 mm Std-deviation = 6.9 mm

5.7 Benchmarking with Visible Light Positioning

To benchmark the performance accuracy of UIL against Visible Light Positioning (VLP) system, the same test bed and algorithm applications are applied to the 2 systems. The VLP system implemented here used the exact platform set up as the above ultrasound indoor localization (UIL) system as described in section 5.4, also see Figure 5.12. Four LED luminaires were placed in the same positions that were previously occupied by the US transmitters. The details of the VLP hardware can be found in Chapter 4. For the experiments conducted, the luminaires were set to unique frequencies of 2.5, 2.7, 3.2 and 3.5 kHz, respectively, allowing for Frequency-Division Multiplexing (FDM) of the transmitted signals.

During the offline stage, the RSS–distance relationship was found by calibrating the Lambertian propagation model. RSS data were collected at a set number of pre-determined locations for the parameter calibration. For this experiment, it involved in taking offline RSS measurements at 17 points to estimate m_i , the Lambertian order for model calibration. Refer to Figure 5.19 for the location of the calibration measurement points. Please refer to Chapter 4, Section 4.4 for detail explanation of offline calibration of VLP.

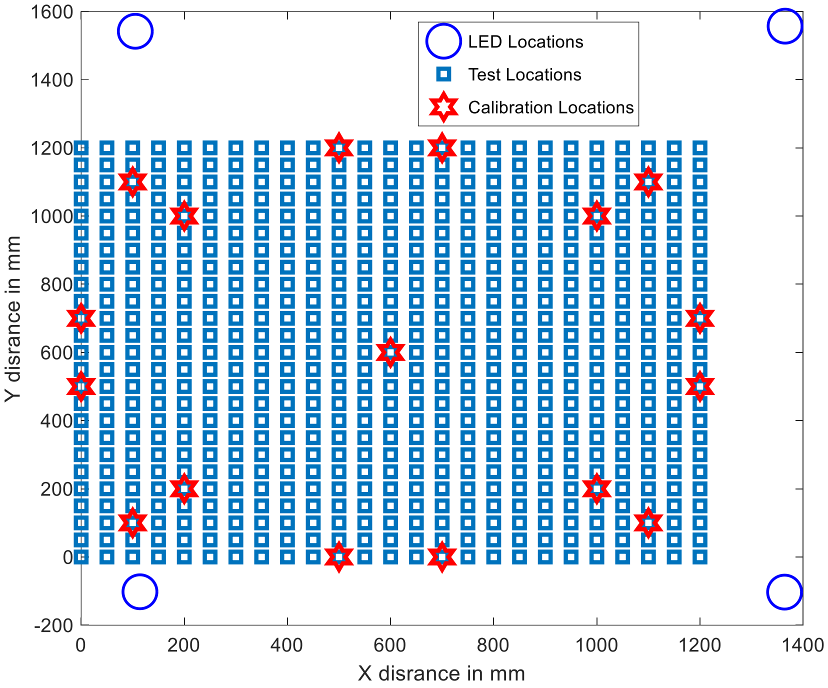

Fig. 5.19 Measurement locations and test setup for the VLP system [100]

Once range distances are found from for all four luminaires, the spring relaxation algorithm outlined in Section 5.5 was used to find the location of the target. Here the target object with the photodiode sensor, is taking the place of microphone receiver unit. The localization accuracy of the VLP is shown in Table 5.4 and in the CDF plot shown in Figure 5.20. As can be seen, the UIL system is far more accurate than the VLP system.

Table 5.4 Localization accuracy of the UIL compared to VLP.

Ultrasound indoor localization (UIL)	**Visible light positioning (VLP)**
Median = 12.4 mm Mean error = 13.0 mm 90-percentile = 21. 8 mm Std-deviation = 6.9 mm	Median = 33.7 mm Mean error = 36.5 mm 90-percentile = 58.6 mm Std-deviation = 17.3 mm

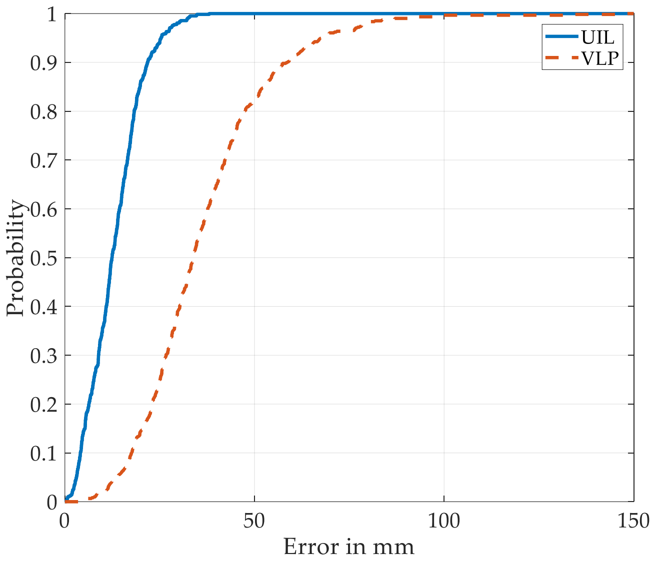

Fig.5.20 Benchmarking the UIL against VLP using a CDF showing UIL is more accurate. Mean, Median, 90th percentile and standard deviation of the error shown in Table 5.4 [100]

5.8 Summary

The SR algorithm was successfully implemented for an UIL system to achieve accurate positioning. For the experimental set up utilized, SR outperforms the well-known LLS-based lateration technique. Furthermore, the UIL system was found to be more accurate than a VLP system. Unlike the VLP system, the UIL system does not require parameter calibration, only needing the ambient temperature, making it easier to deploy in a changing environment. It should be noted that VLP has the advantage of being able to potentially leverage the existing lighting systems if the luminaires are enabled with VLC technology. In such a scenario, the ultrasonic technique can be fused with the VLP system to extend coverage, eliminate blind spot, provide fault tolerance and maintain the robustness of the system in case one of the luminaires becomes faulty.

Chapter 6 – Conclusion

The focus of this PhD was on addressing several gaps in the literature of visible light positioning. The contributions made can be summarised as follows:

- Chapter 3: The localization accuracy of the popular Weighted KNN can be improved by using the Squared Chord Distance (SCD) rather than the commonly used Euclidean distance (ED). This is supported by experiments conducted on a room-scale VLP testbed.
- Chapter 4: Reasonably simple VLP system using cost effective photodiode-based sensor can potentially be used to control a 2D robot. This conclusion is supported by the experimental data collected while driving a CNC machine using solely a VLP employing two proposed novel algorithms.
- Chapter 5: Ultrasonic localization system is very accurate and can be a viable option for supplementing the coverage of a VLP system. This is based on the experiments conducted with a custom-made ultrasonic localization system and a same-platform benchmarking against a VLP system.

6. 1 Future Work:

As outlined in the previous section and in Chapter 1, this PhD work has made several original and novel contributions to the discipline of Visible light positioning. Further research can be carried out to extend the works presented in this thesis and to address the research gaps that were not covered during this PhD research. These include:

- Application of neural network for fingerprint based VLP
  - The work presented in Chapter 2 utilised WKNN algorithm for online positioning. In the ensuing years, neural networks have become popular for fingerprint-based positioning. Therefore, an obvious avenue to explore in the future is to investigate the efficacy of neural network-based positioning. However, more extensive data collection might be necessary to accommodate the needs of neural networks that typically requires large amount of data for training.

- 3D positioning
    - The VLP systems and the algorithms developed for this PhD work are applicable to 2D positioning only. While for many applications, only 2D positioning is required, there are also popular use cases for 3D positioning (e.g., controlling UAV). Therefore, future work should explore 3D positioning using visible light. Such 3D positioning could involve utilising a receiver with multiple photodiodes and the incorporation of inertial measurement unit.

- Mitigation of the impact of tilt
    - The VLP algorithms were developed with the assumption that that the PD and the luminaires are parallel. If the receiver tilts, the localisation estimate gets impacted. For many applications, a simple gimbal can ensure that the receiver maintains its orientation. However, there are also models [68] that addresses this issue and thus can be adopted. Incorporation of accelerometer and inertial measurement unit can be a potential approach to account for the tilt of the receiver.

- Pose estimation
    - Pose comprises of location and orientation. For the work presented in Chapter 4, the location was determined by VLP. The orientation was determined by the CNC. Therefore, developing a new receiver capable of VLP-based orientation estimation will enable more sophisticated control strategies. Bernades et al. [69] proposed a multi-PD based system for estimating the orientation of the receiver for an Infrared (IR)-based positioning system. A similar approach can be applied for estimating the complete pose (both location and orientation) of the receiver. Incorporating orientation information into the algorithm and conducting new benchmarking experiments will open new avenues for investigation. Obstacle avoidance and path planning can also be investigated in the future. But this would require utilising additional sensors alongside the PD. At this point a standard mobile robot can be employed rather than an emulated robot like a CNC.

- Sensor fusion for fault tolerance

- The investigation carried out in Chapter 5 clearly shows that ultrasonic positioning systems are extremely accurate. Therefore, they can potentially be utilised to supplement the light sources and eliminate the coverage “blind spots” of the VLP system. Development of such a fault tolerant system has been left for future works. A sensor fusion approach utilising some form of a Kalman filter can be potential method for achieving robust sensor fusion.

References

[1] T. T. Khanh, V. Nguyen, X.-Q. Pham, and E.-N. Huh, "Wi-Fi indoor positioning and navigation: a cloudlet-based cloud computing approach," *Human-centric Computing and Information Sciences,* vol. 10, no. 1, pp. 1-26, 2020.

[2] M. Sasikala, J. Athena, and A. S. Rini, "Received Signal Strength based Indoor Positioning with RFID," in *2021 IEEE International Conference on RFID Technology and Applications (RFID-TA)*, 2021: IEEE, pp. 260-263.

[3] Y. Cheng and T. Zhou, "UWB indoor positioning algorithm based on TDOA technology," in *2019 10th international conference on information technology in medicine and education (ITME)*, 2019: IEEE, pp. 777-782.

[4] A. Loganathan, N. S. Ahmad, and P. Goh, "Self-adaptive filtering approach for improved indoor localization of a mobile node with zigbee-based RSSI and odometry," *Sensors,* vol. 19, no. 21, p. 4748, 2019.

[5] M. Shen, Y. Wang, Y. Jiang, H. Ji, B. Wang, and Z. Huang, "A new positioning method based on multiple ultrasonic sensors for autonomous mobile robot," *Sensors,* vol. 20, no. 1, p. 17, 2020.

[6] B. Kim and S.-H. Kong, "A novel indoor positioning technique using magnetic fingerprint difference," *IEEE Transactions on Instrumentation and Measurement,* vol. 65, no. 9, pp. 2035-2045, 2016.

[7] B. Gozick, K. P. Subbu, R. Dantu, and T. Maeshiro, "Magnetic maps for indoor navigation," *IEEE Transactions on Instrumentation and Measurement,* vol. 60, no. 12, pp. 3883-3891, 2011.

[8] Y.-T. Wang, C.-C. Peng, A. A. Ravankar, and A. Ravankar, "A single LiDAR-based feature fusion indoor localization algorithm," *Sensors,* vol. 18, no. 4, p. 1294, 2018.

[9] A. Poulose and D. S. Han, "Hybrid indoor localization using IMU sensors and smartphone camera," *Sensors,* vol. 19, no. 23, p. 5084, 2019.

[10] M. Maheepala, A. Z. Kouzani, and M. A. Joordens, "Light-based indoor positioning systems: A review," *IEEE Sensors Journal,* vol. 20, no. 8, pp. 3971-3995, 2020.

[11] L. E. M. Matheus, A. B. Vieira, L. F. Vieira, M. A. Vieira, and O. Gnawali, "Visible light communication: concepts, applications and challenges," *IEEE Communications Surveys & Tutorials,* vol. 21, no. 4, pp. 3204-3237, 2019.

[12] F. Alam, N. Faulkner, M. Legg, and S. Demidenko, "Indoor visible light positioning using spring-relaxation technique in real-world setting," *IEEE Access,* vol. 7, pp. 91347-91359, 2019.

[13] Y. Zhuang *et al.*, "A survey of positioning systems using visible LED lights," *IEEE Communications Surveys & Tutorials,* vol. 20, no. 3, pp. 1963-1988, 2018.

[14] S. Bastiaens, W. Raes, N. Stevens, L. Martens, W. Joseph, and D. Plets, "Impact of a photodiode’s angular characteristics on RSS-based VLP accuracy," *Ieee Access,* vol. 8, pp. 83116-83130, 2020.

[15] R. Amsters, E. Demeester, N. Stevens, and P. Slaets, "In-depth analysis of unmodulated visible light positioning using the iterated extended kalman filter," *Sensors,* vol. 19, no. 23, p. 5198, 2019.

[16] B. Xie *et al.*, "LIPS: A Light Intensity--Based Positioning System for Indoor Environments," *ACM Transactions on Sensor Networks (TOSN),* vol. 12, no. 4, p. 28, 2016.

[17] Y.-S. Kuo, P. Pannuto, K.-J. Hsiao, and P. Dutta, "Luxapose: Indoor positioning with mobile phones and visible light," in *Proceedings of the 20th annual international conference on Mobile computing and networking*, 2014, pp. 447-458.

[18] J. Nah, R. Parthiban, and M. Jaward, "Visible light communications localization using TDOA-based coherent heterodyne detection," in *Photonics (ICP), 2013 IEEE 4th International Conference on*, 2013: IEEE, pp. 247-249.

[19] H. Sharifi, A. Kumar, F. Alam, and K. M. Arif, "Indoor localization of mobile robot with visible light communication," in *Mechatronic and Embedded Systems and Applications (MESA), 2016 12th IEEE/ASME International Conference on*, 2016: IEEE, pp. 1-6.

[20] S. Lee and S.-Y. Jung, "Location awareness using angle-of-arrival based circular-PD-array for visible light communication," in *Communications (APCC), 2012 18th Asia-Pacific Conference on*, 2012: IEEE, pp. 480-485.

[21] T.-H. Do and M. Yoo, "An in-depth survey of visible light communication based positioning systems," *Sensors,* vol. 16, no. 5, p. 678, 2016.

[22] F. Alam, B. Parr, and S. Mander, "Visible light positioning based on calibrated propagation model," *IEEE Sensors Letters,* vol. 3, no. 2, pp. 1-4, 2018.

[23] P. Luo, M. Zhang, X. Zhang, G. Cai, D. Han, and Q. Li, "An indoor visible light communication positioning system using dual-tone multi-frequency technique," in *Optical Wireless Communications (IWOW), 2013 2nd International Workshop on*, 2013: IEEE, pp. 25-29.

[24] U. Nadeem, N. Hassan, M. Pasha, and C. Yuen, "Indoor positioning system designs using visible LED lights: performance comparison of TDM and FDM protocols," *Electronics Letters,* vol. 51, no. 1, pp. 72-74, 2015.

[25] J. Armstrong, Y. A. Sekercioglu, and A. Neild, "Visible light positioning: A roadmap for international standardization," *IEEE Communications Magazine,* vol. 51, no. 12, pp. 68-73, 2013.

[26] X. Guo, S. Shao, N. Ansari, and A. Khreishah, "Indoor localization using visible light via fusion of multiple classifiers," *IEEE photonics journal,* vol. 9, no. 6, pp. 1-16, 2017.

[27] F. Zafari, A. Gkelias, and K. K. Leung, "A survey of indoor localization systems and technologies," *IEEE Communications Surveys & Tutorials,* vol. 21, no. 3, pp. 2568-2599, 2019.

[28] M. Afzalan and F. Jazizadeh, "Indoor positioning based on visible light communication: A performance-based survey of real-world prototypes," *ACM Computing Surveys (CSUR),* vol. 52, no. 2, pp. 1-36, 2019.

[29] M. Kavehrad and W. Zhang, "Light positioning system (LPS)," in *Visible Light Communication*: Cambridge University Press, 2015, pp. 70-87.

[30] M. F. Keskin, A. D. Sezer, and S. Gezici, "Localization via visible light systems," *Proceedings of the IEEE,* vol. 106, no. 6, pp. 1063-1088, 2018.

[31] K. Y. Yi, D. Y. Kim, and K. M. Yi, "Development of a localization system based on VLC technique for an indoor environment," *Journal of Electrical Engineering and Technology,* vol. 10, no. 1, pp. 436-442, 2015.

[32] N. Chaudhary, L. N. Alves, and Z. Ghassemblooy, "Current trends on visible light positioning techniques," in *2019 2nd West Asian Colloquium on Optical Wireless Communications (WACOWC)*, 2019: IEEE, pp. 100-105.

[33] J. M. Kahn and J. R. Barry, "Wireless infrared communications," *Proceedings of the IEEE,* vol. 85, no. 2, pp. 265-298, 1997.

[34] M. V. Bhalerao, M. Sumathi, and S. Sonavane, "Line of sight model for visible light communication using Lambertian radiation pattern of LED," *International Journal of Communication Systems,* vol. 30, no. 11, p. e3250, 2017.

[35] H. Zheng, Z. Xu, C. Yu, and M. Gurusamy, "A 3-D high accuracy positioning system based on visible light communication with novel positioning algorithm," *Optics Communications,* vol. 396, pp. 160-168, 2017.

[36] Y. Wang, "Linear least squares localization in sensor networks," *Eurasip journal on wireless communications and networking,* vol. 2015, no. 1, pp. 1-7, 2015.

[37] ISO/IEC 18305:2016, "Information technology - Real time locating systems - Test and evaluation of localization and tracking systems," 2016, doi: ISO/IEC JTC 1/SC 31,11/01/2016

[38] F. Potortì *et al.*, "Comparing the performance of indoor localization systems through the EvAAL framework," *Sensors,* vol. 17, no. 10, p. 2327, 2017.

[39] C. M. Bishop and N. M. Nasrabadi, *Pattern recognition and machine learning* (no. 4). Springer, 2006.

[40] M. Brunato and R. Battiti, "Statistical learning theory for location fingerprinting in wireless LANs," *Computer Networks,* vol. 47, no. 6, pp. 825-845, 2005.

[41] C. Laoudias, D. G. Eliades, P. Kemppi, C. G. Panayiotou, and M. M. Polycarpou, "Indoor localization using neural networks with location fingerprints," in *Artificial Neural Networks–ICANN 2009: 19th International Conference, Limassol, Cyprus, September 14-17, 2009, Proceedings, Part II 19*, 2009: Springer, pp. 954-963.

[42] D. Sánchez-Rodríguez, I. Alonso-González, J. Sánchez-Medina, C. Ley-Bosch, and L. Díaz-Vilariño, "Performance analysis of classification methods for indoor localization in VLC networks," *ISPRS Annals of the Photogrammetry, Remote Sensing and Spatial Information Sciences,* 2017.

[43] M. T. Van, N. Van Tuan, T. T. Son, H. Le-Minh, and A. Burton, "Weighted k-nearest neighbour model for indoor VLC positioning," *Iet Communications,* vol. 11, no. 6, pp. 864-871, 2017.

[44] Z. Zhou, M. Kavehrad, and P. Deng, "Indoor positioning algorithm using light-emitting diode visible light communications," *Optical engineering,* vol. 51, no. 8, pp. 085009-085009, 2012.

[45] H.-S. Kim, D.-R. Kim, S.-H. Yang, Y.-H. Son, and S.-K. Han, "An indoor visible light communication positioning system using a RF carrier allocation technique," *Journal of lightwave technology,* vol. 31, no. 1, pp. 134-144, 2012.

[46] T. Wenge, M.-T. Chew, F. Alam, and G. S. Gupta, "Implementation of a visible light based indoor localization system," in *2018 IEEE Sensors Applications Symposium (SAS)*, 2018: IEEE, pp. 1-6.

[47] A. Wilkins, J. Veitch, and B. Lehman, "LED lighting flicker and potential health concerns: IEEE standard PAR1789 update," in *2010 IEEE Energy Conversion Congress and Exposition*, 2010: IEEE, pp. 171-178.

[48] S. BATRA, C. S. PANDAV, and S. AHUJA, "Light Emitting Diode Lighting Flicker, its Impact on Health, and the Need to Minimise it," *Journal of Clinical & Diagnostic Research,* vol. 13, no. 5, 2019.

[49] K. Xu, H.-Y. Yu, Y.-J. Zhu, and Y. Sun, "On the ergodic channel capacity for indoor visible light communication systems," *IEEE Access,* vol. 5, pp. 833-841, 2017.

[50] S.-H. Cha, "Comprehensive survey on distance/similarity measures between probability density functions," *City,* vol. 1, no. 2, p. 1, 2007.

[51] V. Prasath *et al.*, "Distance and Similarity Measures Effect on the Performance of K-Nearest Neighbor Classifier--A Review," *arXiv preprint arXiv:1708.04321,* 2017.

[52] F. Alam, M. T. Chew, T. Wenge, and G. S. Gupta, "An accurate visible light positioning system using regenerated fingerprint database based on calibrated propagation model," *IEEE Transactions on Instrumentation and Measurement,* vol. 68, no. 8, pp. 2714-2723, 2018.

[53] T. Glass, F. Alam, M. Legg, and F. Noble, "Autonomous fingerprinting and large experimental data set for visible light positioning," *Sensors,* vol. 21, no. 9, p. 3256, 2021.

[54] A. M. Rahman, T. Li, and Y. Wang, "Recent advances in indoor localization via visible lights: A survey," *Sensors,* vol. 20, no. 5, p. 1382, 2020.

[55] T. Tuan-Kiet, H.-T. HUYNH, D.-P. NGUYEN, L. Dinh-Dung, T. Thi-Hong, and Y. NAKASHIMA, "Demonstration of a visible light receiver using rolling-shutter smartphone camera," in *2018 International Conference on Advanced Technologies for Communications (ATC)*, 2018: IEEE, pp. 214-219.

[56] R. Hamagami, T. Ebihara, N. Wakatsuki, Y. Maeda, and K. Mizutani, "Rolling-shutter sensor-based visible light communication with cross-screen filter: communication and positioning system using a commercial camera," in *2021 IEEE 10th Global Conference on Consumer Electronics (GCCE)*, 2021: IEEE, pp. 386-390.

[57] X. Li, N. B. Hassan, A. Burton, Z. Ghassemlooy, S. Zvanovec, and R. Perez-Jimenez, "A simplified model for the rolling shutter based camera in optical camera communications," in *2019 15th International Conference on Telecommunications (ConTEL)*, 2019: IEEE, pp. 1-5.

[58] M. Rátosi and G. Simon, "Real-time localization and tracking using visible light communication," in *2018 International Conference on Indoor Positioning and Indoor Navigation (IPIN)*, 2018: IEEE, pp. 1-8.

[59] D. Li *et al.*, "Deep learning-based robust visible light positioning for high-speed vehicles," in *Photonics*, 2022, vol. 9, no. 9: MDPI, p. 632.

[60] L. Hua *et al.*, "FusionVLP: the fusion of photodiode and camera for visible light positioning," *IEEE Transactions on Vehicular Technology,* vol. 70, no. 11, pp. 11796-11811, 2021.

[61] Y. Zhuang, Q. Wang, M. Shi, P. Cao, L. Qi, and J. Yang, "Low-power centimeter-level localization for indoor mobile robots based on ensemble Kalman smoother using received signal strength," *IEEE Internet of Things Journal,* vol. 6, no. 4, pp. 6513-6522, 2019.

[62] W. Guan, S. Chen, S. Wen, Z. Tan, H. Song, and W. Hou, "High-accuracy robot indoor localization scheme based on robot operating system using visible light positioning," *IEEE Photonics Journal,* vol. 12, no. 2, pp. 1-16, 2020.

[63] W. Guan *et al.*, "Robot localization and navigation using visible light positioning and SLAM fusion," *Journal of Lightwave Technology,* vol. 39, no. 22, pp. 7040-7051, 2021.

[64] W. Guan, L. Huang, B. Hussain, and C. P. Yue, "Robust robotic localization using visible light positioning and inertial fusion," *IEEE Sensors Journal,* vol. 22, no. 6, pp. 4882-4892, 2021.

[65] Q. Liang, J. Lin, and M. Liu, "Towards robust visible light positioning under LED shortage by visual-inertial fusion," in *2019 International Conference on Indoor Positioning and Indoor Navigation (IPIN)*, 2019: IEEE, pp. 1-8.

[66] W. Xinyu, L. Xiaojuan, G. Yong, S. Jiadong, and W. Rui, "Bidirectional potential guided rrt* for motion planning," *IEEE Access,* vol. 7, pp. 95046-95057, 2019.

[67] M. Metzner *et al.*, "High-precision assembly of electronic devices with lightweight robots through sensor-guided insertion," *Procedia CIRP,* vol. 97, pp. 337-341, 2021.

[68] S. Shen, S. Li, and H. Steendam, "Simultaneous position and orientation estimation for visible light systems with multiple LEDs and multiple PDs," *IEEE Journal on Selected Areas in Communications,* vol. 38, no. 8, pp. 1866-1879, 2020.

[69] E. Bernardes, S. Viollet, and T. Raharijaona, "A three-photo-detector optical sensor accurately localizes a mobile robot indoors by using two infrared light-emitting diodes," *IEEE Access,* vol. 8, pp. 87490-87503, 2020.

[70] G. Shi, Y. Li, W. Cheng, L. Dong, J. Yang, and W. Zhang, "Accuracy analysis of indoor visible light communication localization system based on received signal strength in non-line-of-sight environments by using least squares method," *Optical Engineering,* vol. 58, no. 5, p. 056102, 2019.

[71] S. Gummadi *et al.*, "Advances in modern clinical ultrasound," *Advanced Ultrasound in Diagnosis and Therapy,* vol. 2, no. 2, pp. 51-63, 2018.

[72] D. T. Blackstock, "Fundamentals of physical acoustics," ed: Acoustical Society of America, 2001.

[73] B. Barshan, "Fast processing techniques for accurate ultrasonic range measurements," *Measurement Science and technology,* vol. 11, no. 1, p. 45, 2000.

[74] R. Queirós, R. C. Martins, P. S. Girao, and A. C. Serra, "A new method for high resolution ultrasonic ranging in air," in *Proceedings of the XVIII IMEKO World Congress, Rio de Janeiro, Brazil*, 2006, pp. 17-22.

[75] X. Kou and L. Gu, "Research of long range accurate ranging technology based on ultrasonic sensor measurement," *Journal of Networks,* vol. 9, no. 8, p. 2161, 2014.

[76] A. Ward, A. Jones, and A. Hopper, "A new location technique for the active office," *IEEE Personal communications,* vol. 4, no. 5, pp. 42-47, 1997.

[77] M. Addlesee *et al.*, "Implementing a sentient computing system," *Computer,* vol. 34, no. 8, pp. 50-56, 2001.
[78] N. B. Priyantha, A. K. Miu, H. Balakrishnan, and S. Teller, "The cricket compass for context-aware mobile applications," in *Proceedings of the 7th annual international conference on Mobile computing and networking*, 2001, pp. 1-14.
[79] M. Chen, F. Cheng, and R. Gudavalli, "Precision and accuracy in an indoor localization system," *University of California, Berkeley, USA, Tech. Rep. CS294-1/2,* 2003.
[80] M. Hazas and A. Hopper, "Broadband ultrasonic location systems for improved indoor positioning," *IEEE Transactions on mobile Computing,* vol. 5, no. 5, pp. 536-547, 2006.
[81] J. Zhao and Y. Wang, "Autonomous ultrasonic indoor tracking system," in *2008 IEEE International Symposium on Parallel and Distributed Processing with Applications*, 2008: IEEE, pp. 532-539.
[82] M. M. Saad, C. J. Bleakley, T. Ballal, and S. Dobson, "High-accuracy reference-free ultrasonic location estimation," *IEEE Transactions on Instrumentation and Measurement,* vol. 61, no. 6, pp. 1561-1570, 2012.
[83] P. Lazik and A. Rowe, "Indoor pseudo-ranging of mobile devices using ultrasonic chirps," in *Proceedings of the 10th ACM Conference on Embedded Network Sensor Systems*, 2012, pp. 99-112.
[84] V. Filonenko, C. Cullen, and J. D. Carswell, "Indoor positioning for smartphones using asynchronous ultrasound trilateration," *ISPRS International Journal of Geo-Information,* vol. 2, no. 3, pp. 598-620, 2013.
[85] J. Bordoy, J. Wendeberg, C. Schindelhauer, and L. M. Reindl, "Single transceiver device-free indoor localization using ultrasound body reflections and walls," in *2015 International Conference on Indoor Positioning and Indoor Navigation (IPIN)*, 2015: IEEE, pp. 1-7.
[86] T.-S. Nguyen and T.-H. Huynh, "Experimental study of trilateration algorithms for ultrasound-based positioning system on QNX RTOS," in *2016 IEEE International Conference on Real-time Computing and Robotics (RCAR)*, 2016: IEEE, pp. 210-215.
[87] R. Kapoor, S. Ramasamy, A. Gardi, C. Bieber, L. Silverberg, and R. Sabatini, "A novel 3D multilateration sensor using distributed ultrasonic beacons for indoor navigation," *Sensors,* vol. 16, no. 10, p. 1637, 2016.
[88] L. Márton, C. Nagy, and Z. Biró-Ambrus, "Robust trilateration based indoor localization method for omnidirectional mobile robots," in *2016 European Control Conference (ECC)*, 2016: IEEE, pp. 2547-2552.
[89] T.-S. Nguyen, T.-N. Nguyen, Q.-S. Tran, and T.-H. Huynh, "Improvement of ultrasound-based localization system using sine wave detector and can network," *Journal of Sensor and Actuator Networks,* vol. 6, no. 3, p. 12, 2017.
[90] J. Qi and G.-P. Liu, "A robust high-accuracy ultrasound indoor positioning system based on a wireless sensor network," *Sensors,* vol. 17, no. 11, p. 2554, 2017.
[91] J. A. Paredes Moreno, F. J. Álvarez Franco, T. Aguilera Benítez, and J. M. Villadangos Carrizo, "3D indoor positioning of UAVs with spread spectrum ultrasound and time-of-flight cameras," 2018.
[92] Measurement Computing, "DT9836 Series : Multifunction USB data acquisition devices (DAQ)," 2022. [Online]. Available: https://www.mccdaq.com/Products/Multifunction-DAQ/DT9836.
[93] Q. Lin, Z. An, and L. Yang, "Rebooting ultrasonic positioning systems for ultrasound-incapable smart devices," in *The 25th Annual International Conference on Mobile Computing and Networking*, 2019, pp. 1-16.
[94] H. Lee, T. H. Kim, J. W. Choi, and S. Choi, "Chirp signal-based aerial acoustic communication for smart devices," in *2015 IEEE Conference on Computer Communications (INFOCOM)*, 2015: IEEE, pp. 2407-2415.

[95] A. Comuniello, A. De Angelis, G. De Angelis, and A. Moschitta, "Ultrasound time of flight based positioning using the bluetooth low energy protocol," in *2019 IEEE International Symposium on Measurements & Networking (M&N)*, 2019: IEEE, pp. 1-6.

[96] T. Aguilera, F. J. Álvarez, D. Gualda, J. M. Villadangos, Á. Hernández, and J. Ureña, "Multipath compensation algorithm for TDMA-based ultrasonic local positioning systems," *IEEE Transactions on Instrumentation and Measurement,* vol. 67, no. 5, pp. 984-991, 2018.

[97] K. Mannay, J. Ureña, Á. Hernández, M. Machhout, and T. Aguili, "Characterization of an Ultrasonic Local Positioning System for 3D Measurements," *Sensors,* vol. 20, no. 10, p. 2794, 2020.

[98] B.-C. Seet, Q. Zhang, C. H. Foh, and A. C. Fong, "Hybrid RF mapping and Kalman filtered spring relaxation for sensor network localization," *IEEE Sensors Journal,* vol. 12, no. 5, pp. 1427-1435, 2011.

[99] W.-T. Yu, J.-W. Choi, Y. Kim, W.-H. Lee, and S.-C. Kim, "Self-organizing localization with adaptive weights for wireless sensor networks," *IEEE Sensors Journal,* vol. 18, no. 20, pp. 8484-8492, 2018.

[100] M. T. Chew, F. Alam, M. Legg, and G. Sen Gupta, "Accurate Ultrasound Indoor Localization Using Spring-Relaxation Technique," *Electronics,* vol. 10, no. 11, p. 1290, 2021.